Heidelberg University

Department of Physics and Astronomy

Theoretical Biophysics

Prof. Ulrich Schwarz
Summer term 2024
Last update: April 11, 2025

Contents

Important numbers

Quantity	Meaning	Value
N_A	Avogadro constant	1 mol = 6.022×10^{23}
Da	mass of hydrogen atom	1 g/mol = $1.6 \times 10^{-24} g$
M	molar	mol / l $\approx 1/nm^3$
nM	nanomolar	$\approx 1/\mu m^3$
	water concentration	55 M
	cellular ATP / ADP / P_i conc	mM / 10 μM / mM
c_S	physiological salt concentration	100 mM
pH	pH in human cell	7.34
λ	de Broglie or thermal wavelength	0.1 A
l_{DH}	Debye Hückel screening length	1 nm
k_BT	thermal energy	$4.1 \times 10^{-21} J = 2.5 kJ/mol = 0.6 kcal/mol = 4.1 pN nm = 25 meV = eV/40$
ΔV	voltage difference	$k_BT/e = 25 mV$
$\hbar\omega$	red photon (700 nm)	$70 k_BT$
$\hbar\omega$	blue photon (450 nm)	$110 k_BT$
	ATP-hydrolysis	$20 - 30 k_BT$
	work in motor cycle	8 nm $\times$ 5 pN = 10 k_BT
	metabolism of glucose	30 ATP molecules
	number of human cells	3×10^{13}
	regeneration rate human cells	10^7 Hz
	human metabolic rate	90 W = 2.000 kcal / day
	size of human genome	3.2 Gbp
	length of human genome	$2 \times 3.2G \times 0.34nm = 2m$
	mutation rate per bp humans	10^{-8}
	mutation rate per bp HIV	$3\ 10^{-5}$
D	diffusion constant small protein	$(10\mu m)^2/s$
v	velocity molecular motor	$\mu m/s$
	velocity blood flow capillaries	0.3 mm/s
	velocity blood flow aorta	0.4 m/s
	velocity action potential	10-100 m/s
	thickness plasma membrane	4 nm
	tension plasma membrane	0.3 pN/nm = 0.3 mN/m
	cortical tension	2 nN/μm = 2 mN/m
	bending rigidity plasma membrane	20 k_BT
	d / l_p DNA	2 nm / 50 nm
	d / l_p actin	7 nm / 17 μm
	d / l_p intermediate filaments	10 nm / 200 nm - 1 μm
	d / l_p microtubule	25 nm / 1 mm

Some history (NP = Nobel Prize)

1665	Hooke's book Micrographia shows biological cells
1774	Franklin's oil drop experiment demonstrates the nanometer size of molecules
1827	thermal motion of microscopic particles observed by Brown
1873	Plateau experiments on soap films, minimal surfaces
1876	Koch discovered bacteria, germ theory of disease (NP 1905)
1905	Einstein paper on Brownian motion (NP 1921)
1906	Smoluchowski theory on Brownian motion
1908	Langevin equation
1910	Perrin experiments on colloids and Avogadro constant (NP 1926)
1917	Fokker-Planck equation
1920	Staudinger shows that polymers are chain molecules (NP 1953)
1931	Ruska invented the electron microscope (NP 1968)
1940	Kramers reaction-rate theory
1941	DLVO theory for colloids
1944	Onsager solution of the 2D Ising model (NP 1968)
1952	Hodgkin and Huxley papers on action potentials (NP 1963)
1953	structure of DNA by Watson and Crick (NP 1962)
1954	Huxley sliding filament hypothesis for muscle (could have earned him a second NP)
1958	central dogma of molecular biology by Crick
1959	X-ray structure of hemoglobin by Perutz and Kendrew (NP 1962)
1960	FitzHugh and (later) Nagumo phase plane analysis of Hodgkin Huxley model
1965	Density functional theory by Walter Kohn (NP 1998)
1969	Israelachvili surface force apparatus
1969	Oesterhelt discovers light-sensitive proton pumps in bacteria; this is the starting point of optogenetics
1970	Canham curvature elasticity explains discocyte shape
1972	Warshel and Karplus molecular dynamics of biomolecules (NP 2013)
1973	Helfrich Hamiltonian with spontaneous curvature
1976	Neher and Sakmann Nature paper on patch clamp technique for ion channels (NP 1991)
1976	Roger Tsien discovers the Green Fluorescent Protein (GFP) (NP 2008)
1978	Helfrich interaction between membranes
1978	Doi and Edwards reptation model for polymer melts
1979	book *Scaling Concepts in Polymer Physics* by de Gennes (NP 1991)
1981	Binnig and Rohrer invent scanning probe microscopy (NP 1986)
1981	Evans micropipette aspiration of red blood cells
1982	de Gennes and Taupin persistence length of membranes
1983	Howard Berg book on *Random Walks in Biology*

1985	Peliti and Leibler renormalization of bending rigidity
1986	Safinya and Roux X-ray on membranes
1986	Lipowsky and Leibler unbinding transition of membranes
1986	book *The Theory of Polymer Dynamics* by Doi and Edwards
1990	Seifert and Lipowsky paper on vesicle adhesion
1991	spontaneous curvature phase diagram of vesicles (Seifert et al.)
1994	book *Statistical Thermodynamics of Surfaces, Interfaces, and Membranes* by Safran
1994	area difference elasticity (ADE) model for vesicles (Miao et al.)
1995	Marko and Siggia model for stretching the WLC
1997	NP physics 1997 for laser cooling includes Steven Chu, who also works on biomolecules
1997	RMP review by Jülicher, Armand and Prost on molecular motors
1998	MacKinnon Science paper on the structure of the K^+ channel (NP 2003)
2002	Lim et al. PNAS paper on shape of red blood cells
2005	Karl Deisseroth induce action potentials by light (neuronal optogenetics)
2014	NP chemistry for super-resolution microscopy to Eric Betzig, Stefan Hell and Bill Moerner
2016	NP chemistry for the synthetic molecular motors (still missing is one on biological molecular motors)
2017	Stefan Hell invented MINFLUX
2018	NP physics for optical tweezers to Arthur Ashkin
2021	NP physics for complex systems to Giorgio Parisi

Chapter 1

Physics background

In this script on theoretical biophysics we will make use of concepts and methods from many different fields of physics, which we will introduce when they are needed. However, there are two parts of basic physics which we will need right from the start, and therefore we briefly review them in this chapter. The first one is statistical mechanics, and the second one is electrostatics.

1.1 Statistical mechanics

1.1.1 The microcanonical ensemble

The most basic principle of statistical physics is the fundamental postulate that states that a closed system maximizes its entropy. One way to arrive at this conclusion is by starting from information theory. This approach to statistical mechanics has been pioneered by Claude Shannon (founder of information theory) and Edwin Jaynes (inventor of the maximum entropy principle). We start from the Shannon entropy

$$S = -\sum_i p_i \ln p_i \tag{1.1}$$

where i numbers all states of the system and p_i is the probability of a state with $\sum_i p_i = 1$. By multiplying with k_B, we would get the physical (or Gibbs) entropy S. For the microcanonical ensemble, we would have $p_i = 1/\Omega$ being constant (Ω is the number of states) and thus

$$S = k_B \ln \Omega \tag{1.2}$$

which is the famous formula by Boltzmann, which you also find on his grave at the Wiener Zentralfriedhof. One can show that entropy S is a unique measure for the disorder or information content in the probability distribution $\{p_i\}$. From a more physics point of view, it is a measure for phase space volume that is additive over subsystems. A system that explores all possible states to an equal extent has maximal entropy. The microcanonical ensemble assumes that a physical system at equilibrium has exactly this property. The physical basis of this postulate is not completely clear, but a hand-waving explanation is that all dynamical systems

develop more structure with time, because they sample more of interaction space, and thus higher order correlations develop that lead to apparent disorder on the coarse-grained scale on which we can observe them.

1.1.2 The canonical ensemble

In general, biological systems are not in equilibrium and driven by energy that is supplied by the environment (food, light, etc). However, often state variables change only slowly and therefore the system can be described by the laws of thermodynamics and statistical physics, albeit often only on local and temporary scales. Biological systems operate at relatively high and constant (body or room) temperature and therefore the canonical ensemble is relevant, in which we do not prescribe energy (like in the microcanonical ensemble), but averaged energy.

We now want to maximize entropy under the constraint of constant average energy, $\langle E \rangle = U = \sum_i E_i p_i$. We add normalization and average energy constraints with Lagrange multipliers to the Shannon entropy, giving the function

$$\mathcal{S} = -\sum_i p_i \ln p_i - \beta \sum_i E_i p_i - \alpha \sum_i p_i \tag{1.3}$$

and maximize it

$$\delta\mathcal{S} = -\sum_i (\ln p_i + 1 + \alpha + \beta E_i)\, \delta p_i = 0 \tag{1.4}$$

leading to

$$p_i = e^{-(1+\alpha+\beta E_i)} \tag{1.5}$$

From the normalization we get

$$e^{-(1+\alpha)} = const = \frac{1}{Z} \tag{1.6}$$

with

$$Z = \sum_i e^{-\beta E_i} \tag{1.7}$$

From the average condition $U = (1/Z)\sum_i E_i e^{-\beta E_i}$ we get that β should be a function of U. We can make the connection to temperature T and identify $\beta = 1/(k_B T)$. Now we have the Boltzmann distribution:

$$p_i = \frac{1}{Z} e^{-\beta E_i} \tag{1.8}$$

where Z is the partition sum. For a continuous state space, we would replace the sum over states by an integral over states. We conclude that the canonical distribution is the one that maximizes entropy under the condition that the average energy has a fixed (observed) value.

1.1.3 The grandcanonical ensemble

We now generalize to the case of particle exchange with a reservoir, for example molecules in a bulk fluid that can adsorb or bind to a surface. Other examples might be the molecules in an open beer bottle lying on the floor of a lake or the molecules in the cell that is in exchange with its surrounding medium. We now have a second side constraint, namely for the average number of particles, $\langle N \rangle = \sum_i N_i p_i$, resulting in the function

$$\mathcal{S} = -\sum_i p_i \ln p_i - \beta \sum_i E_i p_i - \alpha \sum_i p_i - \gamma \sum_i N_i p_i \tag{1.9}$$

where we have introduced a third Lagrange parameter γ. Variation of this function gives

$$\delta\mathcal{S} = -\sum_i (\ln p_i + 1 + \alpha + \beta E_i + \gamma N_i)\, \delta p_i = 0 \tag{1.10}$$

With the same arguments as above, we can identify $\gamma = -\beta\mu$ with the chemical potential μ. We then get

$$Z_G = \sum_i e^{-\beta(E_i - \mu N_i)} \tag{1.11}$$

for the grandcanonical partition sum and

$$p_i = \frac{1}{Z_G} e^{-\beta(E_i - \mu N_i)} \tag{1.12}$$

for the grandcanonical distribution.

1.1.4 The harmonic system

We now consider a system with one harmonic degree of freedom at constant temperature (canonical ensemble). This could be for example a particle in a one-dimensional laser trap with a harmonic potential $E = \frac{1}{2}kx^2$, where k is the spring constant (trap stiffness) and x is the one-dimensional state space coordinate (position). The corresponding partition sum is

$$Z = \int_{-\infty}^{\infty} dx\, \exp(-\beta E) = \int_{-\infty}^{\infty} dx\, \exp(-\beta \frac{1}{2} k x^2) = \left(\frac{2\pi k_B T}{k}\right)^{\frac{1}{2}} \tag{1.13}$$

where $\beta = 1/(k_B T)$ and we have evaluated the Gaussian integral $\int dx e^{-ax^2} = (\pi/a)^{1/2}$. The corresponding correlation function is the mean squared displacement (MSD):

$$\begin{aligned} < x^2 > &= \frac{1}{Z} \int dx\, x^2 \exp(-\beta \frac{k}{2} x^2) & (1.14) \\ &= \frac{1}{Z} \frac{-2}{\beta} \partial_k Z = \frac{-2}{\beta} \partial_k \ln Z = \frac{k_B T}{k} & (1.15) \end{aligned}$$

Thus the larger temperature T and the smaller trap stiffness k, the larger the excursions of the particle. In fact this relation is used to calibrate laser traps:

$$k = \frac{k_B T}{< x^2 >} \tag{1.16}$$

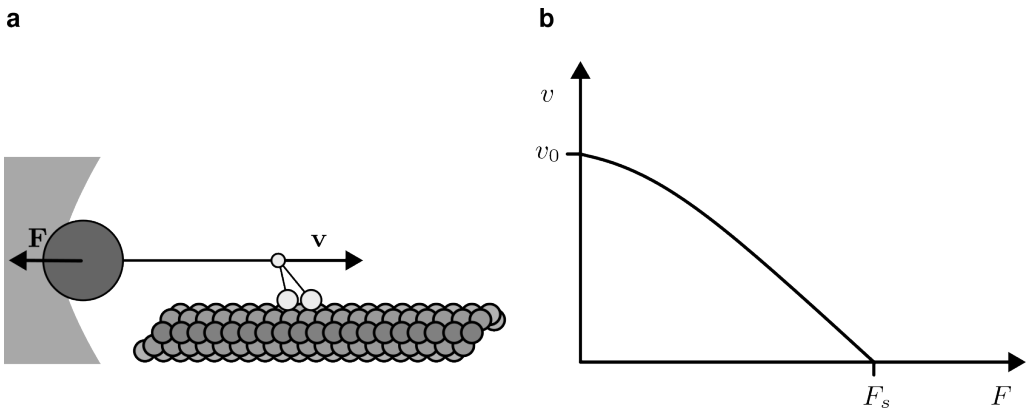

Figure 1.1: Laser traps as harmonic systems. (a) A dielectric bead is attracted to the center of the laser beam. The force F is proportional to the distance from this center. For calibration of trap stiffness k, one uses the relation $< x^2 >= k_B T/k$ for a harmonic system. This is the principle of the optical tweezer as developed in the 1970s by Arthur Ashkin at Bell Labs (Nobel prize physics 2018). The optical tweezer can be used e.g. to measure the force-velocity relation of a molecular motor. Using a feedback system that keeps force F constant, one can measure the corresponding velocity v of the motor. (b) Force-velocity relation for the molecular motor kinesin as measured by Mark J. Schnitzer, Koen Visscher and Steven M. Block, Force production by single kinesin motors, Nature Cell Biology 2, 718 - 723, 2000. The free velocity (without force) is v_0. The larger F, the small v. Eventually the motor gets stalled ($v = 0$) at the stall force F_s.

Because $< x >= 0$, the variance of position is

$$\sigma_x^2 =< (x- < x >)^2 >=< (x^2 - 2x < x > + < x >^2) > \tag{1.17}$$

$$=< x^2 > - < x >^2 =< x^2 >= \frac{k_B T}{k} \tag{1.18}$$

The average energy is

$$< E >= \frac{1}{Z} \int dx\, E \exp(-\beta E) = \frac{-1}{Z} \partial_\beta Z = -\partial_\beta \ln Z = \frac{k_B T}{2} \tag{1.19}$$

This is an example of the equipartition theorem: every harmonic degree of freedom carries an energy of $k_B T/2$. Here we have one degree of freedom, for a harmonic oscillator it would be two (potential and kinetic energy) and for an ideal gas with N particles it would be $3N$ (only kinetic energy, but N particles in three dimensions). The specific heat is constant:

$$c_V = \partial_T < E >= \frac{k_B}{2} \tag{1.20}$$

For the variance of the energy we find

$$\sigma_E^2 =< E^2 > - < E >^2 = \frac{1}{Z} \partial_\beta^2 Z - (\frac{1}{Z} \partial_\beta Z)^2 \tag{1.21}$$

$$= \partial_\beta^2 \ln Z = -\partial_\beta < E >= \frac{(k_B T)^2}{2} \tag{1.22}$$

For the harmonic system, the free energy follows as

$$F = -k_B T \ln Z = \frac{k_B T}{2} \ln(\frac{k}{2\pi k_B T}) = \frac{-k_B T}{2} \ln(2\pi < x^2 >) \tag{1.23}$$

In field theory, this corresponds to the free energy of a Gaussian theory. The harmonic system is the simplest approximation for a bound system and we will encounter it frequently in this script.

1.1.5 The ideal gas

Biomolecules are always in solution and if their concentration is low, the solution is diluted and can be described as an ideal gas. We consider N point particles in a volume V at temperature T (canonical ensemble). The partition sum is

$$Z = \frac{1}{N! h^{3N}} \prod_{i=1}^{N} \int d\vec{p}_i d\vec{q}_i e^{-\beta H(\vec{p},\vec{r})} = \frac{z^N}{N!} \tag{1.24}$$

where $H = \sum_i \vec{p}_i^2/2m$ is the ideal gas Hamiltonian (only kinetic energy), $\vec{p}_i$ and $\vec{q}_i$ are momenta and positions, respectively, of the different particles ($1 \leq i \leq N$). h is Planck's constant. It enters here because the different possible states are assumed to be squeezed together in phase space as closely as permitted by Heisenberg's uncertainty principle, $\Delta p \Delta q \geq h$. The factor $N!$ accounts for the indistinguishability of the particles. z is the partition sum for one particle and again it is simply a Gauss integral:

$$z = \int \frac{d\vec{p} d\vec{q}}{h^3} e^{-\beta \frac{\vec{p}^2}{2m}} = \frac{V}{h^3} (2\pi k_B T m)^{3/2} = \frac{V}{\lambda^3} \tag{1.25}$$

where

$$\lambda = \sqrt{\frac{h^2}{2\pi m k_B T}} \tag{1.26}$$

is the *thermal (de Broglie) wavelength.* A typical value for an atom is 0.1 Angstrom and below this scale, quantum mechanics become relevant. The free energy follows with the help of Stirling's formula $\ln N! \approx N \ln N - N$ for large N as

$$F = -k_B T \ln Z = -k_B T \ln \left(\frac{z^N}{N!} \right) = -k_B T N \left(\ln \left(\frac{V}{\lambda^3 N} \right) + 1 \right) \tag{1.27}$$

The Euler fundamental form for the Helmholtz free energy $F = F(N, V, T)$ is

$$dF = -SdT - pdV + \mu N \tag{1.28}$$

From the statistical mechanics result for the free energy $F = F(N, V, T)$, we can thus now calculate the pressure p as

$$p = -\partial_V F = k_B T \frac{N}{V} \Rightarrow pV = N k_B T \tag{1.29}$$

The result is known as the *thermal equation of state* or simply as the *ideal gas law*.

The average energy is the *caloric equation of state*:

$$< E >= -\partial_\beta \ln Z = -N\partial_\beta \ln \beta^{-3/2} = \frac{3N}{2} k_B T \tag{1.30}$$

which is another example of the equipartition theorem ($3N$ harmonic degrees of freedom).

Finally we calculate the chemical potential as

$$\mu = \partial_N F = k_B T \ln\left(\frac{\lambda^3 N}{V}\right) = k_B T \ln\left(\frac{p}{p_0}\right) \tag{1.31}$$

with $p_0 = k_B T/\lambda^3$ (note that from the three terms, two have canceled each other). Thus chemical potential and pressure are related logarithmically.

We can write our fundamental equation $F(T, V, N)$ and the three equations of state in a very compact way using density $\rho = N/V$:

$$f = \frac{F}{V} = k_B T \rho \left(\ln(\rho\lambda^3) - 1\right) \tag{1.32}$$

$$p = \rho k_B T \tag{1.33}$$

$$e = \frac{< E >}{V} = \frac{3}{2}\rho k_B T \tag{1.34}$$

$$\mu = k_B T \ln\left(\rho\lambda^3\right) \tag{1.35}$$

1.1.6 The law of mass action

From the ideal gas, we get for the chemical potential of species i in dilute solution:

$$\mu_i = \mu_{i0} + k_B T \ln\left(\frac{c_i}{c_{i0}}\right) \tag{1.36}$$

Thus the change in Gibbs free energy at constant T and constant p is

$$\Delta G = \sum_i \frac{\partial G}{\partial N_i} \Delta N_i = \sum_i \mu_i \Delta N_i = \sum_i \mu_i \nu_i \Delta N \tag{1.37}$$

where ν_i are the stoichiometric coefficients of the reaction and ΔN is the reaction coordinate. At equilibrium, $\Delta G = 0$ and ΔN drops out:

$$0 = \sum_i \nu_i \left(\mu_{i0} + k_B T \ln\left(\frac{c_{i,eq}}{c_{i0}}\right)\right) \tag{1.38}$$

From this we get the law of mass action:

$$\Pi_i c_{i,eq}^{\nu_i} = \left(\Pi_i c_{i0}^{\nu_i}\right) e^{-\beta \sum_i \nu_i \mu_{i0}} = const = K_{eq} \tag{1.39}$$

where we have defined the equilibrium constant K_{eq}.

We next consider a reaction with $\Delta N = 1$. The corresponding change in Gibbs free energy is

$$\Delta G = k_B T \ln \left(\frac{\Pi c_i^{\nu_i}}{\Pi c_{i,eq}^{\nu_i}} \right) \tag{1.40}$$

This leads to

$$\Delta G = \Delta G_0 + k_B T \ln \left(\Pi c_i^{\nu_i} \right) \ , \quad \Delta G_0 = -k_B T \ln K_{eq} \tag{1.41}$$

with the understanding that to get a dimensionless argument of the logarithm, we might have to insert some reference concentration (typically 1 M).

A very important example is ATP-hydrolysis, for which we have $\nu_{ATP} = -1$, $\nu_{ADP} = +1$ and $\nu_{P_i} = +1$. Thus we get

$$\Delta G = \Delta G_0 + k_B T \ln \left(\frac{[ADP][P_i]}{[ATP]} \right) \tag{1.42}$$

With a reference concentration of $1M$, the first term is $-12.5 k_B T$. For cellular concentrations ($[ADP] = 10\mu M, [P_i] = mM, [ATP] = mM$), the second term is $-11.5 k_B T$, so together we have $\Delta G = -24 k_B T$.

1.1.7 Phase transitions

If the concentration of a solution increases, the particles start to interact and form a real gas. We briefly discuss the van der Waals gas as the most prominent example of a real gas that is undergoing phase transitions. For particles interacting through some potential U, the partition sum can be divided into an ideal part and an interaction part:

$$Z = Z_{ideal} Z_{inter} \tag{1.43}$$

where

$$Z_{ideal} = \frac{V^N}{N! \lambda^{3N}} \tag{1.44}$$

as above and

$$Z_{inter} = \frac{1}{V^N} \int \left(\prod_{i=1}^{N} d\vec{q}_i \right) e^{-\beta U(\{\vec{q}_i\})} \tag{1.45}$$

This term does not factor into single particle functions because the potential U couples all coordinates. Yet all thermodynamic quantities separate into an ideal gas part and a correction due to the interactions. In particular, we have

$$F = -k_B T \ln Z = F_{ideal} + F_{inter} \tag{1.46}$$

$$p = -\partial_V F = p_{ideal} + p_{inter} \tag{1.47}$$

The formulae for the ideal expressions have been given above. For the pressure, one expects that the correction terms should scale at least in second order in ρ, because two particles have to meet in order to give a contribution to this

term. This suggests to make the following ansatz of a Taylor expansion in ρ, the so-called *virial expansion*:

$$p_{inter} = k_B T \sum_{i=2}^{\infty} B_i(T) \rho^i \tag{1.48}$$

where the $B_i(T)$ are called *virial coefficients*. For many purposes, it is sufficient to consider only the first term in this expansion, that is the second virial coefficient $B_2(T)$. We then have

$$F = N k_B T \left[\ln(\rho \lambda^3) - 1 + B_2 \rho \right] \tag{1.49}$$

$$p = \rho k_B T \left[1 + B_2 \rho \right] \tag{1.50}$$

For pairwise additive potentials, one can show

$$B_2(T) = -\frac{1}{2} \int d\vec{r} \left(e^{-\beta u(\vec{r})} - 1 \right) \tag{1.51}$$

For the van der Waals model, one considers two effects: a hard core repulsion with particle diameter d and a square well attractive potential with an interaction range δ and a depth ϵ. Then one gets, in the limit $\delta/d \ll 1$ and $\beta\epsilon \ll 1$,

$$B_2(T) \approx \frac{2\pi}{3} d^3 - 2\pi (d^2 \delta) \frac{\epsilon}{k_B T} = b - \frac{a}{k_B T} \tag{1.52}$$

where we have introduced two positive constants b (four times the repulsive eigenvolume) and a (representing the attractive part). This general form of $B_2(T)$ has been confirmed experimentally for many real gases. It now allows to rewrite the gas law in the following way:

$$pV = N k_B T (1 + B_2 \frac{N}{V}) \tag{1.53}$$

$$= N k_B T (1 + b \frac{N}{V}) - \frac{N^2 a}{V} \tag{1.54}$$

$$\approx \frac{N k_B T}{1 - b\frac{N}{V}} - \frac{N^2 a}{V} \tag{1.55}$$

thus

$$p = \frac{k_B T}{(v - b)} - \frac{a}{v^2} \tag{1.56}$$

where $v = V/N = 1/\rho$ is the volume per particle. This is the *van der Waals equation of state*: the volume per particle is reduced from v to $v - b$ due to excluded volume, and pressure is reduced by the attractive interaction, that is less momentum is transfered onto the walls due to the cohesive energy.

The van der Waals equation of state (1.56) is characterized by an instability. For a stable system, if a fluctuation occurs to higher density (smaller volume), then a larger pressure should result, which can counteract the fluctuation. Therefore thermodynamic stability requires

$$\frac{\partial p}{\partial V} < 0 \tag{1.57}$$

However, below the critical temperature $T_c = (8a)/(27bk_B)$ the van der Waals isotherms from (1.56) have sections in which this stability criterion is violated. This indicates a fluid-fluid phase transition. The transition region can be calculated by the Maxwell construction from thermodynamics. The van der Waals gas thus predicts the fluid-fluid (gas-liquid) phase coexistence observed at low temperatures.

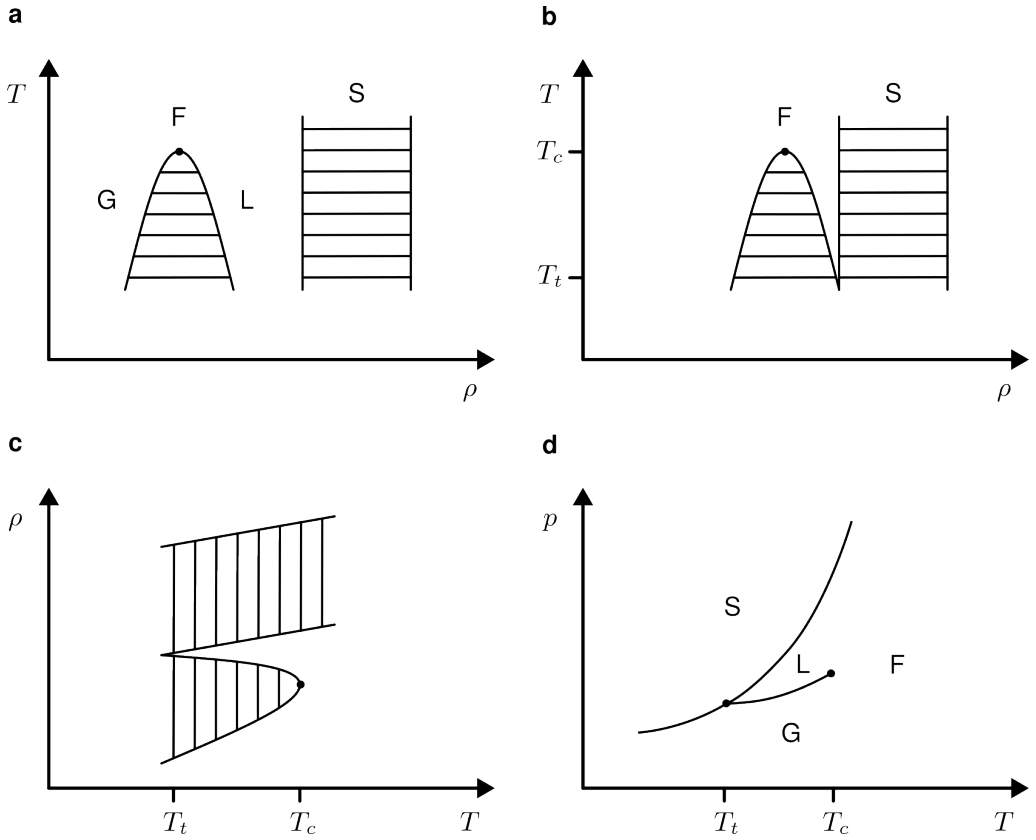

Figure 1.2: (a) A van der Waals fluid has both a fluid-fluid coexistence at low density (due to attraction) and a fluid-solid coexistence at high density (due to eigenvolume). (b) Combining the fluid-fluid and the fluid-solid phase transitions, we get the complete phase diagram of a simple one-component system. (c) We now swap T and ρ axes. (d) By replacing ρ by p, we get the phase diagram in its standard form. Two-phase coexistence regions become lines in this representation. Such a phase diagram is shown e.g. by carbon dioxide (CO_2). The phase diagram by water (H_2O) is similar, but different, because the solid-fluid coexistence line has a different slope.

Interacting systems also show a phase transition to a solid at high densities. Together, one gets the generic phase diagram for a one-component fluid. It fits nicely to the experimental results for simple fluids such as carbon dioxide (CO_2). However, the phase diagram for water is different, as we will see later.

1.2 Electrostatics

1.2.1 Electrostatic potential

In electrostatics, the force on a test particle with charge q_2 is given by Coulomb's law

$$\vec{F} = \frac{q_1 q_2}{4\pi\epsilon_0\epsilon} \cdot \frac{\vec{r}}{r^3} = q_2\vec{E} = -q_2\vec{\nabla}\Phi$$

where ϵ_0 is the electric permitivity of the vacuum and ϵ is the relative permitivity of the medium, and where $\vec{E}$ and Φ are the electrostatic field and the electrostatic potential, respectively, generated by the point charge q_1. Both are additive quantities (superposition principle), therefore for an arbitrary charge distribution with volume charge density $\rho(\vec{r})$ we have:

$$\vec{E} = \frac{1}{4\pi\epsilon_0\epsilon}\int d\vec{r}\prime\, \rho(\vec{r}\prime)\frac{\vec{r}-\vec{r}\prime}{|\vec{r}-\vec{r}\prime|^3} = -\vec{\nabla}\Phi \tag{1.58}$$

$$\Phi(\vec{r}) = \frac{1}{4\pi\epsilon_0\epsilon}\int d\vec{r}\prime\, \frac{\rho(\vec{r}\prime)}{|\vec{r}-\vec{r}\prime|} \tag{1.59}$$

The foundation of electrostatics is formed by the four **Maxwell equations**. These are partial differential equations that usually are derived from experimental observations. Here we are interested only in electrostatic fields. The Maxwell equations then come down to:

$$\vec{\nabla}\times\vec{E} = 0 \tag{1.60}$$

$$\vec{\nabla}\cdot\vec{E} = -\nabla^2\Phi = \boxed{-\Delta\Phi = \frac{\rho(\vec{r})}{\epsilon_0\epsilon}} \qquad \textbf{Poisson equation} \tag{1.61}$$

One can verify this from the explicit representation for $\vec{E}$ given above.

The Poisson equation implies that charges are the sources for the electrostatic potential. For instance, the potential of a point charge with volume charge distribution $\rho(\vec{r}) = Q\cdot\delta(\vec{r})$ can directly be calculated from Eq. 1.61:

$$\nabla^2\Phi \overset{\text{spherical symmetry}}{=} \frac{1}{r}\frac{d^2(r\Phi)}{dr^2} = 0$$
$$\Rightarrow \quad \frac{d(r\Phi)}{dr} = A_1 \quad \Rightarrow \quad \Phi = A_1 + \frac{A_2}{r}$$

As an appropriate boundary condition we choose $\Phi(\infty) = 0$, hence $A_1 = 0$. By comparing our result with the Poisson equation, we finally get

$$\Rightarrow \quad \Phi(r) = \frac{Q}{4\pi\epsilon_0\epsilon}\cdot\frac{1}{r}$$

so we recover the Coulomb law. From a mathematical point of view, the Coulomb law is the Green's function (or propagator) for the Laplace operator in 3D. The given solution can be checked to be true because $\Delta\,(1/r) = -4\pi\delta(r)$.

Sometimes it is useful to rewrite Eq. 1.61 in an integral form, using the divergence theorem known from vector calculus. Denoting the outward-pointing area element of a closed surface as $d\vec{A}$, we find

$$\int_{\partial V} \vec{E}\, d\vec{A} \overset{\text{divergence theorem}}{=} \int_V d\vec{r}\, \vec{\nabla}\cdot\vec{E} \overset{\text{Poisson equation}}{=} \int d\vec{r}\, \frac{\rho(\vec{r})}{\epsilon_0\epsilon}$$

$$\Rightarrow \quad \boxed{\int_{\partial V} \vec{E}\ d\vec{A} = \frac{Q_V}{\epsilon_0\epsilon}} \qquad \textbf{Gauss law} \tag{1.62}$$

where ∂V is a closed surface, V its enclosed volume and Q_V the enclosed charge. As an example, Eq. 1.62 can be used to compute the radial component E_r of the electric field of rotationally symmetric charge distributions (note that the angular components vanish due to spatial symmetry). For a large sphere the Gauss law reads:

$$\int_{\partial V} \vec{E}\, d\vec{A} = 4\pi r^2 E_r = \frac{Q_V}{\epsilon_0\epsilon} \quad \Rightarrow \quad E_r = \frac{Q_V}{4\pi\epsilon_0\epsilon r^2}$$

thus we again recover Coulomb's law.

1.2.2 Multipolar expansion

Consider the work to move a charge q in an electrostatic potential Φ:

$$W = -\int_{\vec{r}_1}^{\vec{r}_2} q\vec{E}d\vec{r} = q\int_{\vec{r}_1}^{\vec{r}_2} \vec{\nabla}\Phi d\vec{r} = q\left[\Phi(\vec{r}_2) - \Phi(\vec{r}_1)\right]$$

The reference position $\vec{r}_1$ can be taken to be at infinity, where the potential vanishes. For a continuous charge distribution, we therefore have

$$E_{pot} = \int d\vec{r}'\rho(\vec{r}')\Phi(\vec{r}')$$

We now consider a charge distribution localized around the position $\vec{r}$ and perform a Taylor expansion around this point:

$$E_{pot} = \int d\vec{r}'\rho(\vec{r}')\left[\Phi(\vec{r}) + (\vec{r}' - \vec{r})\vec{\nabla}\Phi(\vec{r}) + \dots\right] = Q\Phi(\vec{r}) - \vec{p}\cdot\vec{E} + \dots$$

where the monopole Q is the overall charge and the dipole is defined as

$$\vec{p} = \int d\vec{r}'\rho(\vec{r}')(\vec{r}' - \vec{r})$$

We now write the interaction potential between two charge distributions. For a monopole Q_1 at the origin interacting with a monopole Q_2 at $\vec{r}$, we simply get back Coulomb's law:

$$E_{pot} = \frac{Q_1 Q_2}{4\pi\epsilon_0\epsilon}\frac{1}{r}$$

by using the first term and the potential from a monopole. For a dipole $\vec{p}$ at $\vec{r}$ interating with a monopole Q at the origin, we use the second term:

$$E_{pot} = -\vec{p} \cdot \vec{E} = \frac{Q}{4\pi\epsilon_0\epsilon} \frac{\vec{p} \cdot \vec{r}}{r^3}$$

For two dipoles interacting with each other, we first take the potential resulting from a dipole at the origin, which can be read off from the preceding equation:

$$\Phi = \frac{1}{4\pi\epsilon_0\epsilon} \frac{\vec{p_1} \cdot \vec{r}}{r^3}$$

We then get for the interaction

$$E_{pot} = -\vec{p_2} \cdot \vec{E_1} = \frac{1}{4\pi\epsilon_0\epsilon} \left(\frac{\vec{p_1} \cdot \vec{p_2}}{r^3} - \frac{3(\vec{p_1} \cdot \vec{r})(\vec{p_2} \cdot \vec{r})}{r^5} \right)$$

The dipolar interaction is very prominent in biological systems. In particular, water carries a permanent dipole and thus water molecules interact with this potential function.

Chapter 2

Biomolecular interactions and dynamics

From the different types of forces known in physics, only the electrostatic (Coulomb) interaction is directly relevant in biological systems, for two reasons. First it leads to the Schroedinger equation for atoms and molecules, which explains the stability and properties of atoms, ions and biomolecules, which are the microscopic components of biological systems. Second it leads to the interactions and dynamics between these biomolecules; it is this aspect that we discuss in this chapter. Despite the apparent simplicity of only the electrostatic force being relevant, it comes in many different forms and combined with statistical physics leads to the high complexity of biomolecular interactions. The main issue here is that biological systems need to be highly dynamic, so they have to bring the strong Coulomb interaction down to smaller values, for which they use different mechanisms. We start with a discussion of the mechanical properties of biomaterial and immediately see that we are dealing with very weak interactions on the order of thermal energy k_BT, rather than with the eV-scale of electronic phenomena. We then review the details of these interactions and how they can be used in molecular and Brownian dynamics simulations to predict the behaviour of biomolecules, most prominently of proteins.

2.1 The importance of thermal energy

Theoretical biophysics uses mathematical models to study the physics of biological systems. Biophysical length scales cover many orders of magnitude, from atoms (Angstrom) and biomolecules (nanometer) through cells (micrometer) and tissues (centimeter) to multicellular organisms (meter) and populations (kilometers). Biomolecules form supramolecular assemblies like lipid membranes and the polymer networks of the cytoskeleton. Collectively these materials can be classified as *soft matter*, which is a subfield of condensed matter physics. Soft materials are easily deformed by forces which are sometimes only in the range of thermal forces at room temperature, as we shall see in the following.

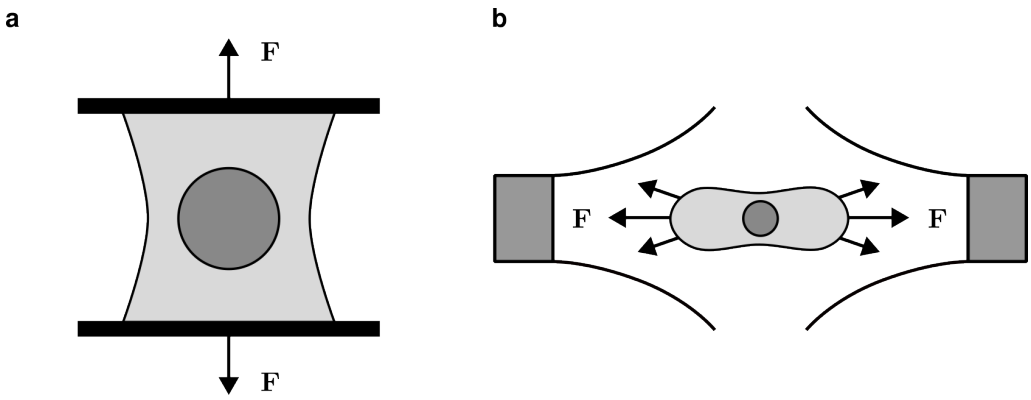

Figure 2.1: Different ways to measure the mechanical rigidity of single cells. (a) Cell stretching between two microplates. A related setup is pulling with an atomic force microscope (AFM), especially when one uses a flat cantilever. (b) Cell stretching with the optical stretcher. A cell is placed between two divergent laser beams. The physical reason for stretching is similar to the one for optical tweezers, namely momentum transfer at interfaces with dielectric contrast.

In order to measure the mechanical stiffness or rigidity of cells, different stretch experiments have been conceived, two of which are illustrated in Fig. 2.1. To first order, the mechanical response to a force is an elastic one. A force F applied over an area A reversibly stretches the material from length L to length $L + \Delta L$ (compare Fig. 2.2a). Force per area and relative deformation are the essential quantities to study, because they do not depend on system size. Also we assume that the first is the cause for the second. We therefore define stress and strain as follows:

$$\text{cause :} \qquad \text{stress} \qquad \sigma = \frac{F}{A} \qquad [\sigma] = \frac{N}{m^2} = Pa$$

$$\text{effect:} \qquad \text{strain} \qquad \epsilon = \frac{\Delta L}{L} \qquad [\epsilon] = 1$$

The simplest possible relation between the two quantities is a linear one:

$$\sigma = E \cdot \epsilon \tag{2.1}$$

where E is the Young's modulus or rigidity of the material with $[E] = Pa$. For cells, this elastic constant is typically in the order of $10\,kPa$. This is also the typical stiffness of connective tissue, including our skin. In general, tissue stiffness is in this range (on the cellular scale, the softest tissue is brain with 100 Pa, and the stiffest tissue is bone with 50 kPa).

Eq. 2.1 might be recognized as Hooke's law, and in fact we can think of the macroscopic deformation as the effect of the stretching of a huge set of microscopic springs which correspond to the elastic elements within the material. Eq. 2.1 can be rewritten as

$$F = \frac{E \cdot A}{L} \cdot \Delta L \tag{2.2}$$

thus $k = E \cdot A/L$ is the effective spring constant of the material. EA is often called the 1D modulus of the material.

Let us now assume that the system is characterized by one typical energy U and one typical length a. A dimensional analysis of E gives $E = U/a^3$. As an example a crosslinked polymer gel as illustrated in Fig. 2.2b can be considered.

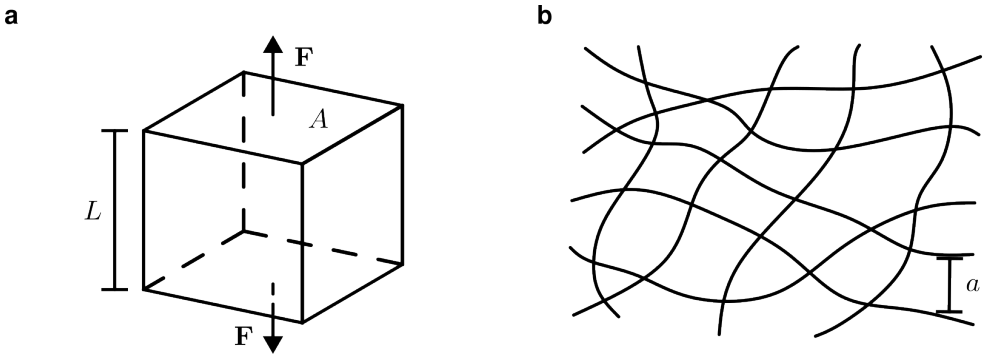

Figure 2.2: (a) A slab of elastic material of length L and cross sectional area A is stretched by a force F. The force acting on the material will result in a deformation. In the case shown here, the box will be stretched by the length ΔL. (b) Illustration of a polymer gel with a meshsize a, defining its typical length scale. In this example, the typical energy U is the elastic energy stored in one cell of the mesh.

The elasticity of cellular material is determined by supramolecular complexes forming the structural elements of the cell with a typical scale $a = 10\,nm$. Therefore we get for the typical energy

$$U = E \cdot a^3 = 10kPa \cdot (10\,nm)^3 = 10^{-20} J \tag{2.3}$$

This is in the order of the thermal energy at ambient or body temperature ($300\,K$) known from statistical mechanics:

$$k_B T = 1.38 \cdot 10^{-23} \frac{J}{K} \cdot 300\,K = 4.1 \cdot 10^{-21}\,J = 4.1\,pN\,nm \tag{2.4}$$

where $k_B = 1.38 \cdot 10^{-23}\,\frac{J}{K}$ is the Boltzmann constant.
In physical chemistry, one usually refers to moles rather than to single molecules:

$$k_B T \cdot N_A = R \cdot T = 2.5\,\frac{kJ}{mol} = 0.6\,\frac{kcal}{mol} \tag{2.5}$$

with $N_A = 6.002 \cdot 10^{23}$ being Avogadro's number and $R = N_A \cdot k_B = 8.31\,\frac{J}{mol \cdot K}$ being the molar gas constant.

Comparing the Young's modulus of biological material to that of an atomic crystal, it becomes clear why we speak of "soft" matter. The energy scale in a crystal usually is in the range of $1\,eV \approx 40\,k_B T$ and it has a typical length a of a few Å. This yields a Young's modulus in the order of 100 GPa. The most rigid material known today is graphene with a Young's modulus of TPa; therefore it has been suggested to be used for building a space elevator.

From the range of the typical energy in supramolecular structures (compare Eq. 2.3) it can be concluded that biological material is held together by many

Chemical Bond	Bond Energy
$C-C$	$140\,k_BT$
$C=C$	$240\,k_BT$
$C\equiv C$	$330\,k_BT$
$H-CHO$	$144\,k_BT$
$H-CN$	$200\,k_BT$

Table 2.1: Some chemical bonds and their corresponding bond energies (at $T \approx 300\,K$)

weak interactions. However, U cannot be smaller than k_BT, because otherwise the entropy of the system would destroy the structure.

Cells are elastic only on the timescale of minutes and later start to flow like viscoelastic material. The constitutive relation of a viscous system is

$$\sigma = \eta \cdot \dot{\epsilon} \tag{2.6}$$

and a typical value for the viscosity of cells is η is $10^5\ Pa\ s$, which is 8 orders of magnitude larger than for water. This high viscosity comes from the polymer networks inside the cell. The corresponding time scale is

$$\tau = \eta/E = 10^5\ Pa\ s/kPa = 100s \tag{2.7}$$

and corresponds to the time the system needs to relax from the external perturbations by internal rearrangements. However, these consideration are only relevant on cellular scales. If we make rheological experiments on the scale of molecules, then we are back to the viscosity and relaxation times of water.

2.2 Review of biomolecular interactions

2.2.1 Covalent ("chemical") bonding

Due to the small length scale of a few Å on which covalent interactions occur, one needs quantum mechanics to explain chemical bonding. Usually, calculations concerning chemical bonding are performed using density functional theory (DFT) which was developed by the physicist Walter Kohn in 1965 (he received the Nobel prize in chemistry in 1998).

The energy of chemical bonds is usually in the range of $\sim 100\,k_BT$ (several $eV = 40\,\mathrm{k_BT}$, comparable to energy scales in solids) and does not only depend on the kind of bonding (single bond, double bond,...), but also on the electronic environment (Tab. 2.1).

2.2.2 Coulomb ("ionic") interaction

Most interactions on biophysical scales are based on the Coulomb interaction, whose central law is Coulomb's law:

$$U = \frac{q_1 q_2}{4\pi\epsilon_0\epsilon r} \qquad \begin{array}{ll} \epsilon_0: & \text{permittivity of vacuum} \\ \epsilon: & \text{dielectric constant} \end{array} \tag{2.8}$$

with the resulting force

$$F = -\frac{dU}{dr} \sim +\frac{q_1 q_2}{r^2} \tag{2.9}$$

which is repulsive if the two electric charges q_1 and q_2 have the same sign and attractive otherwise.

The Coulomb interaction is a "long-ranged" interaction in 3D. To illustrate this, consider the cohesive energy density of a bulk material of diameter L:

$$U_{tot} \propto \int_a^L dr\, r^2 \frac{1}{r^n} \sim r^{3-n}|_a^L = a^{3-n}\left[\left(\frac{L}{a}\right)^{3-n} - 1\right] \tag{2.10}$$

where a is a microscopic cutoff due to the Born repulsion. Taking the limit $L \to \infty$ in Eq. 2.10 shows that U_{tot} does not diverge for $n > 3$, corresponding to a short-ranged interaction where only the local environment significantly contributes to the force on a point-like object. On the other hand, for $n < 3$ the interaction is long-ranged which means that remote objects cannot be neglected. This is especially true for a pure Coulomb interaction (the situation is even worse for gravitation, which not only has $n = 1$ like the Coulomb interaction, but moreover does have only positive charges, so there is not cancellation due to opposite charges). For the special case $n = 3$, we find a logarithmic divergence $U_{tot} \propto \log(L/a)$.

Biological interactions are usually short-ranged for several reasons. One important aspect is that biological systems always operate in water, thus charges such as ions are shielded due to the polarization of the water molecules and, hence, the Coulomb interaction is weakened. This effect is expressed by the large dielectric constant of water ($\epsilon = 80$). Thus the interaction strength is reduced by almost two orders of magnitude in water. Generally, the more polarizable a medium, the larger is its dielectric constant:

$$\epsilon = \begin{cases} 1 & \text{air} \\ 2 & \text{hydrocarbon (oil, fatty acids,...)} \\ 80 & \text{water} \end{cases}$$

Temperature also has an influence on the dielectric constant. With increasing T, the constant decreases due to the thermal motion which disturbs the order in the surrounding medium. This leads to the surprising effect that the interaction can become effectively stronger at higher temperature because polarization goes down.

Due to the difference in dielectric constant of water and hydrocarbons, biological membranes are natural capacitors. This electrical property forms the basis of electrophysiology and the neurosciences.

Biological systems frequently use metal ions such as Ca^{2+}, Mg^{2+} etc. In a solid crystal the ionic interaction is as strong as chemical bonding. For instance, the energy of two neighbouring ions in a sodium (Na^+) chloride (Cl^-) crystal with a lattice constant $a = 2.81$ Å is $U = -200\, k_B T$ (Eq. 2.8 with $q_1 = -q_2 = e$). For

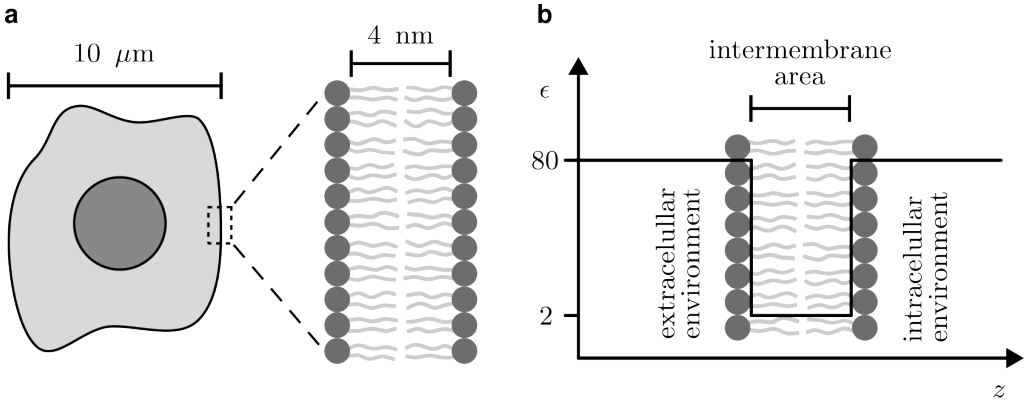

Figure 2.3: (a) Diameter of a typical cell in comparison to the thickness of the biological lipid bilayer membrane. Note the very strong separation of length scales: a very thin oily layer holds together the very large cell. (b) There is a drop of ϵ across the membrane. The situation is similar to two metal sheets separated by plastic. Thus the membrane forms a capacitor.

the total energy density of a crystal, one has to sum over all interactions between nearest, next-nearest,... neighbours within the crystal. Let us first consider only one row (compare Fig. 2.4a).

$$U_{row} = \frac{e^2}{4\pi\epsilon_0 a} \cdot 2 \cdot \left(-1 + \frac{1}{2} - \frac{1}{3} + \dots\right) = -\frac{2e^2}{4\pi\epsilon_0 a} \ln 2 \tag{2.11}$$

Although this summation is mathematically ill-defined (Riemann showed that changing the order of the summation can give any desired value), physically it makes sense. Continuing this calculation to the full three-dimensional crystal, we get

$$U_{tot} = -\underbrace{1.747}_{\substack{\text{Madelung} \\ \text{constant}}} \frac{e^2 N}{4\pi\epsilon_0 a} = -206\,\frac{kcal}{mol} \tag{2.12}$$

From the negative sign of the total energy in Eq. 2.12 it can be concluded that the crystal is stable. The vaporization energy of a NaCl crystal was experimentally determined to be $183\,\frac{kcal}{mol}$. Hence, although Eq. 2.12 is the result of strong assumptions, it nevertheless agrees relatively well with the experimental value.

2.2.3 Dipolar and van der Waals interactions

Many biomolecules do not have a net charge, but rather a charge distribution. In the sense of a multipolar expansion, the most important contribution is the dipolar interaction. For the interaction of two identical dipoles like in Fig. 2.4b, one gets for the interaction energy:

$$U = \frac{(ea)^2}{4\pi\epsilon_0\epsilon_r r^3} \underbrace{\left[\vec{n_1}\cdot\vec{n_2} - 3\left(\vec{n_1}\cdot\hat{\vec{r}}\right)\left(\vec{n_2}\cdot\hat{\vec{r}}\right)\right]}_{f(\Theta,\phi,\dots)} \tag{2.13}$$

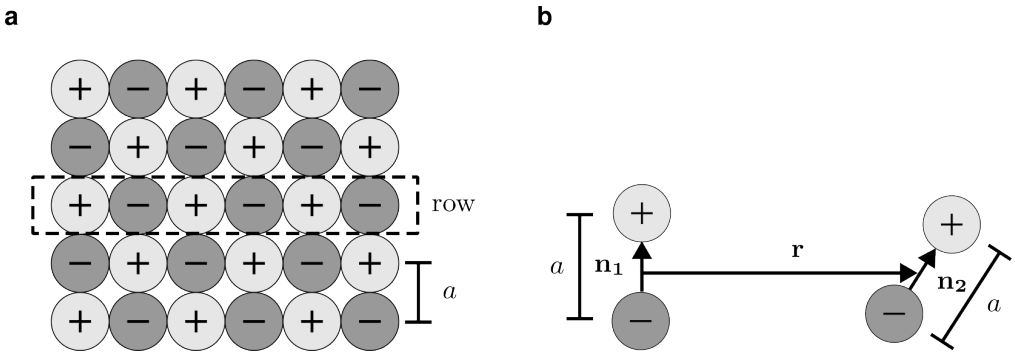

Figure 2.4: (a) Schematic drawing of a simple ionic crystal (such as NaCl). (b) Two dipoles with dipole moments $\vec{p_1} = e \cdot a \cdot \vec{n_1}$ and $\vec{p_2} = e \cdot a \cdot \vec{n_2}$, respectively.

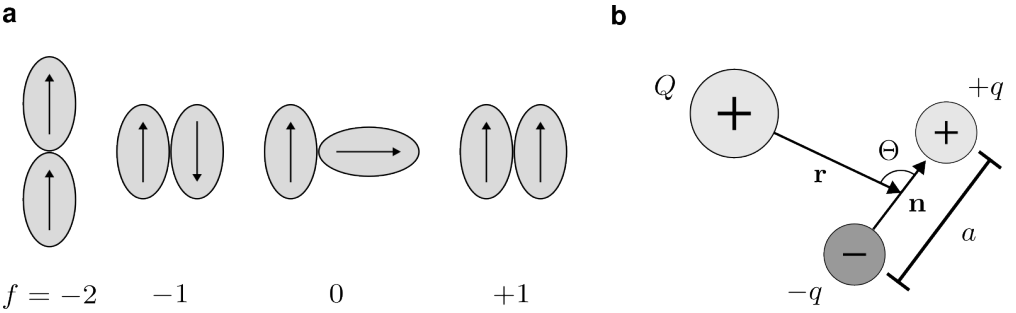

Figure 2.5: (a) f-values of different geometrical arrangements of two dipoles. The more negative the f-value becomes, the more favourable is the arrangement. (b) Interaction between a single charge and a rotating dipole.

The factor $f(\Theta, \phi, \dots)$ does not depend on distance, but on all angles involved. It is thus determined by the geometrical arrangement of the two dipoles and its sign determines whether a certain orientation is favourable or not. Fig. 2.5 shows some dipole arrangements and their corresponding f-values. The most favorable orientation is a head-tail-alignment. In water, but also in dipolar fluids and ferrofluids, this leads to dipole chains, network formation and spontaneous polarization.

The interaction between charge distributions is further weakened by thermal motion. If the dipoles are free to rotate, the interaction becomes weaker. For example, if a charge Q is separated by a distance r from a dipole with dipole moment $\vec{\mu} = q \cdot a$, as depicted in Fig. 2.5, the electrostatic energy of the system is given by

$$U(\vec{r}, \Theta) = \underbrace{\frac{Q\mu}{4\pi\epsilon_0\epsilon r^2}}_{U_0} \cdot \underbrace{\cos(\Theta)}_{\text{orientation factor}} \tag{2.14}$$

The dipole is rotating due to thermal forces, that is why we calculate an effective interaction law by a thermal average weighted with the Boltzmann factor:

$$U(\vec{r}) = \frac{\int_0^\pi \sin(\Theta) \mathrm{d}\Theta U(\vec{r}, \Theta) \exp\left(\frac{-U(\vec{r}, \Theta)}{k_B T}\right)}{\int_0^\pi \sin(\Theta) \mathrm{d}\Theta \exp\left(\frac{-U(\vec{r}, \Theta)}{k_B T}\right)} \tag{2.15}$$

If we assume that the interaction is weak compared to thermal energy, $\frac{-U(\vec{r},\Theta)}{k_BT} \ll 1$, then we can simplify the above expression:

$$\begin{aligned} U(\vec{r}) &= \frac{\int_0^\pi -\mathrm{d}(\cos(\Theta))U_0\cos(\Theta)\left(1-\frac{U_0\cos(\Theta)}{k_BT}\right)}{\int_0^\pi -\mathrm{d}(\cos(\Theta))\left(1-\frac{U_0\cos(\Theta)}{k_BT}\right)} \\ &= -\frac{U_0^2}{3k_BT} = -\frac{1}{3k_BT}\left(\frac{Q\mu}{4\pi\epsilon_0\epsilon}\right)^2\cdot\frac{1}{r^4} \end{aligned} \tag{2.16}$$

So we see the change in the interaction potential from $\frac{1}{r^2}$ for a static dipole to $\frac{1}{r^4}$ for a rotating one. The thermal motion weakens the Coulomb interaction also for dipole-dipole interaction. A similar calculation can be made for dipoles that are free to rotate with a centre-to-centre separation of r. We then obtain

$$U(\vec{r}) = -\frac{2}{3k_BT}\left(\frac{\mu_1\mu_2}{4\pi\epsilon_0\epsilon}\right)^2\cdot\frac{1}{r^6} \tag{2.17}$$

Thus two permanent dipoles interact with an attractive and short-ranged $1/r^6$ - potential.

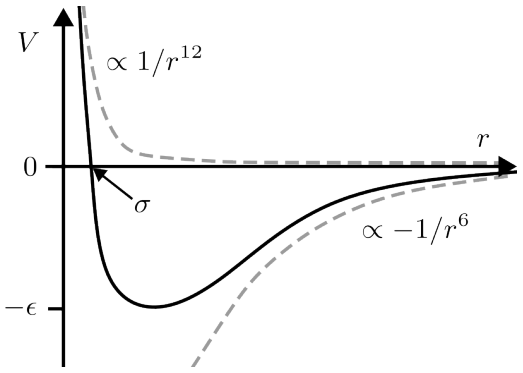

Figure 2.6: Lenard-Jones Potential. We see two different regimes in the interaction between two particles at distance r – the attraction regime $\propto r^{-6}$ and repulsion regime $\propto r^{-12}$.

A universal and short-ranged $1/r^6$-attraction also arises for completely neutral atoms due to quantum fluctuations. A neutral atom can always form a dipole by quantum fluctuations, and this induces another dipole in a near-by atom, with an interaction potential

$$U = -\vec{p}\vec{E} = -\alpha E^2(\vec{r}) \sim -\frac{\alpha}{r^6} \tag{2.18}$$

Here α is the polarizability and $E(\vec{r}) \sim \frac{1}{r^3}$ is the electric field of a dipole. Even spherical and uncharged gas atoms like argon condense into liquids at very low temperatures due to these "dispersion forces" (Fritz London 1937).

The different $\frac{1}{r^6}$-interactions are collectively called "van der Waals forces". As a convenient model for these forces one often uses the "Lenard-Jones potential":

$$U(r) = 4\epsilon\left[(\frac{\sigma}{r})^{12} - (\frac{\sigma}{r})^6\right] \tag{2.19}$$

As one can see in Fig. 2.6, the interaction between atoms is attractive, if they are situated at distances greater than a certain distance σ. If the two particles come closer and closer together, they start to repel each other due to the Born repulsion. This part of the interaction curve is described by the $1/r^{12}$ - potential. The 12th power was not measured, but is rather an arbitrary dependency accepted for convenience. For argon, the parameters are $\epsilon = 0.4\ k_B T$ and $\sigma = 3.4$Å.

2.2.4 Hydrophilic and hydrophobic interactions

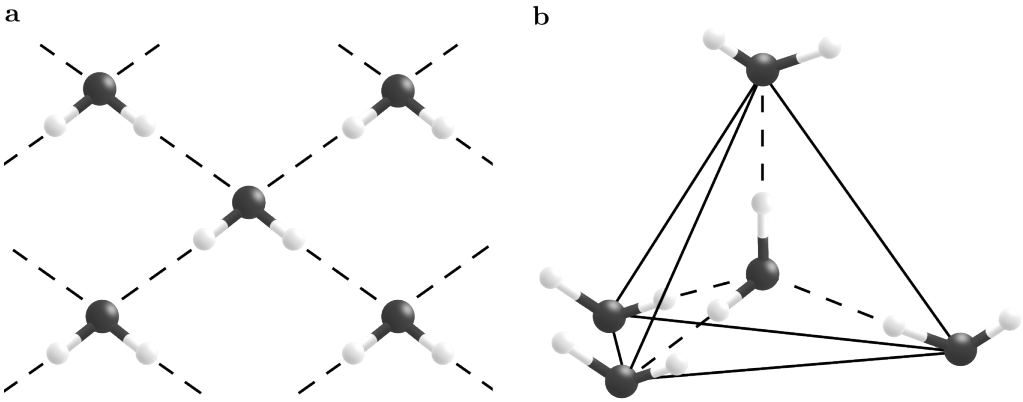

Figure 2.7: (a) A network of water molecules connected by hydrogen bonds. (b) Tetrahedral structure of ice and water, due to the hydrogen bonds between the water molecules.

Much of the complexity of biological systems arises from the peculiar properties of water, in particular from its tendency to form hydrogen bonds. In a hydrogen bond, a hydrogen atom is situated between two other atoms. Water forms hydrogen bonds with itself, as depicted in Fig. 2.7. Because hydrogen bonds can open and close, a lot of entropy is stored in such networks. In three dimensions, the water networks are locally tetrahedral, as depicted in Fig. 2.7. This means that every water molecule has only four neighbors. In comparison, argon atoms have 10 and in close packing structure there are 12.

While the van der Waals interaction tends to condense water molecules, the network of hydrogen bonds creates a more open structure. Because the second effect dominates in ice, it floats on water. This also leads to the maximal density of water at $4\,\mathrm{C}^\circ$. Pressure squeezes the molecules together and usually leads to freezing; in water, it leads to melting. This is part of the explanation why you can skate on ice, but not on glass. The feature of water is demonstrated in Fig. 2.8, where the phase diagrams of water and carbon dioxide are compared. One sees that the main difference is the slope of the coexistence line between solid and liquid. Obviously the case of carbon dioxide is the standard case described by the Lennard-Jones system, while the case of water is special. In general, water should not be considered as a normal liquid, but rather as a network of fluctuating and cooperative hydrogen bonds. Other hydrogen-bonded liquids are hydrogen fluoride HF, hydrogen peroxide H_20_2, hydrogen cyanide HCN.

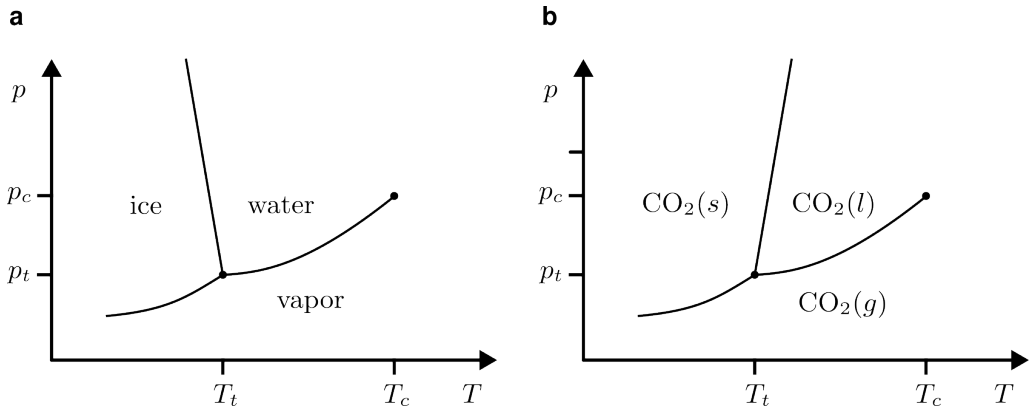

Figure 2.8: (a) Phase diagram of water. (b) Phase diagram of CO_2.

Water is also a very special solvent. It is ordered by the presence of the solutes. For a hydrophobic solute, water molecules point their hydrogen bonds away from the solute. This decreases the entropy and therefore makes solution unfavorable (measured by calorimetry, the effect is the strongest at 25 C°). Because of the "hydrophobic effect" water and oil do not mix. Non-polar solutes attract each other in water and this phenomenon is called the "hydrophobic interaction".

The large energy stored in the network of hydrogen bonds results in large values for the surface tension, melting and boiling temperatures, heat capacity, etc. Because the network of hydrogen bonds is easily polarized, water has a very high dielectric constant ($\epsilon = 80$). It is also important to remember that polar solutes prefer polar solvents due to the low self-energy. In analogy to the previous paragraph this effect is called "hydrophilic interaction".

2.2.5 Protein folding

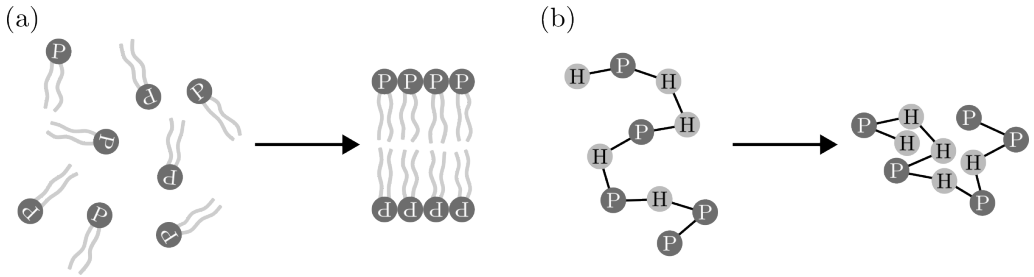

Figure 2.9: The two most important consequences of the hydrophobic effect in biological systems. (a) Lipids form bilayers to shield the hydrophobic tails from the surrounding water. (b) Proteins fold into a native conformation to shield the hydrophobic amino acids from the surrounding water.

The special properties of water are not only the basis of membrane assembly, but also of protein folding, compare Fig. 2.9. A simplest model for analyzing protein folding is the HP-model by Ken Dill. It has been extensively studied on the lattice by exact enumeration. The standard case is a $3 \times 3 \times 3$ lattice, which can

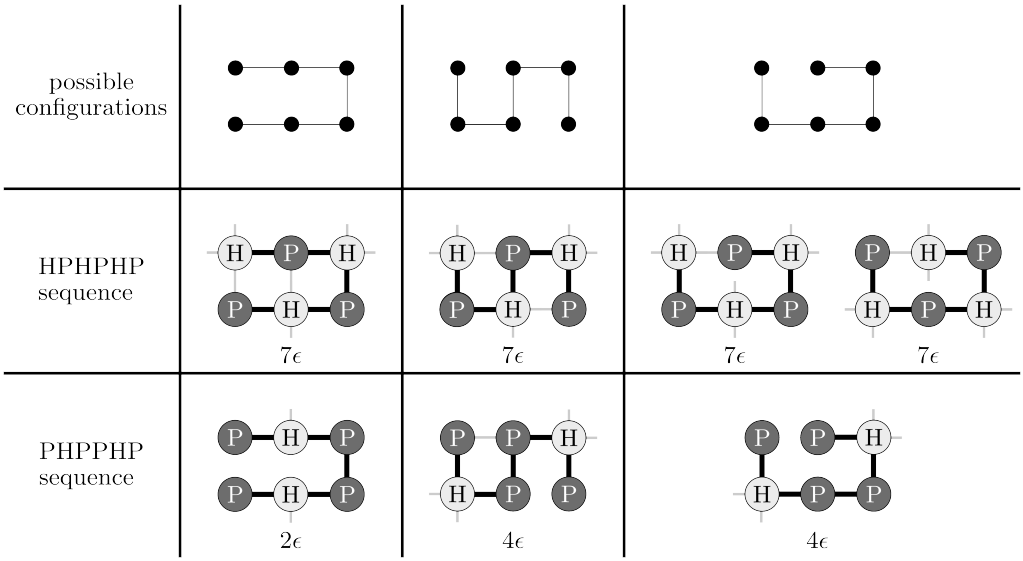

Figure 2.10: HP-model on an 3×2 - lattice. The upper panel shows the possible configurations on this lattice. Center panel: Possibilities to arrange the sequence HPHPHP on the lattice. Note, that for the third configuration there exist two possible arrangements. The energy penalty per H-P contact is ϵ (denoted as green lines). Recall that the environment of the polymer is polar. Lower panel: PHPPHP sequence on the lattice. The first configuration has a unique lowest energy and therefore forms the ground state.

contain $2^{27} = 134217721$ sequences and has 103346 possible configurations (this number is non-trivial because one has to figure out all symmetry operations that make two configurations identical in order to avoid overcounting). We pick one configuration and fill it with a given sequence. After finishing the construct on the lattice, for every amino acid positioned on the outside of the lattice an extra P is added. After that every unfavorable H-P contact is assigned a free energy penalty ϵ. This is repeated for all configurations, and then we look for the one with the lowest energy for a given sequence. If this ground state is unique, we call it "native structure" and the sequence is "protein-like".

The HP-model is a very useful toy model for protein folding. We now consider a simplier variant. This time we have a 2×3 lattice with 2^6 sequences and 3 different configurations. The solvent molecules surrounding the lattice pattern are assumed to be P-monomers. We now try to fit two different sequences on this lattice — HPHPHP and PHPPHP. In Fig. 2.10 all possible configurations for both sequences are shown.

While the first sequence (HPHPHP) is degenerated, the second (PHPPHP) has a unique ground state. The sequence is therefore protein-like. The probability to find the chain in the native structure as function of temperature is given by a sigmoidal function, see Fig. 2.10:

$$\mathrm{P}_{\mathrm{fold}} = \frac{\exp(-2\beta\epsilon)}{\exp(-2\beta\epsilon) + 2\exp(-4\beta\epsilon)} \tag{2.20}$$

where $\beta = 1/k_B T$ as always.

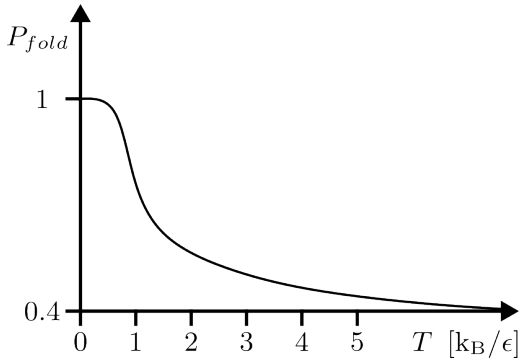

Figure 2.11: The probability to find the native structure as a function of temperature.

While the HP-model is useful to understand the conceptual basis of protein folding, it does not has real predictive power. Predicting the three-dimensional fold of proteins from their sequence is a very large field and many methods have been developed for this purpose. Molecular dynamics is a straight-forward approach, but only works for small proteins. More coarse-grained approaches typically use the contact matrix of all 20 amino acids interacting with themselves. Other important efforts are the folding at home project and the specialized hardware by D.E. Shaw Research.

Every second year, the CASP-competition takes place (Critical Assessment of Structure Prediction) in which the teams compete for the best structure prediction for a few protein structures that has been solved experimentally, but not been published yet. In 2020, at CASP14, the field was revolutionized by a new software called AlphaFold2, introduced by the Google-owned company DeepMind [1]. AlphaFold2 uses machine learning, attention networks, homology modelling and the complete knowledge of solved structures (including their evolutionary history) to predict not only the structures from CASP14, but all known sequences from the human and some other genomes. This effort was quickly followed by a competing machine learning software from the Rosetta-community around David Baker [2]

2.2.6 Steric interactions

Another important class of interactions are excluded volume interactions. Because particles cannot overlap, their entropy is reduced and this creates effective interactions. An example of this kind of effects are polymer brushes, shown in figure 2.12. They repel as the chains start to overlap just for entropy reasons. Therefore they are used to stabilize colloidal suspensions like ink, but also in cell-cell interactions. For example polymer brushes on the outside of a cell membrane help avoiding cell attraction. This effect was understood only about 50 years ago because of its complexity and the need of deep knowledge in statistical physics and understanding of entropy.

Another example of steric interactions can be observed between fluctuating membranes. Imagine two membranes coming closer together, as described in Fig. 2.13.

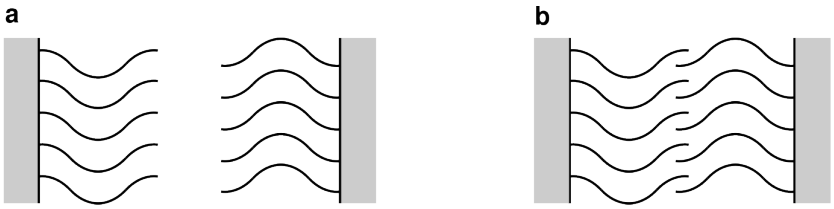

Figure 2.12: (a) Polymer brushes as an example for steric interaction. (b) As the brushes approach each other, the volume available for their motion and hence the entropy is reduced, leading to an effective repulsion.

As d gets smaller the membranes start to perturb each other following the dependency $V(d) \sim \frac{1}{d^2}$. Similar considerations apply for two soft particles (e.g. two cells) approaching each other.

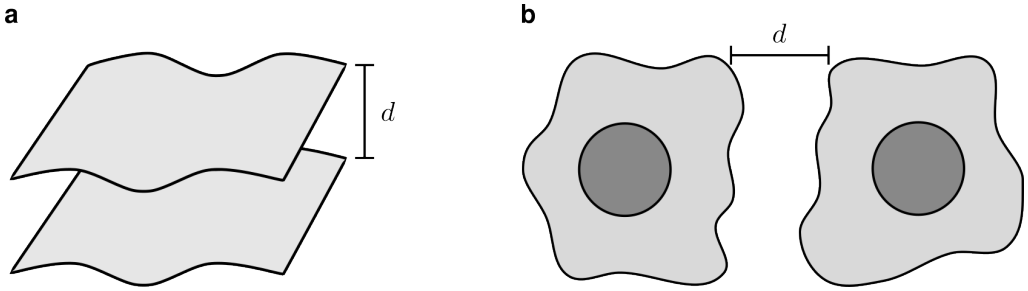

Figure 2.13: (a) The planes represent two membranes that fluctuate to and away from each other. On (b) there are two whole cells with fluctuating membranes.

The last example given here is the depletion interaction. Imagine two large particles (depicted as large spheres in Fig. 2.14) that are surrounded by many small particles. The volume available to the small molecules is marked blue, the excluded volume is marked red. When the two large particles come close together, so that the restricted volumes on their surfaces start to overlap, the entropy of the system increases, because the volume available to the small molecules increases. The system tries to reach a state with higher entropy, that is why the interaction is called entropic attraction.

2.3 Phase separation

For a long time, it was thought that biological systems tend to avoid phase separation, in the sense of the one-component phase diagram shown in Fig. 1.2, which has two types of phase separations at elevated temperature, namely fluid-solid and fluid-fluid. The fluid-solid transition is of course used to make protein crystals for diffraction studies, but for living systems, protein concentrations have to be lower, otherwise they could not move and interact with each other anymore. A transition to a solid is usually related to a pathological condition, like formation of gall or bladder stones. It is actually more relevant for nucleic acids, because viruses, bacteria, fungi, plants and a few other organisms are known to store

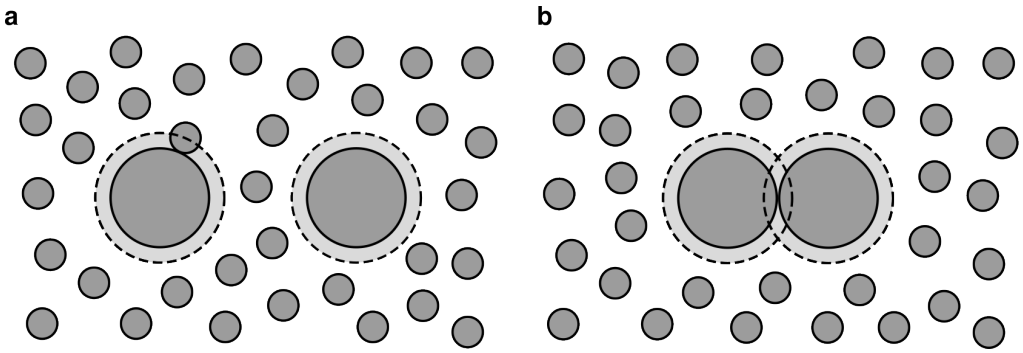

Figure 2.14: Depletion interaction between two big particles in a suspension of smaller particles.

their genetic information in crystal-like structures in order to survive very tough conditions (spores for the cellular systems).

Given the fluid nature of the cytoplasm, a fluid-fluid phase separation would be very natural. Different from the gas-liquid phase separation for the Lennard-Jones system, in a biological system the different densities would only relate to the biomolecules and the density of water would be the same, thus one would speak of a *liquid-liquid phase separation* (LLPS), namely a coexistence of low and high density solutions of proteins.

For a long time, LLPS was thought to not occur in the cytoplasm, but only in the form of lipid rafts, and even there not as a full-fledged phase separation, but rather of enrichment of certain lipids around transmembrane proteins [3, 4], compare Fig. 2.15(a). Although it is hard to prove this concept beyond doubt in cellular systems, it has been nicely confirmed for model systems using vesicles with so-called raft mixtures [4]. These are ternary mixtures of cholesterol (a major component of biological membranes that makes them more flexible) and two lipids, one melting at low and one melting at high temperature. Such systems form a two-phase liquid-liquid coexistence region with a critical point a higher cholesterol concentration (depicted in the Gibbs triangle for ternary mixtures in Fig. 2.15(b)), which might be the basis of lipid rafts in cellular systems.

For a long time, there was no evidence for LLPS in the three-dimensional cytoplasm. Recently, this notion has changed completely, starting with the first direct observation of LLPS in embryos of the worm C. elegans [5, 6]. It was shown that certain proteins and RNA were localized into one side of the embryo by liquid droplets, with round shapes and recovery after photobleaching, thus satisfying the conditions of liquids. Later it was observed that LLPS is tightly connected to the existence of intrinsically disordered proteins (IDPs), that generically tend to undergo LLPS. Examples include the nucleolus, P-granules and stress granules. It is now realized that LLPS are a convenient and very dynamical way to establish compartments in the cell, as an alternative to using membranes or protein shells to create closed compartments, like in vesicles or viruses, respectively. With autophagy and bacterial microcompartments (BMCs), there are even examples which combines both, liquid-liquid phase separation and protein capsid

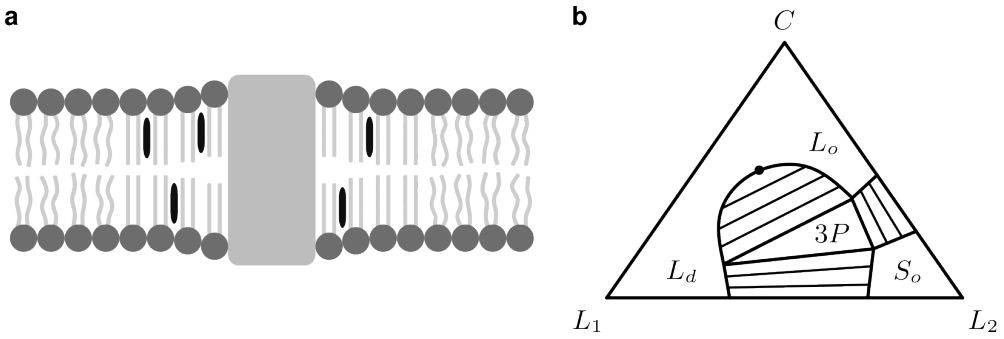

Figure 2.15: (a) Schematic representation of a raft around a transmembrane protein. The protein induces a transition from liquid-disordered to liquid-ordered in the chains of the closeby lipids. In addition, it attracts cholesterol. (b) Ternary phase behaviour of a raft mixtures of a low T_m lipid (L_1), a high T_m lipid (L_2), and cholesterol (C), represented in a Gibbs triangle. The different phases are liquid-ordered L_o, liquid-disordered L_d, and solid S_0. There are one three-phase region and three two-phase regions, one of them with a critical point.

formation.

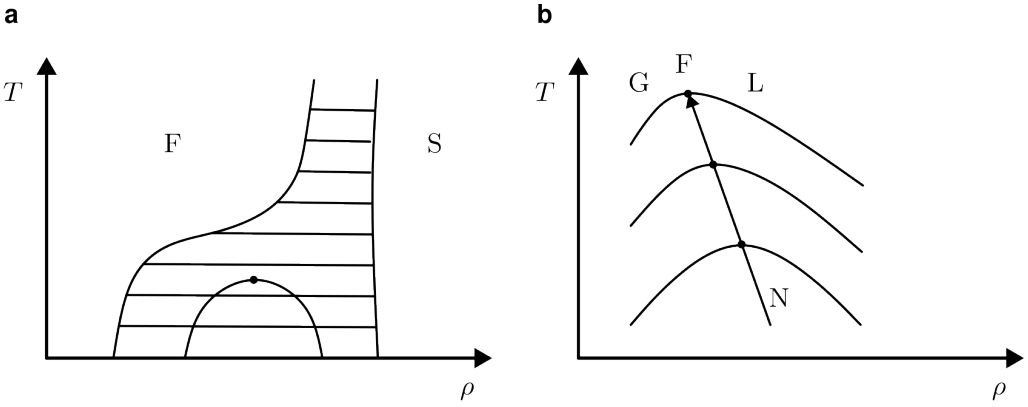

Figure 2.16: (a) Phase diagram for colloids, which are a model system for folded proteins. The fluid-fluid phase transition is overshadowed by the fluid-solid phase transition and thus does not occur. (b) Phase diagram for polymers of increasing chain length N, which are a model system for intrinsically disordered proteins. No solid occurs and the fluid-fluid phase transition dominates.

From the theoretical point of view, one can say that folded and disordered proteins behave as colloids and polymers, respectively [7]. Both phase separate, but large colloids do only crystallize, while polymers only have a liquid-liquid loop, compare Fig. 2.16. Thus in each case, one of the two transitions from Fig. 1.2 is missing. Because IDPs have so much in common with polymers, one can use Flory-Huggins theory to understand their phase behaviour [7].

2.4 Molecular dynamics

Now that we are familiar with the relevant molecular interactions, we have to understand how to combine them in one unifying framework in order to apply them to biomolecules. The structure and dynamics of biomolecules and their interactions can be studied with molecular dynamics (MD) computer simulations. They integrate Newton's equations of motion for atoms interacting through the interaction laws detailed above:

$$m_i \frac{d^2}{dt^2}\vec{r_i} = \vec{F_i} = -\vec{\nabla}_i U(\{\vec{r_j}\}) \tag{2.21}$$

Note that some effects are taken care implicitly (e.g. entropic effects when simulating all particles) and that for some effects one includes effective potentials (e.g. van der Waals interaction). For the energy function we sum all energy contributions as discussed before:

$$\begin{aligned} U \;=\; & \sum_{\substack{\text{covalent}\\ \text{bonds}}} \underbrace{\frac{k_r}{2}(r-r_0)^2}_{\text{bond streching}} + \sum_{\text{angles}} \underbrace{\frac{k_\theta}{2}(\theta-\theta_0)^2}_{\text{bond bending}} + \sum_{\substack{\text{dihedral}\\ \text{angles}}} \underbrace{\frac{k_\phi}{2}(\phi-\phi_0)^2}_{\text{torsion}} \\ & + \sum_{\substack{\text{non-bonded}\\ \text{interactions}\\ <ij>}} \underbrace{\left(\frac{a}{r_{ij}^{12}} - \frac{b}{r_{ij}^{6}}\right)}_{\substack{\text{Lenard-Jones potential}\\ \text{or}\\ \text{van der Waals interactions}}} + \underbrace{\frac{q_i q_j}{4\pi\epsilon_0\epsilon}\cdot\frac{1}{r_{ij})}}_{\substack{\text{Coulomb}\\ \text{interactions}}} \end{aligned} \tag{2.22}$$

Because MD is a Hamiltonian dynamics, energy should be conserved. If we use an Euler scheme for the integration, we usually see deviations from this expectation, compare Fig. 2.17. The problem lies in the algorithm:

$$\vec{r_i}(t+\Delta t) \overset{\text{Taylor expansion}}{=} \vec{r_i}(t) + \vec{v_i}(t)\cdot\Delta t + \frac{\vec{F_i}(t)}{2m_i}\cdot\Delta t^2 + \mathcal{O}((\Delta t)^3) \tag{2.23}$$

$$\vec{v_i}(t+\Delta t) = \vec{v_i}(t) + \frac{\vec{F_i}(t)}{m_i}\cdot\Delta t + \mathcal{O}((\Delta t)^2) \tag{2.24}$$

This procedure is numerically unstable and does not ensure energy conservation and time reversibility even for small time intervals Δt.

The better solution is the "Verlet algorithm", also called "leaping frog":

$$\begin{aligned} \vec{r_i}(t\pm\Delta t) &\overset{\substack{Taylor\\ Expansion}}{=} \vec{r_i}(t) \pm \frac{d}{dt}\vec{r_i}(t)\cdot\Delta t + \frac{1}{2}\frac{d^2}{dt^2}\vec{r_i}(t)\Delta t^2 \pm ... \\ \text{now we} \quad & \text{add both} \quad \text{equations and get} \\ \vec{r_i}(t+\Delta t) &= 2\vec{r_i}(t) - \vec{r_i}(t-\Delta t) + \frac{\vec{F_i}(t)}{m_i}\cdot\Delta t^2 \\ & \quad +\mathcal{O}((\Delta t)^4) \end{aligned} \tag{2.25}$$

One advantage is that the odd terms drop out, but more importantly the velocities are not needed and can be calculated independently by

$$\vec{v_i}(t) = \frac{\vec{r_i}(t+\Delta t) - \vec{r_i}(t-\Delta t)}{2\Delta t}$$

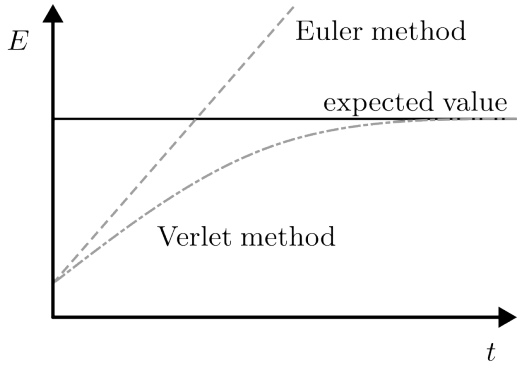

Figure 2.17: Energy distribution over time. From initial condition we need certain relaxation time till we reach expected value with simplectic Verlet method.

Using this algorithm we get results that agree better with our expectations, as can be seen in Fig. 2.17.

When performing MD-simulations, one has to make sure that one is familiar with the technical pitfalls. If one deals with finite system, in order to avoid surface effects, one can work with periodic boundary conditions, truncated Lenard-Jones potentials and the appropriate Ewald sum for the Coulomb interaction [8].

The ensemble described here is a NVE ensemble. However, for biological systems one typically wants constant temperature rather than constant energy (canoncial ensemble). Therefore one has to use a thermostat. Known examples are called after their inventors: Berendsen, Nose-Hoover, Parinello-Bussi (also known as v-rescale thermostat). The main idea is always the same, namely to rescale velocities. For a harmonic degree of freedom, we have the equipartition theorem, $mv^2/2 = k_B T/2$. The simplest way therefore to control temperature is to calculate the current value T from the kinetic energy and then to rescale all velocities with the factor $\lambda = \sqrt{T_0/T}$, where T_0 is the desired temperature. In order to avoid sudden jumps, to allow for fluctuations and to also take potential energies into account, different refinements have been suggested.

Here is a list of the classical papers on MD-simulations:

- Alder, B. J., and TE Wainwright. "Phase transition for a hard sphere system." The Journal of Chemical Physics 27.5 (1957): 1208.
- Rahman, A. "Correlations in the motion of atoms in liquid argon." Physical Review 136.2A (1964): A405.
- Warshel, A., and M. Karplus. "Calculation of ground and excited state potential surfaces of conjugated molecules. I. Formulation and parametrization." Journal of the American Chemical Society 94.16 (1972): 5612-5625.
- Levitt, Michael, and Arieh Warshel. "Computer simulation of protein folding." Nature 253.5494 (1975): 694-698.
- Theoretical studies of enzymic reactions: dielectric, electrostatic and steric

stabilization of the carbonium ion in the reaction of lysozyme. Warshel A, Levitt M. J Mol Biol. 1976 May 15;103(2):227-49.

- Karplus, Martin. "CHARMM: a program for macromolecular energy, minimization, and dynamics calculations." Journal of computational chemistry 4.2,187-217 (1983).

In 2013, the Nobel prize for chemistry was awarded to Karplus, Levitt and Warshel for the development of MD for chemical and biological physics.

Books on MD-simulations:

- Daan Frenkel and Berend Smit, Understanding Molecular Simulation: From Algorithms to Applications. Academic Press 2001
- DC Rapaport, The Art of Molecular Dynamics Simulation, Cambridge University Press 2004
- MP Allan, Computer Simulation Of Liquids, Oxford University Press, U.S.A.; Auflage: Reprint (14. September 2006)

Here are some standard software packages:

- GROMACS: GROningen MAchine for Chemical Simulations (Herman Berendsen, Groningen)
- GROMOS: GROningen MOlecular Simulation computer program package (Wilfred van Gunsteren, Switzerland)
- CHARMM: Chemistry at HARvard Macromolecular Mechanics (Martin Karplus, Harvard)
- NAMD: Not just Another Molecular Dynamics program (Klaus Schulten, Illinois)
- ESPResSo: Extensible Simulation Package for Research on Soft matter (Kurt Kremer and Christian Holm, Mainz and Stuttgart)

Movies on molecular processes (usually based on MD, but in some cases, an artistic component is added):

- Klaus Schulten lab: `http://www.ks.uiuc.edu/Gallery/Movies/`
- DNA learning center: `http://dnalc.org/`
- Biovisions Harvard: `http://biovisions.mcb.harvard.edu`
- D. E. Shaw Research: `https://www.deshawresearch.com` (private company with very fast hardware)
- AlphaFold2: `https://alphafold.ebi.ac.uk` (machine learning software by Deep Mind)
- RoseTTaFold: `https://github.com/RosettaCommons/RoseTTAFold` (machine learning software by David Baker and team)

2.5 Brownian dynamics

Brownian dynamics is an effective or coarse-grained description of how molecules undergo random walks as they constantly collide with other molecules. Like in MD, we start with Newton's equation, for simplicity here for one particle of mass m in one dimension:

$$m\ddot{x} = m\dot{v} = F = -\nabla U \ . \tag{2.26}$$

We now add two new terms: a friction term describing energy dissipation into the surrounding medium and a random force (known as the noise term) that continuously kicks the particle:

$$m\dot{v} = F - \xi v + \sigma\eta(t)$$

Note that it is mandatory to add both terms together, because the noise term alone would input too much energy into the system, so the damping is required to balance this effect. This equation is the famous *Langevin equation*. It is a stochastic differential equation (SDE) and conceptually different from an ordinary (ODE) or a partial differential equation (PDE). σ is the amplitude of the noise term and η describes Gaussian white noise which obeys:

1. $\langle\eta(t)\rangle = 0$
2. $\langle\eta(t)\eta(t')\rangle = 2\delta\left(t - t'\right)$

The formal solution for $F = 0$ is given by:

$$v(t) = e^{-t/t_0}\left(v_0 + \int_0^t ds\ e^{s/t_0}\frac{\sigma}{m}\eta(s)\right)$$

as one can check easily by insertion into the Langevin equation. Here $t_0 = m/\xi$ is the characteristic relaxation time of the system.

Obviously v is defined only through its averages, like the noise itself:

$$\begin{aligned}
\langle v(t)\rangle &= v_0 e^{-t/t_0} \\
\langle v(t)v(t')\rangle &= v_0^2 e^{-\frac{t+t'}{t_0}} + \left(\frac{\sigma}{m}\right)^2 e^{-\frac{t+t'}{t_0}} \underbrace{\int_0^t ds \int_0^{t'} ds'\ e^{\frac{s+s'}{t_0}} 2\delta\left(s - s'\right)}_{\overset{t\leq t'}{=}\int_0^t ds\ 2e^{2s/t_0} = t_0\left(e^{2t/t_0}-1\right)} \\
&= \underbrace{e^{-\frac{t+t'}{t_0}}\left(v_o^2 - \frac{\sigma^2}{m\xi}\right)}_{=0 \text{ for } t,t' \gg t_0} + \frac{\sigma^2}{m\xi}e^{-(t'-t)/t_0}
\end{aligned}$$

$$\Rightarrow \quad \left\langle v(t)^2\right\rangle = \frac{\sigma^2}{m\xi}$$

Note that the linear terms in η have dropped out and that the autocorrelation decays exponentially, thus the system is well-behaved.

The equipartition theorem gives us:

$$\frac{1}{2}m\left\langle v^2\right\rangle = \frac{1}{2}k_BT$$

$$\Rightarrow \quad \boxed{\sigma^2 = \xi k_BT} \quad \text{fluctuation-dissipation theorem}$$

The noise amplitude σ (fluctuations) is related to the friction coefficient ξ (dissipation) through temperature T. The higher temperture T, the stronger the noise.

For $t \gg t_0$, we can neglect inertia:

$$\begin{aligned}
\Rightarrow \quad & \xi v = \sigma\eta(t) = \xi\dot{x} \\
\Rightarrow \quad & x(t) = x_0 + \frac{1}{\xi}\int_0^t dt'\sigma\eta(t') \\
\Rightarrow \quad & \langle x(t)\rangle = x_0 \\
\left\langle (x(t)-x_0)^2\right\rangle &= \frac{1}{\xi^2}\int_0^t dt'\int_0^t dt''\ 2\sigma^2\delta\left(t'-t''\right) \\
&= \frac{1}{\xi^2}2\sigma^2 t \stackrel{!}{=} 2Dt
\end{aligned}$$

Here we identified the diffusion constant D from the one dimensional random walk.

$$\Rightarrow \quad \boxed{D = \frac{\sigma^2}{\xi^2} = \frac{k_BT}{\xi}} \quad \text{Einstein relation}$$

If we use for the friction coefficient Stokes' law from hydrodynamics, $\xi = 6\pi\eta R$ with viscosity η we get:

$$\Rightarrow \quad \boxed{D = \frac{k_BT}{6\pi\eta R}} \quad \text{Stokes-Einstein relation}$$

Inserting in typical numbers ($T = 300$ K, $\eta = 10^{-3}$ Pa s, $R = 1$ nm), we get $D = (10\ \mu m)^2/s$ as typical diffusion constant for proteins. A recent survey of diffusion constants in E. Coli measured by FCS has shown that this is the correct order of magnitude and that the inverse scaling with protein mass is indeed obeyed [9].

We are now in the position to formulate the basic algorithm for BD-simulations:

$$\frac{dx(t)}{dt} = -M\nabla U + \left(\frac{k_BT}{\xi}\right)^{1/2}\eta \tag{2.27}$$

$$= -D\nabla\left(\frac{U}{k_BT}\right) + D^{1/2}\eta \tag{2.28}$$

Here we have introduced the mobility $M = 1/\xi$. Due to the FDT, we only have one relevant parameter, which we take to be D. The discretized version now reads:

$$x(t+\Delta t) = x(t) - D\frac{d}{dx}\left(\frac{U}{k_BT}\right)\Delta t + \sqrt{2D\Delta t}\mathcal{N}(0,1) \tag{2.29}$$

where $\mathcal{N}(0,1)$ is the Gaussian distribution with vanishing mean and unit variance. In order to be able to work with the standard Gaussian, we now explicitly use the factor of 2 that above we have placed in the definition of the Gaussian white noise. It is straight-forward to generalize this scheme to N particles with interaction terms in U.

Different from the MD-community, the BD-community did not converge yet to a few software packages and thus there are many of them. Here are a few examples:

- LAMMPS from Sandia National Labs, started as large-scale parallel MD code, but also includes Langevin, `https://www.lammps.org`
- HOOMD from Sharon Glotzer's lab, also a MD-code with Langevin mode, `https://hoomd-blue.readthedocs.io`
- ESPResSo from Kurt Kremer Mainz / Christian Holms Stuttgart, coarse-grained MD/BD for soft matter, `https://espressomd.org/wordpress`
- Smoldyn from Steve Andrews, point particles and arbitrary geometries, many published projects, `https://www.smoldyn.org`
- MesoRD from Johan Elf, discretized on cubic lattice, diffusion as reaction, Gillespie algorithm, `https://mesord.sourceforge.net`
- Greens Function Reaction Dynamics (GFRD) from Pieter Rein ten Wolde, event-based reactions based on exact solutions to the diffusion equation, `https://gfrd.org`
- Simulation of diffusional association (SDA) from Rebecca Wade, `https://mcm.h-its.org/sda`
- ReaDDy from Frank Noe, includes potentials, combination of MD and BD, `https://readdy.github.io`
- Cytosim from Francois Nedelec, focus on filament mechanics, `https://gitlab.com/f-nedelec/cytosim`

We finally note that in BD one deals with an effective solvent that in principle should also mediate hydrodynamic interactions. The importance of hydrodynamics for self-diffusion and molecular interactions is somehow debated and there are many approaches to address this important issue. Because biomolecules and cells are so small, they have a small Reynolds number:

$$Re = \frac{\rho v L}{\eta} \ll 1 \tag{2.30}$$

if we insert typical values for density ρ and viscosity η of water as well as for velocity v and size L. Thus viscous forces dominate over inertial ones and one has to solve the Stokes equation rather than the Navier-Stokes equation. The most common approaches to hydrodynamics in biological systems are

- analytical solutions, including the Oseen and Rotne-Prager tensors

- FEM-implementations of the Stokes equation, e.g. in FEniCS (`https://fenicsproject.org`)
- Lattice Boltzmann Method (LBM)
- Dissipative Particle Dynamics (DPD)
- Multi Particle Collision Dynamics (MPCD)

For more information, compare the review by Ulf Schiller and colleagues [10].

Chapter 3

Electrostatistics

We already discussed that polarizability and thermal rotation weakens the electrostatic interaction between two molecules in the cell. We now consider this issue further for a charged object (an ion, a biomolecule or an assembly of biomolecules) immersed in a sea of other charges. These surrounding charges are counter-ions (balancing the charge on the object) that can be complemented by co-ions (salt). The fact that the counter- and co-ions are highly mobile and under permanent thermal motion creates a cloud of charge distribution that screens and further decreases the electrostatic interaction between the large objects. This is especially important for genome compactification, for example in viruses or sperm cells.

3.1 Role of geometry

In Fig. 3.1 we depict two important situations of this kind in the cell, namely the charge distributions around a DNA and around a lipid membrane. For the DNA, the size of a basepair is 0.34 nm and we have $6 \cdot 10^9\, bp$ in our genome (counting all chromosome, which come in pairs), thus the DNA in each of our cells amount to a length of 2 m. Now consider that each basepair carries a charge of $2e$ and that the diameter of nuclei are in the order of μm. We therefore must ask the question how the highly charged DNA can be compactified to this small size. The same question arises for bacteria (they typically have one circular chromosome with around 1 Mbp, amounting to a contour length of around 1 mm, packed into a μm large cell body) and for DNA viruses, where the packing density is even higher. As we will see below, the solution to this DNA riddle is provided by theoretical physics in the form of strong coupling theory [11, 12].

For the lipid bilayer depicted in Fig. 3.1, the charge distribution is not characterized by a line charge density λ, but by an area charge density σ. Here the relevant biophysical questions are very different from the case of DNA. Because of the barrier function of the lipid bilayer, we have to ask how charges arrange themselves in its vicinity and how they can cross the bilayer. Obviously the distribution around charged lines and surfaces must be very different for geometrical reasons.

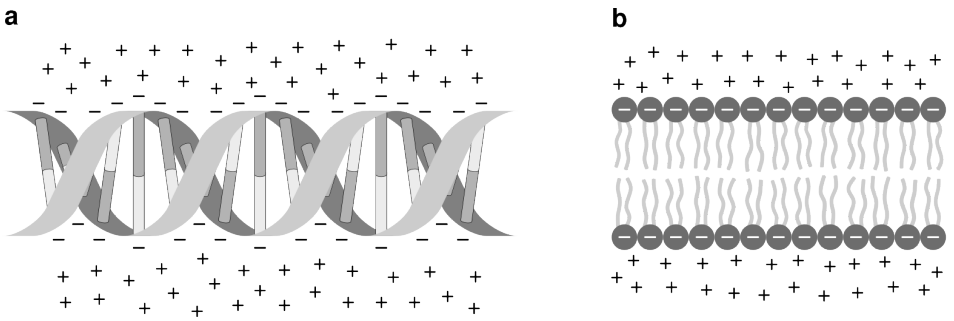

Figure 3.1: (a) DNA is a charged polymer (polyelectrolyte). Per base pair (*bp*, distance between bp $a = 3.4\,\text{Å}$), the DNA carries a charge of $2\,e$ and hence a line charge density of $\lambda = \frac{2e}{3.4\,\text{Å}}$. (b) Lipid membranes are charged plates. Negatively charged head groups of the fatty acids in the plasma membrane result in an area charge density of $\sigma = en_{2d} = \frac{e}{nm^2}$.

As already mentioned in the beginning of this chapter, a DNA molecule can be seen as a charged line with a linear charge density of $\lambda = \frac{2e}{3.4\text{Å}}$. To simplify matters, we assume the DNA molecule to be an infinitely long straight line. Then the DNA exhibits a cylindrical symmetry (compare Fig. 3.2a) and Gauss law can easily be applied to determine the radial component of the electrostatic field:

$$\text{Gauss' law:} \qquad E_r \cdot 2\pi r L = \frac{\lambda L}{\epsilon_0 \epsilon}$$

$$\text{Electrostatic field:} \qquad E_r = \frac{\lambda}{2\pi\epsilon_0\epsilon r} \tag{3.1}$$

$$\text{Potential:} \qquad \Phi \;=\; -\int_a^r E_r(r')\,dr' = -\frac{\lambda}{2\pi\epsilon_0\epsilon}\ln\left(\frac{r}{a}\right) \tag{3.2}$$

where a microscopic limit a was employed. The logarithmic electrostatic potential Φ in Eq. 3.2 diverges for $r \to \infty$. Thus, the usual boundary condition $\Phi(\infty) = 0$ cannot be used. One often encounters this logarithmic behavior in 2D systems. For example, this means that one cannot calculate a simple formula for the flow of a fluid around a cylinder (as one can for the flow of a fluid around a sphere in 3D).

For the straight line charge the same result as in equations 3.2 and 3.2 can be obtained from the direct integration of Coulomb's law (Eq. 1.59) or from the Poisson equation (Eq. 1.61) in cylindrical coordinates.

In the cell, the plasma membrane can be seen as a charged plane with an area charge density $\sigma = \frac{e}{nm^2}$. Again, the electrostatic field can be computed with Gauss law. Restricting oneself to an infinitely large surface with negligible curva-

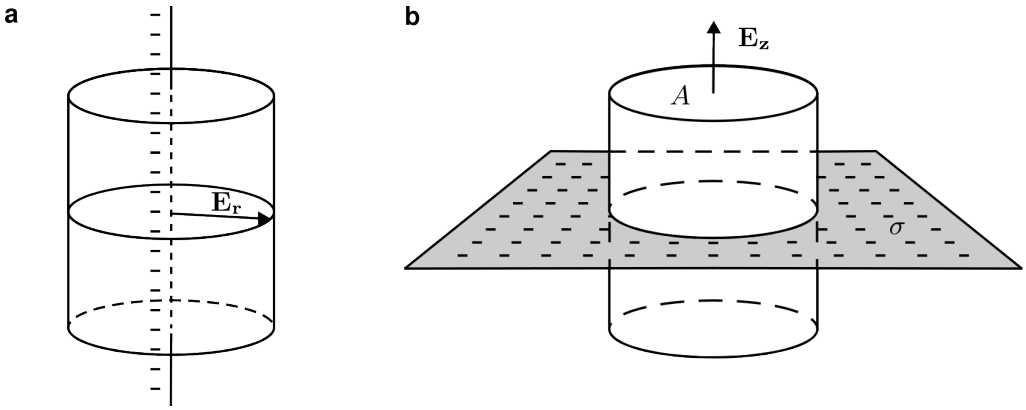

Figure 3.2: Cylindrical symmetry of (a) an infinitely long charged line and (b) charged plane with infinite surface.

ture, the cylindrical symmetry of the plane can be made use of (compare Fig. 3.2):

$$\text{Gauss' law:} \qquad |E_z| \cdot 2A = \frac{A\sigma}{\epsilon_0 \epsilon}$$

$$\text{Electrostatic field :} \qquad E_z = \frac{\sigma}{2\epsilon_0 \epsilon} \frac{z}{|z|} \tag{3.3}$$

$$\text{Potential:} \qquad \Phi = -\int_0^r E_z(z')\, dz' = -\frac{\sigma |z|}{2\epsilon_0 \epsilon} \tag{3.4}$$

Two comments can be made concerning the results in equations 3.3 and 3.4. Firstly, Φ increases linearly with the distance from the charged plane. Secondly, the electric field jumps by $\sigma/(\epsilon_0 \epsilon)$ across the charged plane and does not depend on the distance. As before, the same results can be obtained from explicit integration or from solving the Poisson equation.

3.2 The membrane as a parallel plate capacitor

Besides its function as a diffusion barrier, the biomembrane can act as a parallel plate capacitor (compare Fig. 3.3) if charges are separated to its both sides by active processes such as ion pumps and transporters. Then we are actually dealing with two oppositvely charged planes with electric fields according to Eq. 3.3:

$$E_+ = E_- = \frac{\sigma}{2\epsilon_0 \epsilon} \tag{3.5}$$

Outside the plasma membrane, E_+ and E_- cancel each other, whereas within the membrane they add up:

$$\text{Electrostatic field:} \qquad E_{inside} = E_+ + E_- = \frac{\sigma}{\epsilon_0 \epsilon} \tag{3.6}$$

$$\text{Electrostatic potential difference:} \qquad \Delta\Phi = -\int_0^d dz\, \frac{\sigma}{\epsilon_0 \epsilon} = -\frac{\sigma d}{\epsilon_0 \epsilon} \tag{3.7}$$

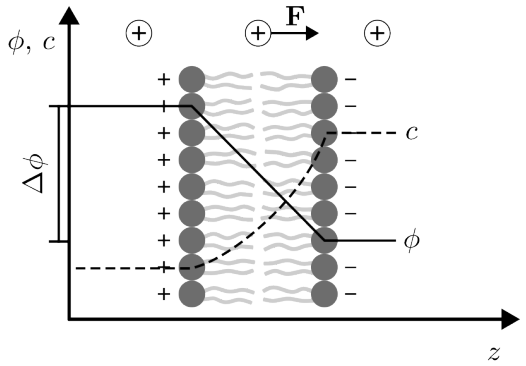

Figure 3.3: Electrostatic potential Φ and ion concentration c across the plasma membrane which is modeled as a parallel plate capacitor. In the inter-membrane region, the potential decreases linearly whereas the concentration follows $\sim e^{-q\Delta\Phi/(k_BT)}$ (equation 3.10). Since the electrical field of a charged plane does not depend on the distance from the plane (compare equation 3.3), the net field outside the membrane vanishes. Hence, there is a force on a charged test particle only if it is *within* the lipid bilayer.

	intracellular (mM)	extracellular (mM)	Nernst potential (mV)
K^+	155	4	-98
Na^+	12	145	67
Cl^-	4	120	-90
Ca^{2+}	10^{-4}	1.5	130

Table 3.1: Nernst potentials for some important ions in a typical mammalian muscle cell. Because the Nernst potentials of the different ion species differ strongly, this ionic distribution is an out-of-equilibrium situation. Resting potentials of excitable cells are in the range of -50 to $-90\,mV$.

From Eq. 3.7, the capacitance of the plane can be computed:

$$C = \frac{Q}{U} = \frac{A\sigma}{|\Delta\Phi|} = \frac{A\epsilon_0\epsilon}{d} \tag{3.8}$$

As an example, we choose a myelinated nerve cell membrane with $\epsilon = 2$ and $d = 2\,nm$. We then obtain for the capacitance of the nerve cell membrane:

$$\frac{C}{A} = \frac{\epsilon_0\epsilon}{d} \approx \frac{\mu F}{cm^2}$$

where F denotes the physical unit Farad. This value membrane capacity has been measured experimentally. Moreover, the measure of $1\,\frac{\mu F}{cm^2}$ is universally used in experiments to determine the area of any given cell or membrane patch. The concept of the biomembrane being a parallel circuit of a capacitor and an ohmic resistance forms the basis of electrophysiology (theory of action potentials according to Hodgkin and Huxley).

We now consider a single species of mobile ions that is free to distribute along z (e.g. ions diffusing through the hydrophobic part or through an ion channel of the membrane). At finite temperature T, there is a competition between electrostatic

forces and translational entropy. The concepts of energy stored in the form of chemical potential μ and electrostatic potential Φ can be combined in the so-called **electrochemical potential** (compare Eq. 1.31 for the chemical potential of an ideal gas):

$$\mu(z) = k_B T \ln c(z) + Ze\Phi(z) \tag{3.9}$$

where Z is the valency of the ion species. In equilibrium, $\mu(z)$ has to be constant:

$$\Rightarrow \quad \ln\left(\frac{c(z_1)}{c(z_2)}\right) = \frac{-Ze(\Phi(z_1) - \Phi(z_2))}{k_B T}$$

$$\Rightarrow \quad \boxed{c(z_2) = c(z_1) \cdot e^{-Ze\Delta\Phi/(k_B T)}} \qquad \textbf{Nernst equation} \tag{3.10}$$

Eq. 3.10 was first formulated by the German physical chemist Walter Nernst who won the Nobel prize in chemistry in 1920. It can be seen as Boltzmann's law for charges in an electrostatic potential (compare Fig. 3.3). In table 3.1 we give experimentally measured values for ion concentrations in a muscle cell. The corresponding Nernst potentials are calculated in the last column. One sees that they differ widely, proving that the distributions are out off equilibrium (ion pumps and channels redistribute them against the thermal forces).

Our discussion showed that mobile charges will lead to concentration profiles that depend on temperature and electrostatic potential. Therefore we now turn to **"electrostatistics"**, the field that combines these two elements.

3.3 Charged wall in different limits

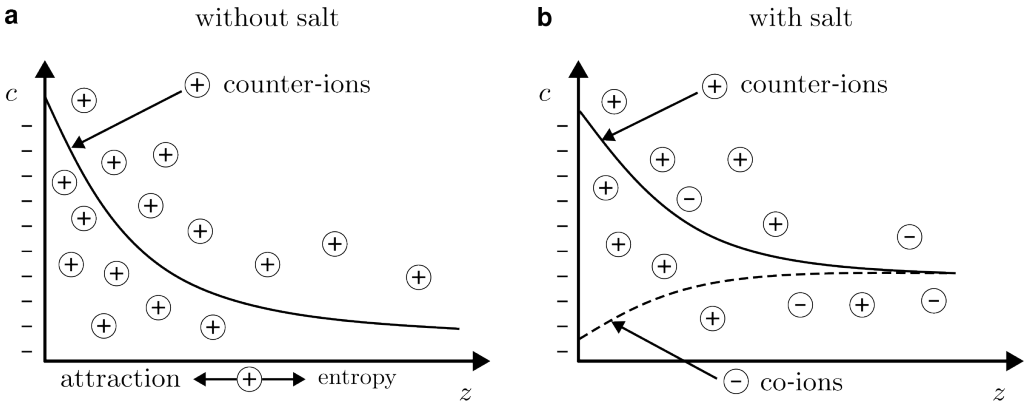

Figure 3.4: Concentration profile of counter-ions (here: positive) and co-ions (here: negative) in a solution (a) without salt and (b) with salt, at a distance z from the charged wall. The physiological concentration of salt is around $c_s = 100\,mM$.

At close approach, each object is locally flat (e.g. a globular protein or a colloid). We therefore start with the planar case as most instructive example. Consider a wall with an area charge density of σ and the corresponding counter-ions, e.g. dissociated groups of the charged object, in solution. Note, that the complete system does not carry a net charge, i.e. it is always charge neutral. Two cases

can be distinguished. First a solution containing only counter-ions, and second a solution with additionally added salt, hence also containing co-ions (see Fig. 3.4). These seemingly simple systems are in fact hard problems in theoretical physics. In the following, we will treat three special cases for the planar geometry:

1. high T or small charge density σ (no salt): In this case mean field theory (MFT) can be used to derive the **Poisson-Boltzmann theory**.

2. salt, $c_s \neq 0$: **Debye-Hückel theory**, will turn out to be a linearized Poisson-Boltzmann theory

3. low T or high charge density σ (no salt): **strong-coupling limit** (i.e. for DNA condensation)

All other cases are too complicated to be treated analytically and have to be investigated with Monte Carlo simulation.

Because counter-ions and co-ions are mobile, we have to deal with thermal averages. The first step is to formulate the Hamiltonian of the system, therefore we consider N counter-ions of valency Z at an oppositely charged wall with area density n_{2d} (the charge density thus is $\sigma = -en_{2d}$):

$$\frac{H}{k_BT} = \sum_{i<j} \underbrace{\frac{Z^2e^2}{4\pi\epsilon_0\epsilon k_BT \cdot r_{ij}}}_{\substack{\text{Coulomb interaction} \\ \text{between 2 counter-ions}}} + \sum_i \underbrace{\frac{Ze^2 n_{2d} z_i}{2\epsilon_0\epsilon k_BT}}_{\substack{\text{Coulomb interaction} \\ \text{between one counter-ion} \\ \text{and the wall}}} \tag{3.11}$$

We introduce two new length scales to write

$$\frac{H}{k_BT} = \sum_{i<j} \frac{Z^2 l_B}{r_{ij}} + \sum_i \frac{z_i}{\mu} \tag{3.12}$$

resulting in the following definitions:

1. The **Bjerrum length** $l_B = \frac{e^2}{4\pi\epsilon_0\epsilon k_BT}$ is the distance at which two unit charges interact with thermal energy. In water, where $\epsilon = 80$, we find $l_B = 7\,\text{Å}$, while in vacuum the value Bjerrum length is $5.6\,nm$ (both values computed for $T = 300\,K$).

2. The **Gouy-Chapman length** $\mu = (2\pi Z n_{2d} l_B)^{-1}$ marks the distance from a charged wall at which the potential energy of the charge equals k_BT. Note that in contrast to the definition of the Bjerrum length, we do not use a unit charge, but keep valency Z in the definition. For $Z = 1$, ambient temperature T and $n_{2d} = 1/nm^2$, one gets $\mu \approx 1\,nm$.

Because we focus on the effect of a wall, we now rescale all distances with μ:

$$\frac{H}{k_BT} = \sum_{i<j} \frac{\Xi}{\bar{r}_{ij}} + \sum_i \bar{z}_i \tag{3.13}$$

where

$$\Xi = \frac{Z^2 l_B}{\mu} = 2\pi Z^3 l_B^2 n_{2d} = \frac{Z^3 e^4 n_{2d}}{8\pi(\epsilon_0 \epsilon k_B T)^2} \qquad \textbf{coupling strength} \tag{3.14}$$

In Eq. 3.13, we rescaled the system such that only one dimensionless parameter, namely the coupling strength (Eq. 3.14), determines the behavior of the whole system.

At this point, we managed to end up with only one dimensionless parameter, that defines two asymptotic limits of interest:

1. $\Xi \ll 1$: This is the case if the system has a low charge density, a low valency and/or a high temperature. One can perform an expansion in small Ξ (mean-field theory) and ends up with the Poisson-Boltzmann theory.

2. $\Xi \gg 1$: In the strong-coupling limit, the system has a high charge density, a high valency and/or is prepared at a low temperature. Here a virial expansion in Ξ^{-1} can be made.

In order to understand the difference better between the two limits, we use charge neutrality

$$\frac{Ze}{\pi a_\perp^2} = \sigma = e n_{2d} \tag{3.15}$$

to introduce the typical lateral distance $a_\perp$ between counter-ions. Later we will see that both for weak and strong coupling, the average distance of the counterions to the wall is the Gouy-Chapman length μ. We therefore rescale also the lateral length with the Gouy-Chapman length:

$$\frac{a_\perp}{\mu} = \sqrt{\frac{Z}{n_{2d}\pi\mu^2}} = \sqrt{2\Xi} \tag{3.16}$$

This shows that Ξ determines the ratio between $a_\perp$ and μ (compare Fig. 3.5). For $\Xi \ll 1$, the lateral distance between the counter-ions is smaller than their average distance from the wall and they form a 3D cloud that has no structure in the lateral direction; therefore a mean field theory in z-direction is sufficient. For $\Xi \gg 1$, the lateral distance between the counter-ions is larger than their average distance from the wall and they form a 2D layer on the wall. For very strong coupling, this condensate can become a crystal.

3.4 Poisson-Boltzmann theory

Poisson-Boltzmann theory is a mean field theory that assumes local thermal equilibrium. We start with the Poisson equation from electrostatics (Eq. 1.61)

$$\Delta\Phi = -\frac{\rho(\vec{r})}{\epsilon_0 \epsilon}$$

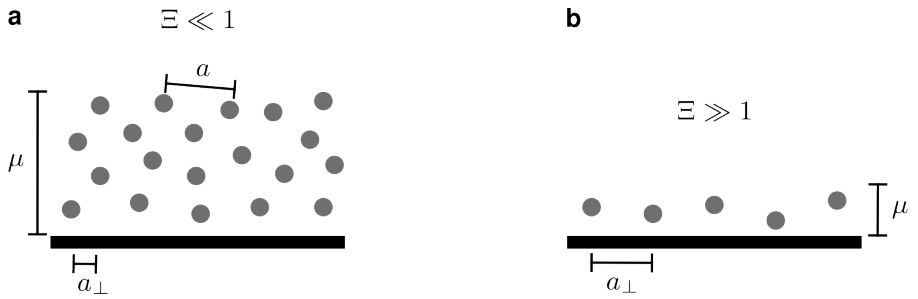

Figure 3.5: The two complementary limits considered here. (a) In the high temperature limit, the lateral distance of the counter-ions is smaller than the vertical extension and thus we get a liquid. This situation is described by a mean field theory in z-direction (Poisson-Boltzmann theory). (b) In the low temperature limit, the lateral distance is larger than the vertical extension and we get a condensate and possibly even a crystal (strong coupling limit).

and combine it with the Boltzmann distribution:

$$\rho(\vec{r}) \overset{\text{for simplicity } Z=1}{=} e \cdot n(\vec{r}) = e \cdot n_0 \cdot \exp\left(\frac{-e\Phi(\vec{r})}{k_B T}\right) \tag{3.17}$$

This results in

$$\Rightarrow \boxed{\Delta\Phi = -\frac{e}{\epsilon_0 \epsilon} \cdot n_0 \cdot \exp\left(-\frac{e\Phi}{k_B T}\right)} \qquad \textbf{Poisson-Boltzmann equation} \tag{3.18}$$

The Poisson-Boltzmann equation (PBE) is a non-linear differential equation of second order which is in general hard to solve analytically. In MD simulations, one usually employs PB-solvers (e.g. DelPhi, APBS, MIBPB, etc). There are only few cases for which it can be solved analytically.

Luckily, this is the case for the example of the charged wall. The boundary conditions are given by the charge neutrality of the whole system and by $|E(\infty)| = |-\Phi'(\infty)| = 0$:

$$\begin{aligned} \sigma &= \int_0^\infty dz \underbrace{\rho(z)}_{\substack{\text{charge density} \\ \text{of counter-ions}}} = -\epsilon_0 \epsilon \int_0^\infty \Phi'' \, dz \\ &= -\epsilon_0 \epsilon (\underbrace{\Phi'|_{z=\infty}}_{= -E(\infty) = 0} - \Phi'|_{z=0}) \\ \Rightarrow \quad \Phi'|_{z=0} &= \frac{\sigma}{\epsilon_0 \epsilon} \end{aligned}$$

With the boundary conditions, we get the analytical solution for the charged

	point charge	charged wall	with counter-ions (PBT)	with salt (DH)
Φ	$1/r$	z	$\ln(z)$	$\exp(-\kappa z)$
E	$1/r^2$	*const*	$1/z$	$\exp(-\kappa z)$

Table 3.2: Distance dependence of the electrostatic potential Φ and the electrostatic field E for different systems. Note that in comparison to a point charge a spatially extended distribution like the charged wall strengthens the interaction, whereas the presence of counter-ions (Poisson-Boltzmann theory) weakens the interactions. If, in addition, salt is added to the solution, the interaction is weakened to an even higher extent.

wall:

$$\text{Electrostatic potential} \qquad \Phi(z) = \frac{2k_BT}{e}\ln\left(\frac{z+\mu}{\mu}\right) + \Phi_0 \tag{3.19}$$

$$\text{Counter-ion density} \qquad n(z) = \frac{1}{2\pi l_B}\cdot\frac{1}{(z+\mu)^2} \tag{3.20}$$

Recall, that without counter-ions $\Phi \sim z$ and $E = const$ (compare Eq. 3.2 and Eq. 3.3; compare also table 3.2). This is now changed to a logarithmic scaling of the potential since a cloud of counter-ions surrounds any charged object and thus weakens the electrostatic potential. In other words, the charged wall is "screened" by the counter-ions. Together with the cloud or layer of counter-ions, the charged wall forms an electrostatic "double layer".

3.5 Debye-Hückel theory

Let us once again investigate the charged wall, now with a 1:1 electrolyte (i.e. NaCl) added to the solution. In this system, counter-ions as well as co-ions are present in the solution. Eq. 3.17 for the density of the ion species accounts for both counter-ions and co-ions with the same n_0 due to charge neutrality far from the wall. The PBE (Eq. 3.18) then reads:

$$\begin{aligned}
\Delta\Phi &= -\frac{e}{\epsilon_0\epsilon}(n_+ - n_-) \\
&= -\frac{e}{\epsilon_0\epsilon}\left(n_0\cdot\exp\left(\frac{-e\Phi}{k_BT}\right) - n_0\cdot\exp\left(\frac{+e\Phi}{k_BT}\right)\right) \qquad (3.21)\\
&= \frac{2e}{\epsilon_0\epsilon}\cdot n_0\cdot\sinh\left(\frac{e\Phi}{k_BT}\right) \qquad (3.22)
\end{aligned}$$

Note that the nice mathematical form of this equation arises because of the boundary condition that n_0 is the same for both the plus and minus co-ions at infinity. Interestingly, there exists an analytical solution for this equation. Here however we continue right away with a special case. For small $e\Phi/(k_BT)$, we can linearize Eq. 3.22 by using $\sinh(x) \approx x$ for small x. We then obtain

$$\boxed{\Delta\Phi = \kappa^2\Phi} \qquad \textbf{Debye-Hückel equation} \tag{3.23}$$

l_B	μ	l_{DH}
7 Å	$1\,nm$	$1\,nm$

Table 3.3: Values for the three electrostatic length scales Bjerrum length l_B, Gouy-Chapman length μ and Debye-Hückel screening length l_{DH} at physiological conditions. Note that the three electrostatic lengths are very similar (all around $1\,nm$).

with the Debye-Hückel screening length

$$l_{DH} = \frac{1}{\kappa} = \left(\frac{\epsilon_0\epsilon \cdot k_B T}{2e^2 n_0}\right)^{1/2} = (8\pi l_B n_0)^{-1/2} \tag{3.24}$$

$$l_{DH} = \begin{cases} 1\,\mu m & \text{pure water, } 10^{-7}\,M,\ H_3O^+ : OH^- \\ 10\,nm & 1\,mM\ NaCl \\ 1\,nm & 100\,mM\ NaCl \text{ (cytoplasma)} \\ 3\,\text{Å} & 1\,M\ NaCl \end{cases}$$

which adds a third typical length scale to the two (Bjerrum length and Gouy-Chapman length) we already introduced before (see also table 3.3).

The solution of the Debye-Hückel equation for a charged wall is simply

$$\Phi(z) = \frac{\sigma}{\epsilon_0\epsilon\kappa} e^{(-\kappa z)} \tag{3.25}$$

where we again employed the boundary condition $\Phi'(z=0) = -\sigma/(\epsilon_0\epsilon)$ due to charge neutrality.

In contrast to the result obtained by the PB theory where no salt was added to the solution, Eq. 3.25 exhibits an exponential decay. Thus, the interaction is short-ranged. In general, the more salt is added to the solution, the smaller is the screening length l_{DH} and the more the charged wall is screened by the counter-ions.

The DHE (Eq. 3.23) can also be solved analytically for other geometries than the charged wall, for instance for spherical symmetry. Consider a sphere with radius R (e.g. an ion, a protein, a micelle, a vesicle, a virus or a cell).

$$\Delta\Phi = \frac{1}{r}\frac{d^2}{dr^2}(r\Phi) = \kappa^2\Phi$$

$$\Rightarrow \quad \Phi = \frac{R\phi_R}{r} \cdot \exp(-\kappa(r-R)) \tag{3.26}$$

where ϕ_R denotes the surface potential. It follows from Gauss' law (Eq. 1.62) and charge neutrality:

$$E_R = \frac{Q_V}{4\pi\epsilon_0\epsilon R^2} = -\Phi'|_{r=R} = \frac{\phi_R(1+\kappa R)}{R}$$

$$\Rightarrow \quad \phi_R = \frac{Q_V}{4\pi\epsilon_0\epsilon \cdot (1+\kappa R)R} \tag{3.27}$$

Two special cases of Eq. 3.26 are particularly interesting:

1. No salt added to the solution, hence $\kappa \to 0 \;\Rightarrow\; \Phi = \dfrac{Q_V}{4\pi\epsilon_0\epsilon r}$. This limit results in the well-known Coulomb law.

2. Point charge ($R \to 0$): Then the potential takes the form

$$\Phi = \frac{Q_V \cdot \exp(-\kappa r)}{4\pi\epsilon_0\epsilon r} \qquad \text{Yukawa potential} \tag{3.28}$$

   Eq. 3.28 is the Green's function (or propagator) for the linear Debye-Hückel theory. Like for the Coulomb interaction, one can calculate Φ for any extended object (i.e. a line, a plane, etc.) by superposition of the propagator.

3.6 Strong coupling limit

To obtain a solution in the low-temperature limit for our example of the charged wall, a virial expansion via a complicated field theory has to be performed [13]. However, since this is not subject to this course, only the result for the ion distribution near a charged wall is given here:

$$n(z) = 2\pi l_B (n_{2d})^2 e^{-z/\mu} \qquad \textbf{Strong coupling limit} \tag{3.29}$$

It has to be noted that although Eq. 3.29 exhibits an exponential decay, it is not comparable to the derivation of the DHE and its solution for the charged wall. The latter was derived by the linearization of the PBE, whereas the result shown here has been derived independently from PBT. Note that the relevant length scale of Eq. 3.29 is the Gouy-Chapman length μ, and not the Debye-Hückel length l_{DH}.

3.7 Two charged walls

Now we want to investigate the case of two charged walls facing each other by making use of the theories introduced so far, i.e. the PB, the DH and the SC theories. The picture of two charged walls is actually the simplest model for the interaction between two particles. The interaction of charged particle surrounded by counter-ions is not only important in biology, but also e.g. in the earth sciences. In Fig. 3.6 the formation of river deltas is given as an instructive example.

3.7.1 Poisson-Boltzmann solution

Consider two charged walls which both carry a charge density σ facing each other at a distance d (compare Fig. 3.7a. We start with the PBE:

$$\Phi'' = -\frac{e}{\epsilon_0\epsilon} \cdot \underbrace{n_0 \exp\left(-\frac{e\Phi}{k_B T}\right)}_{n}$$

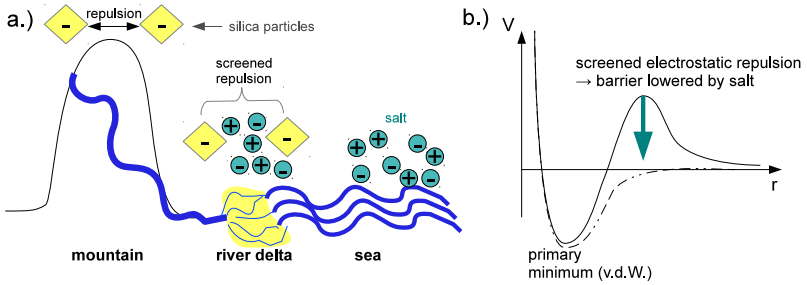

Figure 3.6: The formation of river deltas as a consequence of the interaction of two charged particles in salty solution. (a) A river flows from the mountains into the sea. On its way, negatively charged silica particles dissolve in the water which repel each other due to their charge. As the low-salt water of the river meets the sea water with high salinity, the repulsion between the particles is screened. They aggregate and, hence, form the river delta. (b) Effect of the salt ions on the potential energy. Screening lowers the energy barrier responsible for the repulsion. The corresponding description is known as DLVO-theory in colloidal sciences.

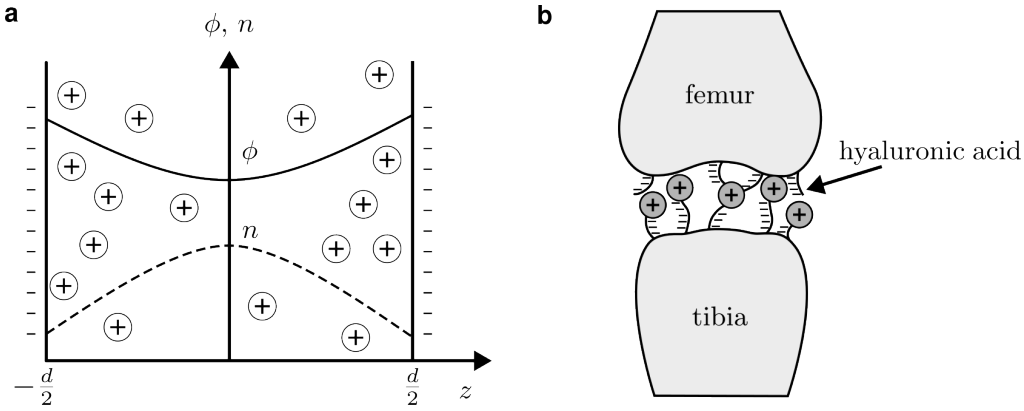

Figure 3.7: (a) Poisson-Boltzmann solution for the potential Φ and the counter-ion density n between two charged walls with charge densities $\sigma_1 = \sigma_2 = \sigma$. (b) The human knee is stabilized by cartilage containing hyaluronic acid (HA). Hyaluronic acid is a long, high molecular mass polymer of disaccharids, which is negatively charged and therefore responsible for the disjoining pressure caused by its counter-ions.

The two boundary conditions are:

$$\begin{aligned} \text{symmetry}: \quad & \Phi'(0) = 0 \\ \text{charge neutrality}: \quad & \sigma = -\int_0^{d/2} \rho \, dz = \epsilon_0 \epsilon \int_0^{d/2} \Phi'' \, dz = \epsilon_0 \epsilon \Phi' \left(\frac{d}{2}\right) \\ & \Rightarrow \; \Phi' \left(\frac{d}{2}\right) = \frac{\sigma}{\epsilon_0 \epsilon} \end{aligned}$$

This results in the exact solution of the PBE:

$$\text{Potential} \qquad \Phi(z) = \frac{k_B T}{e} \ln\left[\cos^2\left(K \cdot z\right)\right] \tag{3.30}$$

$$\text{Counter-ion density} \qquad n(z) = \frac{n_0}{\cos^2\left(K \cdot z\right)} \tag{3.31}$$

where n_0 denotes the counter-ion density at the mid plane and K denotes a constant which follows from the boundary condition:

$$\Phi'\left(\frac{d}{2}\right) = \frac{\sigma}{\epsilon_0 \epsilon} = \frac{2k_B T \cdot K}{e} \tan\left(\frac{K \cdot d}{2}\right) \tag{3.32}$$

Eq. 3.32 has to be solved numerically for K. A graphical representation of the analytic result of potential and charge density is shown in Fig. 3.7a.

Interestingly, the charges tend to accumulate at the sides, although the electrostatic forces between the two equally-charged plates cancel each other. This leads to a strong **"disjoining pressure"** (counter-ion pressure).

For two membranes with $\sigma = e/nm^2$ facing each other at a distance $d = 2\,nm$ and a mid-plane concentration $n_0 = 0.7\,M$, the counter-ion density at the plates is $n(d/2) = 12\,M$. This implies that the density is increased by a factor of 18.5 over a distance of only $1\,nm$. In this case, the potential difference is $\Delta\Phi = -74\,mV$. One can also compute the disjoining pressure and in the limit of small separation ($d \ll l_B$), it obeys an ideal gas equation (without proof):

$$p = k_B T \cdot n_0 = 17\,atm \tag{3.33}$$

where $1\,atm \cong 10^5\,Pa$. It can be seen directly that the disjoining pressure is very large and this has many applications in biological systems. For example, disjoining pressure can be found in joints and is actually the reason why we can go jogging (compare Fig. 3.7b).

3.7.2 Debye-Hückel solution

Let us now assume that there is additional salt in between the charged walls. Since the DH equation is a linear differential equation, the solution for this system is simply a superposition of the solution of two single charged walls (Eq. 3.25). One then gets

$$\Phi'' = \kappa^2 \Phi \quad \Rightarrow \quad \Phi = \Phi_0 \cosh(\kappa z) \tag{3.34}$$

Thus, the DH solution for Φ (as well as for n and p, respectively) decays exponentially with the distance and, hence, the interaction is short-ranged.

3.7.3 Strong coupling limit

The counter-ion density between two charged walls in the strong coupling limit turns out to be relatively flat. In detail it is constant in zero order and parabolic

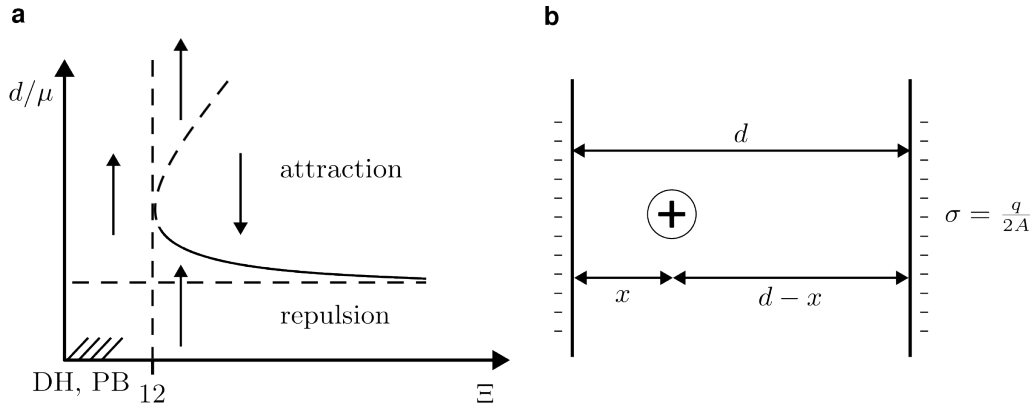

Figure 3.8: (a) Phase diagram showing regions of attraction and repulsion as a function of plate separation d/μ and coupling strength Ξ [13]. (b) Small strip of two charged walls with an in-between counter-ion.

in first order of the virial expansion. Thus superficially it appears to be similar to the PB result. In practise, however, the results are very different, because one finds that the two equally charged walls can in principle attract each other. Whether the interaction between the two planes is attractive or repulsive depends on the distance d and the coupling strength Ξ, as shown in the phase diagram in Fig. 3.8a. The very fact that attraction can occur offers a solution to our DNA riddle.

A simple explanation for this behavior can be given as follows: consider the condensed situation as sketched in Fig. 3.8b. Because the counter-ions condense with a relatively large lateral distance to each other, we neglect their interaction and only consider the interactions of one counter-ion with the wall in a small strip with area $A = -\frac{q}{2\sigma} > 0$. There are three contributions to the electrostatic energy now: the two interactions of the counter-ion with the two walls and the interaction of the walls with each other:

$$\begin{aligned} \frac{U_{el}}{k_B T} &= -2\pi(l_B/e^2)q\sigma x - 2\pi(l_B/e^2)q\sigma(d-x) - 2\pi(l_B/e^2)\sigma(\sigma\cdot A)d \\ &= -\pi(l_B/e^2)\sigma q d = 2\pi(l_B/e^2)\sigma^2 A d \end{aligned} \tag{3.35}$$

The energy is minimal for $d \to 0$ which leads to attraction of the two charged walls. For the electrostatic and the entropic pressure we get

$$\text{electrostatic pressure:} \qquad p_{el} = -\frac{\partial}{\partial d}\left(\frac{U_{el}}{A}\right) = \frac{-2\pi l_B \sigma^2 k_B T}{e^2}$$

$$\text{entropic pressure:} \qquad p_{en} = \frac{k_B T}{A\cdot d} = -\frac{2\sigma k_B T}{q d}$$

$$\Rightarrow \text{balanced at equilibrium distance} \qquad \boxed{d = -\frac{e^2}{\pi l_B q \sigma} = 2\mu} \tag{3.36}$$

The strong coupling limit is biologically relevant, because for $n_{2d} = 1\,nm^{-2}$ it can be reached with trivalent counter-ions. In fact, the charged polymer DNA

uses many multivalent counter-ions such as speridine and spermine which support DNA condensation in the nucleus. Again the existence of an equilibrium distance also has consequences in other sciences. E.g. it explains why clay particles can be swollen only to a certain distance.

3.8 Electrostatistics of viruses

In the beginning of this chapter, we asked the question how DNA as a charged polymer can be kept spatially confined such that the distance between the charges is in the range of nm (which is the case in a nucleus or in a virus). We can answer this now with the help of the previous section: the DNA can be in a condensed state due the effect of counterions with high valency. In the nucleus, it is organized in highly complex structure with several levels of organization in order to form chromosomes. Therefore a more accessible model system is DNA-organisation in viruses.

3.8.1 The line charge density of DNA

We already know that DNA is highly charged. Until now we assumed that every base pair carries two negative charges, in other words we assumed that every segment of the DNA was fully dissociated and therefore the linear charge density was $\lambda = 2e/(3.4\,\text{Å})$. We will now see why this assumption can indeed be made.

In water, DNA dissociates H^+ as a counter-ion into the surrounding solution:

$$\text{DNA} \rightleftharpoons \text{DNA}^- + \text{H}^+ \tag{3.37}$$

The law of mass action gives us the dissociation constant for reaction formula 3.37.

$$K_D = \frac{[\text{H}^+] \cdot [\text{DNA}^-]}{[\text{DNA}]} \tag{3.38}$$

Due to the many orders of magnitude spanned by K_D values, a logarithmic measure of the dissociation constant is more commonly used in practice.[1]

$$pK := -\log_{10} K_D = \underbrace{-\log_{10}\left[\text{H}^+\right]}_{=pH} - \log_{10}[\text{DNA}^-] + \log_{10}[\text{DNA}] \tag{3.39}$$

$$\Rightarrow pK = pH - \log_{10}\frac{[\text{DNA}^-]}{[\text{DNA}]} \qquad \begin{matrix}\text{Henderson-Hasselbalch}\\ \text{equation}\end{matrix} \tag{3.40}$$

The pK corresponds to the pH at which half of the groups have dissociated ($[\text{DNA}^-] = [\text{DNA}]$).

[1] pure water: $\left[\text{H}^+\right] = 10^{-7}\,M \Rightarrow pH = 7$

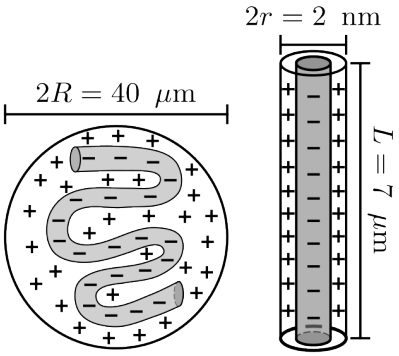

Figure 3.9: Simple model of viral DNA packed in the capsid of the $\phi 29$ bacteriophage.

For DNA, we find $pK = 1$ which implies that DNA is a very strong acid. In cells, $pH = 7.34$. With the Henderson-Hasselbalch equation the fraction of dissociated DNA can immediately be calculated.

$$\frac{[\mathrm{DNA}^-]}{[\mathrm{DNA}]} = 10^{6.34}$$

Thus, DNA in the cell is completely dissociated and, therefore, carries a line charge density of

$$\boxed{\lambda = \frac{2e}{3.4\,\text{Å}}} \qquad \begin{matrix}\text{linear charge density} \\ \text{of DNA}\end{matrix} \tag{3.41}$$

3.8.2 DNA packing in $\phi 29$ bacteriophage

Now we want to focus on DNA packing in viruses. Actually, a virus is not a living object per definition, but rather genetic material, i.e. DNA or RNA, packed into a protein shell, the so-called capsid. Typically, the diameter of a capsid is in the range of tens to hundreds of nm. Some viruses, e.g. HIV, are in addition wrapped by a lipid bilayer (and are then called "enveloped virus").

As we shall see in the following, the RNA and DNA in viruses is very densely packed. Take for instance the $\phi 29$ bacteriophage (a virus infecting *E.Coli)*: Its capsid can be approximated as a sphere of radius $R_{capsid} = 20\,nm$ containing $20\,kbp$ (corresponding to $L = 2 \cdot 10^4 \cdot 0.34\,nm = 7\,\mu m$) DNA. We assume $V_{bp} \approx 1\,nm^3$ (compare Fig. 3.9). The **packing ratio** in the capsid can be computed directly:

$$\frac{2 \cdot 10^4\,nm^3}{\frac{4\pi}{3}\,(20\,nm)^3} \approx 0.6 \tag{3.42}$$

Comparing this value with the maximal packing density of spherical objects into a crystal (≈ 0.71) it can be concluded that DNA packed into a viral capsid must be close to a crystalline structure. Indeed this can be shown by electron microscopy.

If we now pack DNA with the line charge density $\lambda = 2e/(3.4\,\text{Å})$ into the virus, how much electrostatic energy do we have to put into the system? Electrostatic

energy is the work to bring a charge distribution into its own field and is known to be

$$U_{el} \quad = \frac{1}{2} \int \Phi(\vec{r}) \cdot \rho(\vec{r})\, d\vec{r} \tag{3.43}$$

where the factor 1/2 is needed to avoid double-counting each interaction. We model the DNA in the virus as a fully charged sphere. The potential at the surface of a sphere with radius r and charge density ρ follows from Gauss law as

$$\Phi(r) \quad = \quad \underbrace{\frac{1}{4\pi\epsilon_0\epsilon} \cdot \frac{1}{r}}_{\text{point charge in origin}} \quad \cdot \quad \underbrace{\rho \cdot \frac{4\pi}{3} r^3}_{\text{charge in smaller sphere}} \quad = \frac{\rho r^2}{3\epsilon_0\epsilon} \tag{3.44}$$

For the total work, we have to add up shell after shell of the sphere:

$$\begin{aligned} \Rightarrow U_{el} \quad &= \int_0^R dr\, \Phi(r) \cdot \left(\rho \cdot 4\pi r^2\right) \\ &= \int_0^R dr\, \frac{4\pi}{3\epsilon_0\epsilon} \rho^2 r^4 = \frac{4\pi}{15\epsilon_0\epsilon} \rho^2 R^5 \\ &= \frac{1}{4\pi\epsilon_0\epsilon} \cdot \frac{3Q^2}{5R} \end{aligned} \tag{3.45}$$

where we have used $Q = \rho \frac{4\pi}{3} R^3$. Here the factor 1/2 does not arise because every contact is counted only once as we gradually build up the sphere. [2] For our example of the $\phi 29$ bacteriophage, we have $Q = 2e/bp \cdot 20kbp$ and hence

$$U_{el} = 10^8 pN \cdot nm \tag{3.46}$$

The work needed to pack the DNA into the viral capsid has been measured in a single molecule experiment [14]. However, in this experiment the work was determined to be much smaller than the one estimated above:

$$W_{exp} \approx \frac{1}{2} 7000\ nm \cdot 60\ pN = 2.1 \cdot 10^5\, pN \cdot nm \tag{3.47}$$

Obviously the above estimate was much too high because we neglected the effect of the counter-ions.

There are $N = 4 \cdot 10^4$ counter-ions packed with the genome (corresponding to 2 counter-ions/bp). We now assume complete neutralization of the charges and consider only the loss of entropy due to the DNA volume:

$$U_{ci} \quad = \quad N k_B T \cdot \ln \frac{V_{free}}{V_{capsid}} \tag{3.48}$$

The volume V_{free} is that of the screening cloud (recall that $L \approx 7\,\mu m$, $R_{DNA} \approx 1\,nm$, $R_{capsid} \approx 20\,nm$ and $l_{DH} \approx 1\,nm$).

$$V_{free} \quad = \quad L\pi \left[(R_{DNA} + l_{DH})^2 - R_{DNA}^2 \right] = 6.6 \cdot 10^4\, nm^3 \tag{3.49}$$

$$V_{capsid} \quad = \quad \frac{4\pi}{3} R_{capsid}^3 - L\pi R_{DNA}^2 = 1.2 \cdot 10^4\, nm^3 \tag{3.50}$$

$$\Rightarrow U_{ci} \quad = \quad 3 \cdot 10^5\, pN \cdot nm \tag{3.51}$$

[2] Eq. 3.43 can still be used and leads to the same result if we use in it the expression for the potential *inside* a uniformly charged sphere, $\phi(r) = \frac{\rho(3R^2 - r^2)}{6\epsilon_0\epsilon}$ (valid for $r < R$).

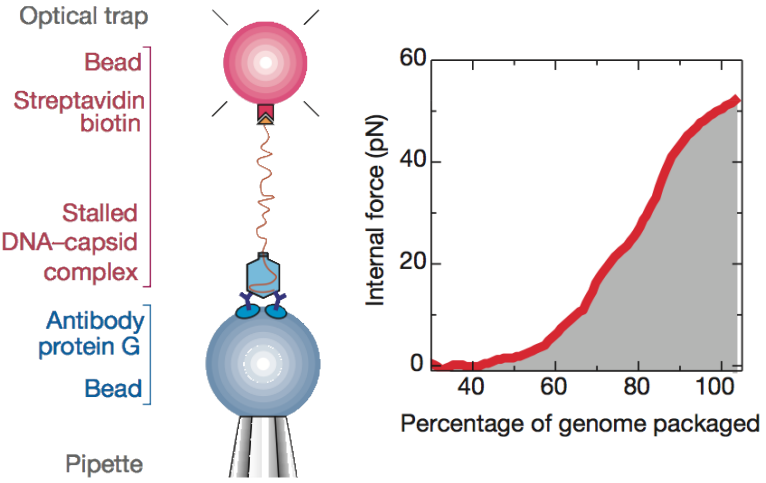

Figure 3.10: Left panel: Experimental set-up of the portal motor force experiment. A single $\phi 29$ packaging complex is tethered between two microspheres. Optical tweezers are used to trap one microsphere and measure the forces acting on it, while the other microsphere is held by a micropipette. Right panel: Internal force as the function of % genome packed. Note that 100% of the genome corresponds to $7\,\mu m$ DNA and that the work is obtained by integration of the force (grey area). Images and caption text (partly) taken from reference [14].

This result is much closer to the experimental value. A full analysis had to also include the effect of bending the DNA, which requires polymer physics.

Finally the pressure inside the capsid can be calculated:

$$\begin{aligned} p &= \frac{Nk_BT}{V} = \frac{4 \cdot 10^4 \cdot 4.1\,pN \cdot nm}{\frac{4\pi}{3}\,(20\,nm)^3} \\ &\approx 5\,\frac{pN}{nm^2} = 50\,atm \end{aligned} \tag{3.52}$$

This is a huge counter-ion pressure inside the capsid, as was also experimentally confirmed.

3.8.3 Electrostatistics of viral capsid assembly

Before the DNA can be inserted into the viral capsid by a molecular motor, the capsid itself has to be assembled (for RNA viruses, genome and capsid are often co-assembled, because RNA is more flexible than DNA and therefore more easy to bend during assembly). Viral capsids assemble from so-called capsomers and often form an icosahedral lattice, because this is close to the shape of a sphere which gives the optimal volume to area ratio. For many viruses like Hepatitis B virus (HBV, compare Fig. 3.11a), assembly is sufficiently robust to also occur in the test tube from the capsomers alone. This proves that it is a spontaneously occuring process that is driven by some gain in Gibbs free energy. We consider two major contributions: a contact energy between the capsomers driving the process and an electrostatic energy opposing it (note that charges are required to

stabilize the capsomers and the capsid in solution against aggregation, although this is unfavorable for assembly):

$$\Delta G = \Delta G_{contact} + \Delta G_{electro} \tag{3.53}$$

The equilibrium constant K then follows as (assuming a dilute solution)

$$\ln K = -\frac{\Delta G}{k_B T} \tag{3.54}$$

For HBV, K has been measured as a function of temperature T and salt concentration c_s [15], compare Fig. 3.11b-d. Because this virus assembly from 120 capsomers in an all-or-nothing manner, we do not have to consider intermediates and can write a law of mass action:

$$K = \frac{[capsid]}{[capsomer]^{120}} \tag{3.55}$$

The fraction of complete capsids can be measured by size exclusion chromatography and then be fitted to the corresponding isotherm (with a Hill coefficient of 120). This procedure works very well and gives curves for $K(T, c_s)$.

The experimental data gives two main results. First the slope of $K(T, c_s)$ as a function of T does not depend on c_s, suggesting that assembly is driven mainly by contact interactions. The strong temperature dependence points to entropic effects and suggests a hydrophobic interaction, similar to the one driving micelle formation, protein folding or lipid membrane assembly. Second K increases with c_s, suggesting that increased salt screens the electrostatic repulsion and thus promotes assembly.

In a theoretical analysis, it has been shown that these experimental results can be fitted nicely using Debye-Hückel theory [16]. We start from the surface potential of a sphere of radius R in Debye-Hückel theory (Eq. 3.27):

$$\phi_R = \frac{Q_V}{4\pi\epsilon_0\epsilon \cdot (1+\kappa R)R} = \frac{Q_V}{4\pi\epsilon_0\epsilon}\frac{l_{DH}}{R(R+l_{DH})} \,. \tag{3.56}$$

The electrostatic energy of the charged spherical shell is now

$$U = \frac{1}{2}Q\phi_R = \frac{1}{2}k_B T \left(\frac{Q}{e}\right)^2 \frac{l_{DH} l_B}{R(R+l_{DH})} \,. \tag{3.57}$$

With $l_{DH} = 1nm$ and $R = 14nm$ we can write $(R + l_{DH}) \approx R$. Therefore our final result for the salt-dependent part of the equilibrium constant reads

$$\ln K = -\frac{\Delta G_{electro}}{k_B T} = -\frac{1}{2}\left(\frac{Q}{e}\right)^2 \frac{l_{DH} l_B}{R^2} \tag{3.58}$$

Thus $\ln K$ should scale linearly with the screening length l_{DH} and therefore with $c_s^{-1/2}$, exactly as it is observed experimentally, compare Fig. 3.11d.

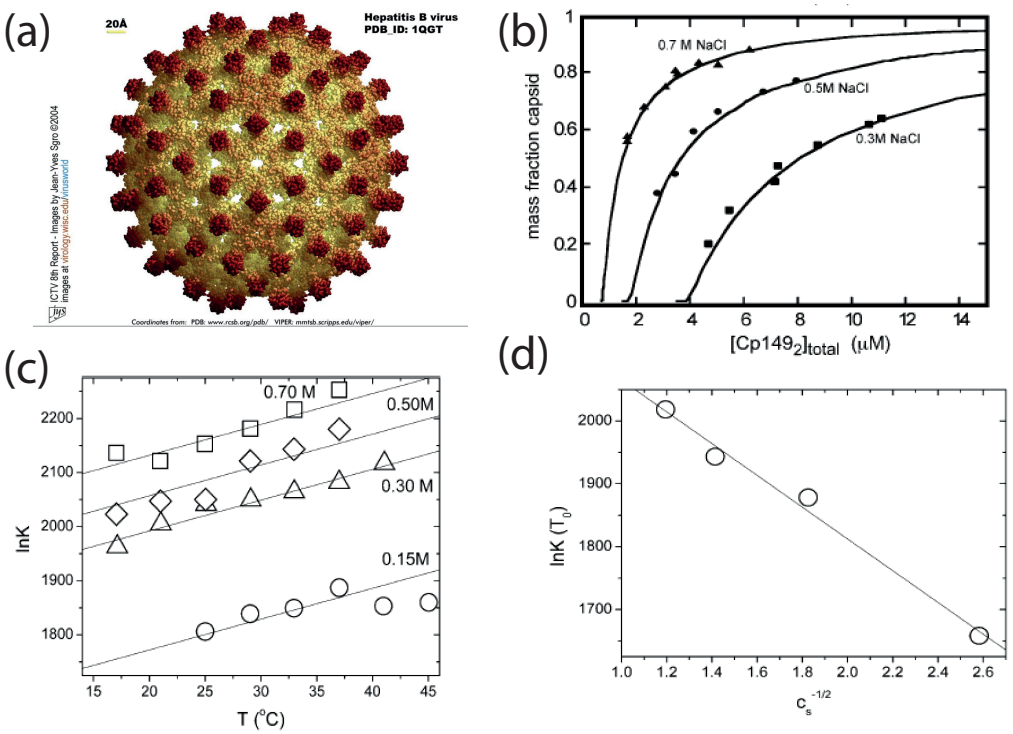

Figure 3.11: (a) Molecular rendering of the structure of the capsid of hepatitis B virus (HBV). (b) Assembly isotherms at different salt concentrations. (c) Fit of equilibrium constant as a function of temperature and salt concentration. (d) Scaling of equilibrium constant with salt concentration. Experimental data from Zlotnick group, theory by van der Schoot group.

Chapter 4

Binding and assembly

Due to the high temperature and low interaction energies, the biomolecules in the cell are in constant motion and continuously bump into each other. Once this happens, their biomolecular interactions decide whether they bind to each other or not. The main functions of binding are information transfer, transport and assembly. We now ask how one can describe the statistics arising from many binding events. We will see that the appropriate formalism is essentially the grandcanonical ensemble and that this will allow us to calculate binding curves as function of monomer concentration, using the concept of the binding polynomial. The most important example for such a binding processes is the cooperative binding of oxygen to hemoglobin, which we will discuss in detail, including the MWC-model by Monod, Wyman and Changeux. We then turn to the assembly of cytoskeletal filaments, especially actin, which not only can grow to large sizes, but also solved the problem of polarized growth and treadmilling. Finally we discuss the assembly of micelles and viruses, which again have a finite size, but complex assembly pathways, that need to avoid kinetic trappling and malformed structures.

4.1 Binding polynomial

Consider a protein P that has t binding sites for a ligand X with concentration $[X] = x$. For each complex we write a reaction equation:

$$P + X \to PX_1 \tag{4.1}$$
$$P + 2X \to PX_2 \tag{4.2}$$
$$\dots \tag{4.3}$$
$$P + tX \to PX_t \tag{4.4}$$

Note that these equations do not describe the actual dynamics, but only the binding equilibria that have to exist in a statistical sense. For each equation we have a law of mass action:

$$\frac{[PX_i]}{[P]x^i} = K_i \tag{4.5}$$

which reaction constants K_i, which have units of [concentration]$^{-i}$. The larger K_i, the more favorable the reaction.

We now ask which fraction is in state i:

$$\frac{[PX_i]}{[P]+[PX_1]+\cdots+[PX_t]} = \frac{K_i x^i}{Q(x)} \tag{4.6}$$

where a factor of $[P]$ has canceled and we have defined the *binding polynomial*

$$Q(x) = 1 + K_1 x + \cdots + K_t x^t = \sum_{i=0}^{t} K_i x^i \tag{4.7}$$

with $K_0 := 1$. We next calculate the number of bound ligands:

$$\langle i \rangle = \frac{\sum_i i K_i x^i}{Q} = \frac{x}{Q}\frac{dQ}{dx} = \frac{d\ln Q}{d\ln x} \ . \tag{4.8}$$

So we see that the binding polynomial generates this result simply by a derivative, using a trick which is well known from statistical mechanics: xd_x generates the number i when applied to x^i. The function of $Q(x)$ is exactly the one of the grandcanonical partition sum Z_G in statistical physics or of a generating function G in probability theory.

For the second moment we have

$$\langle i^2 \rangle = \frac{\sum_i i^2 K_i x^i}{Q} = \frac{x}{Q}\frac{d}{dx}\left(x\frac{dQ}{dx}\right) \ . \tag{4.9}$$

The mean squared deviation (MSD) then follows from

$$\langle (\Delta i)^2 \rangle = \langle (i - \langle i \rangle)^2 \rangle = \langle i^2 \rangle - \langle i \rangle^2 \tag{4.10}$$

and is a measure for the size of the fluctuations.

In the following we will discuss this formalism for three different cases: $t = 1, 2$ and 4, with the last one being the case of hemoglobin.

One binding site

We now have only one reaction

$$P + X \to PX \tag{4.11}$$

and one reaction equilibrium

$$\frac{[PX]}{[P]x} = K \tag{4.12}$$

We then find

$$Q(x) = 1 + Kx \tag{4.13}$$

$$\langle i \rangle = \frac{Kx}{1+Kx} \tag{4.14}$$

$$\langle i^2 \rangle = \frac{Kx}{1+Kx} = \langle i \rangle \tag{4.15}$$

thus the first two moments are identical. The result for the first moment is known as the *Langmuir isotherm* because it also arises from the grandcanonical ensemble of a two-state system. It has a hyperbolic shape on a linear scale and a sigmoidal shape on a logarithmic scale. The MSD has a maximum at intermediate values of x, similar to the specific heat of a two-state system (*Schottky hump*).

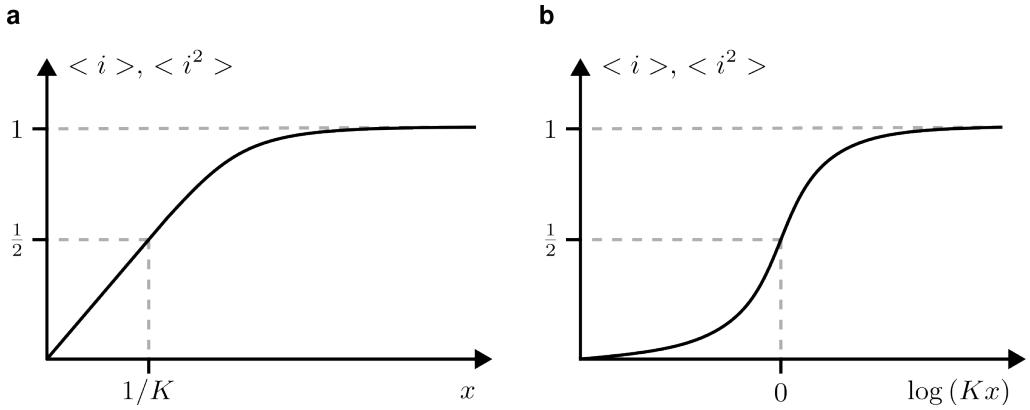

Figure 4.1: (a) First and second moment as a function of concentration $x = [X]$. (b) First and second moment on a logarithmic scale.

Two binding sites

We start with the site-based approach and distinguish between binding sites a and b. We now have three equilibrium reaction

$$P + X \to P_a X \tag{4.16}$$
$$P + X \to P_b X \tag{4.17}$$
$$P + 2X \to P X_2 \tag{4.18}$$

and three corresponding laws of mass action. We consider the average number of bound ligands:

$$\langle i \rangle = \frac{[P_a X] + [P_b X] + 2[P X_2]}{[P] + [P_a X] + [P_b X] + [P X_2]} = \frac{d \ln Q}{d \ln x} \tag{4.19}$$

with

$$Q(x) = 1 + K_a x + K_b x + K_c x^2 \ . \tag{4.20}$$

For two independent binding sites (no cooperativity) we have $K_c = K_a K_b$ and thus

$$Q(x) = 1 + K_a x + K_b x + K_a K_b x^2 = (1 + K_a x)(1 + K_b x) \ . \tag{4.21}$$

For the binding curve we get the sum of two Langmuir isotherms:

$$\langle i \rangle = \frac{K_a x}{1 + K_a x} + \frac{K_b x}{1 + K_b x} \ . \tag{4.22}$$

Positive cooperativity would imply $c = K_c/(K_a K_b) > 1$ and the binding polynomial would not factorize.

In the stochiometric approach, we do not distinguish between sites a and b and only consider two reaction:

$$P + X \to PX_1 \tag{4.23}$$
$$PX_1 + X \to PX_2 \tag{4.24}$$

with reaction constants K_1 and K_2. The binding polynomial Q now reads

$$Q(x) = 1 + K_1 x + K_1 K_2 x^2 \ . \tag{4.25}$$

Comparing with the site-based approach gives $K_1 = K_a + K_b$ and $K_1 K_2 = K_c$.

Four binding sites

This is the case of hemoglobin, which can bind four oxygen atoms with high cooperativity. Without cooperativity, we would have

$$Q(x) = (1 + Kx)^4 = 1 + 4Kx + 6(Kx)^2 + 4(Kx)^3 + (Kx)^4 \tag{4.26}$$

where the binomial coefficients reflect the different ways to distribute the zero to four ligands over the four binding sites. For the first moment we would simply have

$$\langle i \rangle = \frac{4Kx}{1 + Kx} \ . \tag{4.27}$$

that is a Langmuir isotherm with four ligands in saturation. Experimentally, however, it was realized early on that the binding curve is much steeper, more closely to a Hill binding curve

$$\langle i \rangle = \frac{4Kx^n}{1 + Kx^n} \tag{4.28}$$

with an effective Hill coefficient of $n \approx 3$. In the literature, different suggestions have been made to explain such binding curves. While Adair (1925) simply used four different reaction constants, Pauling (1935) came up with a model that has only one more parameter, namely the energy gain for a pairwise interaction between two neighboring ligands on a tetrahedron. Although this model fits the experiments nicely, it does not reflect the additional experimental fact that hemoglobin is allosteric, which means that it can exist in two states called T (tense) and R (relaxed). In 1965, Monod, Wyman and Changeux introduced a model based on this observation. Today the MWC-model is the standard model for cooperativity in binding curves.

We assume that the T-state is more stable than the R-state in the absence of oxygen, $[T]/[R] = L > 1$. On the other hand, however, oxygen X binds better to R than to T:

$$R + X \to RX \tag{4.29}$$
$$T + X \to TX \tag{4.30}$$

with $K_R > K_T$. Thus once X is present, the whole system shifts towards R, which in turn binds even more X, thus having positive cooperativity. The binding polynomial for this model is

$$Q(x) = \frac{(1 + K_R x)^4 + L(1 + K_T x)^4}{1 + L} \tag{4.31}$$

leading to

$$\langle i \rangle = \frac{d \ln Q}{d \ln x} = \frac{4K_R x(1 + K_R x)^3 + 4LK_T x(1 + K_T x)^3}{Q(1 + L)} \tag{4.32}$$

which indeed is similar to a Hill curve with $n \approx 3$.

4.2 Growth of cytoskeletal filaments

We now turn our attention to a supramolecular complex that can grow to large size, which holds true for cytoskeletal filaments like actin. We denote the aggregates by P_n (because they are polymers) and we only consider growth by monomer addition (alternatively, all sizes could interact with each other, leading to the coagulation-fragmentation equation going back to Smoluchowski and Kolmogorov; the monomer addition scheme treated here is a special case known as the Becker-Döring equations). Again choosing the stochiometric approach, we have

$$\frac{[P_n]x}{[P_{n-1}]} = K_d \tag{4.33}$$

where now we do not use the reaction constant K, but its inverse $K_d = 1/K$, the dissociation constant. Note that K_d has the dimension of concentration and in fact it is the concentration at half-occupancy (when $[P_n] = [P_{n-1}]$). The smaller K_d, the stronger the reaction (the larger the reaction constant K) and the fewer monomers are required to reach half-occupancy. We also assume that the reaction constant does not depend on the aggregate size n, because to first approximation, only the local interface should matter. In marked contrast to micelle and virus assembly, now the aggregate can grow to infinite size, which means that n can run to infinity.

Like before, by iteration we can write the concentration of the intermediates:

$$[P_n] = K_d \left(\frac{x}{K_d}\right)^n = K_d e^{-\alpha n} \tag{4.34}$$

where we have defined $\alpha = -\ln(x/K_d)$, which is possible for $x < K_d$. Thus for a fixed concentration x below the dissociation constant K_d, there will be an exponential distribution of polymer sizes. However, if concentration approaches K_d from below, polymer size will diverge. Thus $x_c = K_d$ is the analogue to the critical micelle concentration where assembly suddenly kicks in, similar to a phase transition, but for a finite-sized system.

For actin, an order of magnitude estimate is $K_d = k_{off}/k_{on} = (1/s)/(10/\mu M s) = 0.1\mu M$. However, the typical actin monomer concentration in cells is $x = 30\mu M$.

This means that actin in cellular conditions always wants to grow. To regulate this process, cells use capping proteins that locally suppress growth. Addition of one actin monomers corresponds to a increase in length of $a = 2.75$ nm. The growth velocity follows as $v = k_{on}ax = \mu m/s$, which indeed is a typical value observed experimentally.

Growth velocity is reduced by dissociation, leading to

$$\frac{dL}{dt} = ak_{on}x - ak_{off} \tag{4.35}$$

again resulting in the critical concentration $x_c = k_{off}/k_{on} = K_d$. Growth would be further reduced if monomer starvation existed, that is if overall actin concentration would be fixed and monomers were used up during growth. Here we assume that we have a unlimited reservoir for monomers which fixes concentration x.

We now ask the question how biological filaments manage to treadmill, that is one end shrinks while the other end grows such that overall length is constant. In our simple model, $dL/dt = 0$ is only possible at x_c, but then both ends are stalled. To break this symmetry, both ends have to have different rates, that is k_{off}^+ and k_{on}^+ at the plus end and k_{off}^- and k_{on}^- at the minus end (for actin, these two ends are called the *barbed* and *pointed* ends, respectively). However, the ratio of these rates at each side should be the same, because they have the same binding interface and therefore the same free energy difference ΔG, leading to the same reaction constant. This in turn implies that both ends either shrink or grow, thus they have no possibility to have different behaviour at the same monomer concentration x.

Here nature has invented an ingenious solution, namely a different chemical nature for the two ends using ATP-hydrolysis. The barbed end mainly binds ATP-actin, forming an ATP-cap at the barbed end, which is also the fast growing end. With time ATP is converted into ADP and the pointed end mainly binds ADP-actin. In this way, the two interfaces have different binding energies and therefore two different critical concentrations emerge: $K_d^+ = 0.5\mu M$ and $K_d^- = 8\mu M$. For one unique value in this window, one now can get treadmilling, namely when the growth velocities at the two ends are exactly equal and opposite.

For microtubules, the situation is slightly different, here treadmilling is not required and one end typically is fixed to some nucleation center, e.g. the centrosome. In order to still keep average length constant while allowing for growth, nature has invented another trick, namely occasional catastrophes, when suddenly the whole polymer collapses back to a small size.

4.3 Micelle assembly

Cytoskeletal filaments essentially have a linear assembly pathway. As an example of self-assembly into a complex that does not have a linear assembly pathway, we now discuss the formation of micelles, which are spherical assemblies of surfactants (*surface active molecules*), e.g. tensides or lipids, which shield their

hydrophobic tails from the contact with water by forming a droplet. Typicallly a micelle contains 60 surfactant molecules with cone shapes, that means with bulky head groups of molecular surface area above 60 Å^2. Below this value cylindrical micelles will form, and planar bilayers below 40 Å^2. Here however we only discuss the spherical case.

In principle, the surfactants could assemble into aggegrates A_n of arbitrary size $n = 1, 2, 3, \ldots$. For each size we have an reaction equilibrium as above. The monomer concentration is $x = [A_1]$ and the fraction of molecules in aggregates is

$$\nu(x) = \frac{x + 2K_2x^2 + 3K_3x^3 + \ldots}{x + K_2x^2 + K_3x^3 + \ldots} = \frac{1 + 2K_2x + 3K_3x^2 + \ldots}{1 + K_2x + K_3x^2 + \ldots} \tag{4.36}$$

and as before $K_n = e^{-\beta\Delta\mu_n^0}$. A famous model by Tanford and Israelachvili suggests that the chemical potential should single out an optimal micelle size through surface effects. The larger the micelle, the larger the surface energy desribed by the surface tension γ between the oily and aqueous parts. A too small surface area however is also unfavorable because then the polar headgroups would start to repel each other too much. They suggested the following equation

$$\Delta\mu^0(a) = \gamma a + \frac{c}{a} \tag{4.37}$$

which leads to an optimal micelle surface area $a = a^* = (c/\gamma)^{1/2}$. Then we can rewrite the chemical potential as

$$\Delta\mu^0(a) = \frac{\gamma}{a}(a - a^*)^2 + 2\gamma a^* \approx \frac{\gamma}{a^*}(a - a^*)^2 + 2\gamma a^* \tag{4.38}$$

where the approximation would be a Taylor expansion around $a = a^*$. If we now insert this result into the Boltzmann factor, we can conclude that the micelle size will have a Gaussian distribution around $a = a^*$. This suggests that micelle formation is essentially a two-state process, with monomers coexisting with fully assembled micelles of size $a = a^*$. Indeed this is observed experimentally: at the critical micelle concentration (CMC), fully developed micelles start to develop and monomer concentration plateaus. The CMC can be deduced from a two-state equilibrium between A_1 and A_n with $K = [A_n]/x^n$. Then

$$\nu(x) = \frac{x + nKx^n}{x + Kx^n} = \frac{1 + nKx^{n-1}}{1 + Kx^{n-1}} \tag{4.39}$$

and the CMC is $x_c = K^{-1/(n-1)}$.

4.4 Virus capsid assembly

Viruses come in many different sizes and shapes, but a typical virus is spherical and has a diameter of 100 nm. As a rule of thumb, animal RNA-viruses like Influenza A, Ebola, HIV 1 or SARS-CoV-2 tend to be enveloped by a membrane and therefore assemble at some membrane of the host cell. They also tend to have structural proteins that form a capsid, but this capsid often assembles at

the membrane. Here SARS-CoV-2 is a bit special because its structural proteins do not form a completely connected capsid, in contrast to Influenza A, Ebola or HIV-1. RNA-viruses also tend to assemble their capsid together with the genome, because RNA is relatively easy to bend (see the chapter on biopolymers). In contrast, DNA is relatively hard to bend and therefore DNA-viruses tend to first assemble a capsid and then to fill it with the genome (e.g. bacteriophages, Papilloma, Herpes or smallpox), often with the help of a portal motor. Non-enveloped viruses tend to have a very stable protein capsid that often can assemble in the test tube without any other proteins than the ones needed for the coat. Note however that these are only rules of thumb and that the real situation is much more complex, with many exceptions to these rules. For example, hepatitis B is a DNA-virus and has a very regular capsid that can be assembled in the testtube, but in addition it is enveloped. Many plant viruses such as cowpea mosaic virus (CPMV) or cowpea chlorotic mottle virus capsid (CCMV) form beautiful capsids and are not enveloped, but they are RNA-viruses. Disregarding this diversity, in the following we discuss the assembly of protein capsids from few proteins as a paradigm for the assembly of supramolecular complexes with clear cut structure.

Virus capsid assembly is similar to micelle assembly, in the sense that it also turns out to be essentially a two-state system between monomers and the assembled capsid (see below), but the target structure is even more defined because it is a solid protein lattice and not a fluid droplet. It has been noted by Francis Crick and Jim Watson (who also discovered the structure of DNA) that most viruses are spherical or cylindrical because they are made essentially from one protein, so each point on the surface must be equivalent. In addition, however, they must form a lattice. Closed shells with a lattice in which each point is equivalent are the five Platonic solids. Donald Kaspar and Aaron Klug therefore concluded that spherical viruses must have icosahedral symmetry, because the icosahedron is the Platonic solid that comes closest to the sphere (largest number of subunits, namely 20 triangles). As a simple model for a virus capsid, we now discuss a dodecahedron (12 pentagons)[1]. As the dual to the icosahedron, it has the same symmetry properties, but it is easier to treat because it has fewer subunits. Examples for real world viruses which have similar structures would be Polio, Hepatitis B or CCMV. If the capsomeres (monomers for the capsid) are pentagons, this implies that they already have preassembled (typically from five identical viral proteins) before the real capsid assembly starts.

We first argue that there is a linear pathway to assembly, from the monomer A_1 through the intermediates A_n to the final capsid A_{12}. The reason is that each addition of an additional monomer takes the route of maximal energy gain, which corresponds to the maximal number of new edges in the lattice. For example, A_3 should be a rosette rather than a chain of three pentagons, because then the gain is $f_3 = 2$ and not only $f_3 = 1$ new edges. In the table, we list the number of new edges which one gets over the whole sequence. Note that energy goes always downhill and that the last addition (filling in one missing pentagon in

[1]This model has been published as Adam Zlotnick, To build a virus capsid - an equilibrium model for the self-assembly of polyhedral protein complexes, J. Mol. Biol. 241: 59-67, 1994.

n	2	3	4	5	6	7	8	9	10	11	12
f_n	1	2	2	2	3	2	3	3	3	4	5
S_n	5/2	2/3	3/2	4/2	1/5	5/1	2/4	2/3	3/2	2/5	1/12

Table 4.1: Two important numbers characterizing the step $A_{n-1} \to A_n$ in the assembly of a dodecahedral virus capsid: the number f_n of newly established edges characterizing the energy gain, and the entropic degeneracy S_n, which is the ratio of number of ways to build up A_n to the number of ways to dissociate A_n.

the dodecahedron) leads to the largest gain in energy. Each edge comes with an energy gain around $\Delta\epsilon \approx -5k_BT$ and typically results from hydrophobic patches at the sides of the capsomers (compare the chapter on electrostatistics).

Taking the stochiometric approach, we can write the reaction equilibrium for each step as ($x = [A_1]$ as before)

$$\frac{[A_n]}{[A_{n-1}]x} = K_n = K_0 S_{in} S_n e^{-\beta f_n \Delta\epsilon} \tag{4.40}$$

which includes two statistical factor. $S_{in} = 5$ is the number of ways an incoming pentagon can dock. S_n is the ratio of the number of ways to form the new intermediate to the number of ways to dissociate it. For example, we can add a third pentagon to A_2 in two ways, and there are three ways to remove one of the pentagons from A_3. Thus we would have

$$K_3 = K_0 5 \frac{2}{3} e^{-\beta 2\Delta\epsilon} \ . \tag{4.41}$$

Note that because $\Delta\epsilon$ is negative, this gives a relatively large Boltzmann weight.

As before, we now can obtain an equation of the concentration of all aggregates by iteration:

$$[A_n] = K_0^{n-1} {S_{in}}^{n-1} \left(\prod_{i=2}^{n} S_i \right) e^{-\beta\Delta\epsilon \sum_{i=2}^{n} f_i} x^n \tag{4.42}$$

If one plots this distribution, one sees that all values are very low, except the ones for A_1 (monomers are always present due to entropy) and A_{12} (the full capsid is the end point and has the highest energy gain). Like for micelles, we can look at this as a two-state system. We write the concentration of the capsid using all the numbers given above

$$[A_{12}] = K_0^{11} 5^{11} \frac{1}{12} e^{-30\beta\Delta\epsilon} x^{12} \ . \tag{4.43}$$

Note that the number of edges should be $12 \cdot 5/2 = 30$, as seen here, but also follows from the factor f_n given in the table. The statistical factors present the entropy of building the capsid. In particular, the factor 1/12 is the product of all S_n given in the table. We now define an effective reaction constant and an effective free energy difference by

$$K_{eff} = \frac{[A_{12}]}{x^{12}} \ , \Delta G_{eff} = -k_B T \ln \frac{K_{eff}}{K_0} \ , \tag{4.44}$$

leading to

$$\Delta G_{eff} = 30\Delta\epsilon - k_B T \ln\left(\frac{5^{11}}{12}\right) \ . \tag{4.45}$$

Obviously the first term is the overall energy gain, and the second defines the entropy of building a capsid.

Chapter 5

Physics of membranes and red blood cells

In a cell, lipid bilayers partition space into functional compartments. This central aspect of lipid bilayers must have been crucial for the development of life. Lipid bilayers are the carriers of many vital processes, including ion separation and transport as well as protein activity. In general, cell membranes regulate the transfer of material and information in and out of cells.

Due to its low bending energy and the thermal environment, the lipid bilayer is in continuous motion. In order to describe the energetics and statistics of membranes, we have to introduce a mathematical description of surfaces and then to identify the corresponding energy (Helfrich bending Hamiltonian). Therefore, we start with a crash course in differential geometry[1]. We then discuss the Helfrich bending Hamiltonian in much detail and its consequences for shapes of minimal energy and thermal fluctuations around these shapes. As a reference point, we always discuss surfaces under tension (e.g. soap bubbles or oil droplets). Finally we discuss the physics of red blood cells, whose shapes and fluctuations can be described well by surface Hamiltonians. However, in contrast to pure membranes, the presence of the actin-spectrin network makes it necessary to add additional terms to the interface Hamiltonian.

[1]There are many books on differential geometry, for example the one by Michael Spivak (Comprehensive introduction to differential geometry, vols 1-5, 1979). Here are two books in German that are especially helpful for membrane physics: MP do Carmo, Differentialgeometrie von Kurven und Flächen, 3rd edition Vieweg 1993; JH Eschenburg and J Jost, Differentialgeometrie und Minimalflächen, 2nd edition Springer 2007. The classical review on vesicle shapes is Udo Seifert, Configurations of fluid membranes and vesicles, Advances in Physics 46: 13-137, 1997. A great resource is also the script by JL van Hemmen, Theoretische Membranphysik: vom Formenreichtum der Vesikel, TU Munich 2001, available at http://www.t35.physik.tu-muenchen.de/addons/publications/Hemmen-2001.pdf from the internet.

5.1 A primer of differential geometry

5.1.1 Curves in 3D

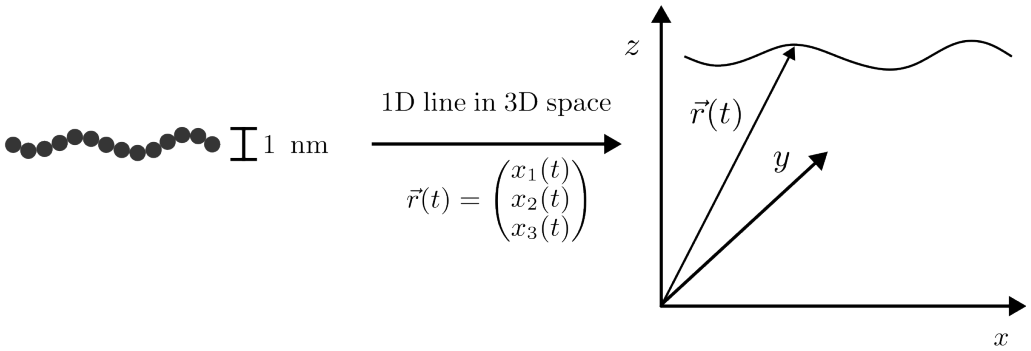

Figure 5.1: Polymers can be mathematically described as one-dimensional curves in a three-dimensional space.

Parametrization and arc length of curves

Consider a curve in 3 dimensions, e.g. a helical curve with radius R and pitch $z_0 = b \cdot \frac{2\pi}{\omega}$ (figure 5.2, parametrized by an internal coordinate t:

$$\vec{r}(t) = \begin{pmatrix} x_1(t) \\ x_2(t) \\ x_3(t) \end{pmatrix} = \begin{pmatrix} R \cdot \cos(\omega t) \\ R \cdot \sin(\omega t) \\ b \cdot t \end{pmatrix} \tag{5.1}$$

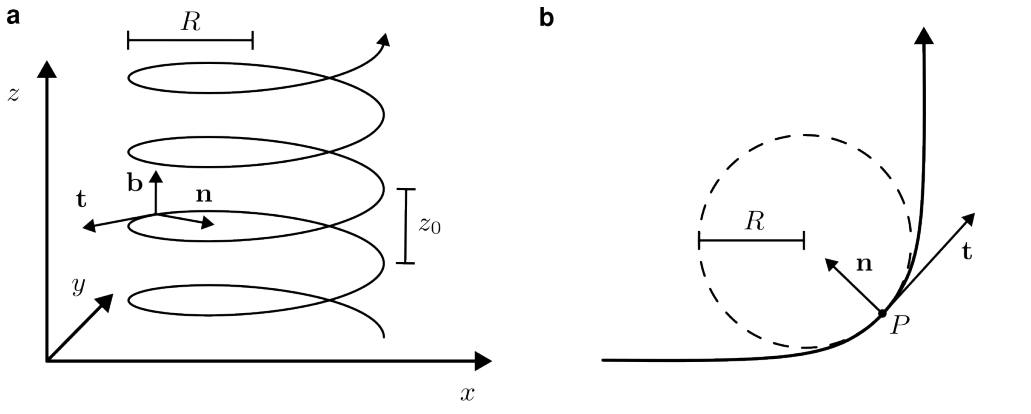

Figure 5.2: **a** Helical curve with radius R and pitch $z_o = b \cdot 2\pi/\omega$. The tangential vector $\vec{t}$, the normal vector $\vec{n}$ and the binormal vector $\vec{b}$ are sketched in blue. **b** Kissing circle at a point $P(s)$ with radius $R(s) = \kappa^{-1}(s)$.

In the limit $b \to 0$, the helix becomes a circle, and in the limit $b \to \infty$, it becomes

a straight line. For the velocity of the helix we get:

$$\begin{aligned} \vec{v} = \frac{d\vec{r}}{dt} = \dot{\vec{r}} &= \begin{pmatrix} -R\omega \cdot \sin(\omega t) \\ R\omega \cdot \cos(\omega t) \\ b \end{pmatrix} \\ \Rightarrow v &= \sqrt{R^2\omega^2 + b^2} > R\omega \end{aligned}$$

An important quantity when describing a curve is its arc length L which is independent of the parametrization that was chosen.

$$\begin{aligned} L &= \int_{t_0}^{t_1} dt \left|\dot{\vec{r}}\right| \overset{t=t(u)}{=} \int_{t_0}^{t_1} dt \left|\frac{d\vec{r}}{du}\right| \cdot \left|\frac{du}{dt}\right| \\ &= \int_{u_0}^{u_1} du \left|\frac{d\vec{r}}{du}\right| \end{aligned} \tag{5.2}$$

The **arc length** along a curve

$$s(t) = \int_{t_0}^{t} dt' \left|\dot{\vec{r}}(t')\right| \tag{5.3}$$

can be used to parametrize the curve since it increases strictly with t ($\dot{s} = \left|\dot{\vec{r}}\right| > 0$) and can therefore be inverted to $t = t(s)$.

$$\Rightarrow r = r(s) = r(t(s)) \qquad \begin{matrix} \text{parametrization by} \\ \text{arc length (}\mathbf{PARC}\text{)} \end{matrix} \tag{5.4}$$

For example, for the helical curve we find

$$\begin{aligned} v = \sqrt{R^2\omega^2 + b^2} = \frac{ds}{dt} = const \\ \Rightarrow s = v \cdot t \Rightarrow t = \frac{s}{v} \Rightarrow \vec{r} = \begin{pmatrix} R \cdot \cos(\frac{\omega s}{v}) \\ R \cdot \sin(\frac{ws}{v}) \\ \frac{bs}{v} \end{pmatrix} \end{aligned}$$

The co-moving frame

The co-moving frame (also called "Frenet frame") of a curve consists of three mutually perpendicular unit vectors:

$$\textbf{tangential vector} \qquad \vec{t}(s) := \frac{\dot{\vec{r}}}{|\dot{\vec{r}}|} \overset{\text{PARC}}{=} \frac{\frac{d\vec{r}}{ds} \cdot \left|\frac{ds}{dt}\right|}{\left|\frac{ds}{dt}\right|} = \frac{d\vec{r}}{ds} \tag{5.5}$$

$$\textbf{normal vector} \qquad \vec{n}(s) := \frac{d\vec{t}}{ds} \cdot \left|\frac{d\vec{t}}{ds}\right|^{-1} = \frac{1}{\kappa}\frac{d\vec{t}}{ds} \tag{5.6}$$

$$\textbf{binormal vector} \qquad \vec{b}(s) := \vec{t}(s) \times \vec{n}(s) \tag{5.7}$$

The normalization in equation 5.5 is not required for PARC. Therefore, PARC is also called the "natural parametrization". In equation 5.6 we defined the **curvature** κ of the curve at a given point

$$\kappa := \left|\frac{d\vec{t}}{ds}\right| \tag{5.8}$$

which defines the radius of curvature $R(s) = \kappa^{-1}$. This is the radius of the so-called "kissing circle" at that specific point (figure 5.2.

E.g. for the helical path we get:

$$\vec{t} = \frac{d\vec{r}(s)}{ds} = \begin{pmatrix} -\frac{R\omega}{v} \cdot \sin(\frac{\omega s}{v}) \\ \frac{R\omega}{v} \cdot \cos(\frac{\omega s}{v}) \\ \frac{b}{v} \end{pmatrix} \quad \Rightarrow \quad |\vec{t}| = \frac{R^2\omega^2}{v^2} + \frac{b^2}{v^2} = 1 \surd$$

$$\frac{d\vec{t}}{ds} = \begin{pmatrix} -\frac{R\omega^2}{v^2} \cdot \cos(\frac{\omega s}{v}) \\ -\frac{R\omega^2}{v^2} \cdot \sin(\frac{ws}{v}) \\ 0 \end{pmatrix} \quad \Rightarrow \quad \begin{aligned} \kappa &= \tfrac{R\omega^2}{v^2} = \tfrac{R\omega^2}{R^2\omega^2+b^2} \\ &= \frac{1}{\left(R+\frac{b^2}{R\omega^2}\right)} < \frac{1}{R} \end{aligned}$$

The curvature of the helical path is smaller than for a circle. In the limit $b \to 0$, we have $\kappa = 1/R$, denoting a perfect circle. In the limit $b \to \infty$, κ vanishes, denoting a straight line.

The derivatives of the vectors of the co-moving frame are described in the same basis through the **Frenet formulae**:

$$\begin{aligned} \frac{d\vec{t}}{ds} &= \kappa\vec{n} \\ \frac{d\vec{n}}{ds} &= -\kappa\vec{t} + \tau\vec{b} \\ \frac{d\vec{b}}{ds} &= -\tau\vec{n} \end{aligned} \tag{5.9}$$

where we introduced the **torsion** τ:

$$\tau = -\frac{d\vec{b}}{ds} \cdot \vec{n} = \frac{d\vec{n}}{ds} \cdot \vec{b} \tag{5.10}$$

τ measures how strongly the curve is twisted out of the plane. E.g. for the helical path

$$\tau = -\vec{n} \cdot \frac{d\vec{b}}{ds} = \frac{b\omega}{v^2} = \frac{b\omega}{R^2\omega^2 + b^2} \xrightarrow[\text{or } b\to 0]{b\to\infty} 0$$

5.1.2 Surfaces in 3D

Tangential vectors, normal and curvatures

We next consider a surface in 3 dimensions. For the parametrization, we need two internal parameters x and y:

$$\vec{f}(x,y) = \begin{pmatrix} f_1(x,y) \\ f_2(x,y) \\ f_3(x,y) \end{pmatrix} \tag{5.11}$$

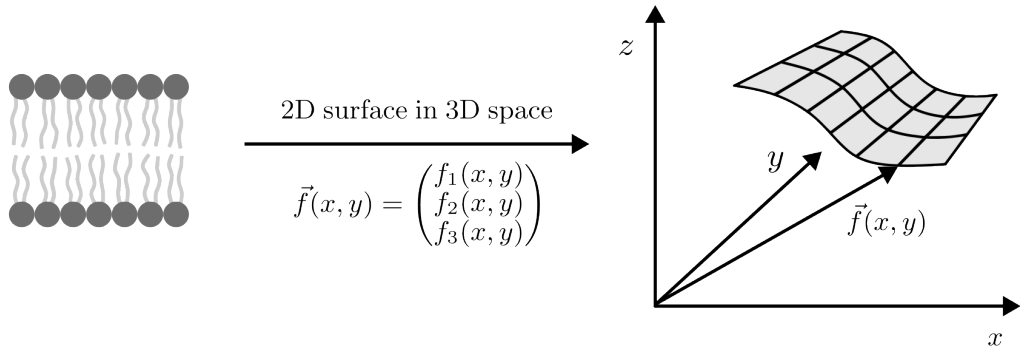

Figure 5.3: Membranes can be mathematically described as two-dimensional surfaces in a three-dimensional space.

The tangential vectors $\partial_x \vec{f}$ and $\partial_y \vec{f}$ span the tangential plane (compare figure 5.4a). The unit normal vector then is defined as

$$\vec{n} \quad = \quad \frac{\partial_x \vec{f} \times \partial_y \vec{f}}{\left| \partial_x \vec{f} \times \partial_y \vec{f} \right|} \tag{5.12}$$

Note that in contrast to the case of space curves, we do not normalize the tangential vectors.

In order to introduce definitions for the curvature, we can construct a plane containing $\vec{n}$ which we then rotate by 180 degrees through a given point (x, y) on the surface, as sketched in figure 5.4b. The kissing circle for each span curve defined by a rotation angle Θ of the plane gives us a curvature in this certain direction (figure 5.4c).

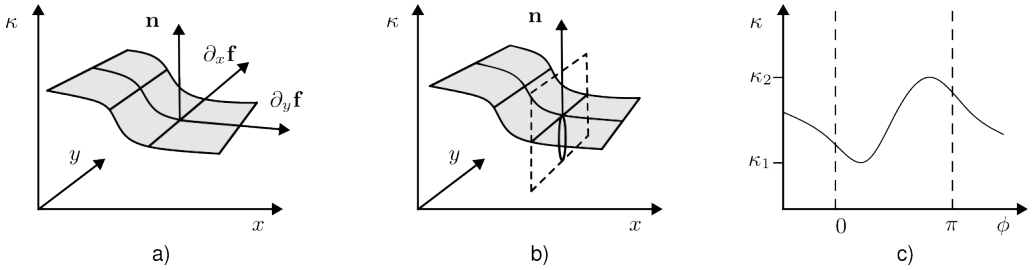

Figure 5.4: a) Surface in a 3D space with tangential vectors $\partial_x \vec{f}$ and $\partial_y \vec{f}$ and unit normal vector $\vec{n}$ perpendicular to the tangential vectors. b) Plane (gray) containing $\vec{n}$ and rotating. c) For each position Θ of the rotating plane a curvature can be determined.

The curvature will have a minumum κ_1 and a maximum κ_2, the so-called "**principal curvatures**". With these two curvatures and the radii of the corresponding kiss-

ing circles R_1 and R_2, respectively, we can define two important concepts:

$$\textbf{Mean curvature:} \qquad H := \frac{\kappa_1 + \kappa_2}{2} = \frac{1}{2}\left(\frac{1}{R_1} + \frac{1}{R_2}\right) \tag{5.13}$$

$$\textbf{Gaussian curvature:} \qquad K := \kappa_1 \cdot \kappa_2 = \frac{1}{R_1 \cdot R_2} \tag{5.14}$$

H and K can be used to classify a point (x, y) on a surface: If $K(x, y) > 0$, it is called elliptic point or sphere-like, if $K(x, y) < 0$, it is called hyperbolic or saddle-like, and if $K(x, y) = 0$, it is called parabolic or cylinder-like. Three examples with constant K are shown in table 5.1.

	Sphere (elliptic)	Saddle (hyperbolic)	Cylinder (parabolic)
Example	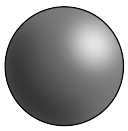	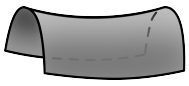	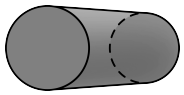
Radii of kissing circles	$R_1 = R_2 = R$	$R_1 = -R_2$	$R_1 = R$, $R_2 = \infty$ (straight line)
Mean curvature	$H = \frac{1}{R}$	$H = 0$	$H = \frac{1}{2R}$
Gaussian curvature	$K = \frac{1}{R^2} > 0$ (cannot be mapped onto plane)	$K = -\frac{1}{R_1^2} < 0$	$K = 0$ (can be mapped onto plane)

Table 5.1: H and K can be used to classify surfaces. For the examples shown here, K is constant, and hence each point on the surface is elliptic, hyperbolic or parabolic, respectively.

For the Gaussian curvature K, Gauss formulated two important theorems:

1. **Theorema egregium** (Latin: "remarkable theorem"): K depends only on the inner geometry of the surface. The normal $\vec{n}$ is not required to calculate it. In fact there exists an explicit formula to calculate K from the two tangent vectors and their derivatives, without the need to use the normal.

2. **Gauss-Bonnet theorem**: K integrated over a *closed* surface is a topological constant.

$$\oint dA\, K \quad = \quad 2\pi\chi \tag{5.15}$$

where χ is the so-called "Euler characteristic". It can be used to calculate the number of handles G ("genus") of a surface:

$$\chi \quad = \quad 2 - 2 \cdot G \tag{5.16}$$

Because χ is a topological quantity, one can calculate it from topologically equivalent polyhedra (for examples, see table 5.2). Then one can use the **Euler theorem**:

$$\chi = F - E + V \qquad \begin{array}{ll} \text{F:} & \text{Number of faces} \\ \text{E:} & \text{Number of edges} \\ \text{V:} & \text{Number of vertices} \end{array} \tag{5.17}$$

Recipe from differential geometry

In order to evaluate integrals like $\int dA\, K$, one needs formulae for $dA = dA(x,y) = f_A(x,y)\, dxdy$ and $K = K(x,y)$. To this end, we calculate the three 2×2 matrices g, h and a. Let us first define the symmetric matrix g, also called "first fundamental form" or "metric tensor":

$$\boxed{g_{ij} := \partial_i \vec{f} \cdot \partial_j \vec{f} = \begin{pmatrix} \left|\partial_x \vec{f}\right|^2 & \partial_x \vec{f} \cdot \partial_y \vec{f} \\ \partial_x \vec{f} \cdot \partial_y \vec{f} & \left|\partial_y \vec{f}\right|^2 \end{pmatrix}} \qquad \textbf{metric tensor} \tag{5.18}$$

$$\Rightarrow g_{ij}^{-1} = \frac{1}{\det g} \begin{pmatrix} \left|\partial_y \vec{f}\right|^2 & -\partial_x \vec{f} \cdot \partial_y \vec{f} \\ -\partial_x \vec{f} \cdot \partial_y \vec{f} & \left|\partial_x \vec{f}\right|^2 \end{pmatrix} \tag{5.19}$$

where $\det g = \left|\partial_x \vec{f} \times \partial_y \vec{f}\right|^2$. g_{ij} depends on $\partial_x \vec{f}$ and $\partial_y \vec{f}$, but not on the unit normal $\vec{n}$. It describes the metrics in the surface:

$$A(S) \quad = \quad \int_S dxdy \left|\partial_x \vec{f} \times \partial_y \vec{f}\right| = \int_S dxdy \, (\det g)^{1/2} \tag{5.20}$$

The "second fundamental form" is defined as

$$h_{ij} := -\partial_i \vec{n} \cdot \partial_j \vec{f} \overset{\vec{n} \cdot \partial_i \vec{f} = 0}{=} \vec{n} \cdot \partial_i \partial_j \vec{f}$$

$$\Rightarrow \boxed{h_{ij} = \vec{n} \cdot \partial_{ij} \vec{f}} \qquad \textbf{second fundamental form} \tag{5.21}$$

which, in contrast to the metric tensor, depends on the unit normal $\vec{n}$.
With the matrices g and h, the matrix a can be defined:

$$\boxed{a := h \cdot g^{-1}} \qquad \textbf{Weingarten matrix} \tag{5.22}$$

Like curvature κ and torsion τ tell us how the normal changes along a space curve, the Weingarten matrix tells us how the normal changes along a surface:

$$\partial_i \vec{n} \quad = -\sum_j a_{ij} \partial_j \vec{f} \tag{5.23}$$

From the Weingarten matrix we now can compute the mean curvature H and the Gaussian curvature K for any given surface $\vec{f}$ (without proof):

$$\boxed{K = \det a = \tfrac{\det h}{\det g}} \tag{5.24}$$

$$\boxed{H = \tfrac{1}{2} \mathrm{tr}\, a} \tag{5.25}$$

In the following, we will use this recipe for some important examples.

Object	Topological equivalence	Euler characteristic $\chi = F - E + V$	Genus $G = \frac{2-\chi}{2}$
a Sphere	Cube 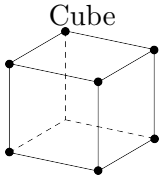	$\chi = 6 - 12 + 8 = 2$	$G = 0$
	Tetrahedron 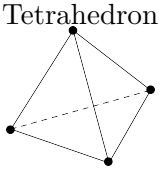	$\chi = 4 - 6 + 4 = 2$	$G = 0$
b n spheres	n cubes	$\chi = 2 \cdot n$	$G = 1 - n$
c Torus	punctured cube 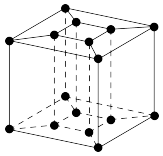	$\chi = 16 - 32 + 16 = 0$	$G = 1$
d Double torus	connected punctured cubes 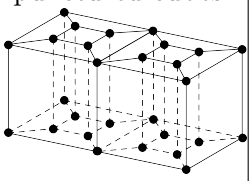	$\chi = -2$	$G = 2$

Table 5.2: **a** The sphere is topologically equivalent to a cube and a tetrahedron, respectively. χ can also be calculated from the Gauss-Bonnet theorem (equation 5.15): $\oint dA\, K = 4\pi R^2 \cdot \frac{1}{R^2} = 2\pi \cdot 2$. **b** The Euler characteristic is additive over multiple bodies. The more bodies, the larger χ and the more negative G. **c** The torus is topologically equivalent to toroidal polyhedra, e.g. a punctured cube. Note that $G = 1$, denoting that the object has one handle. **d** For topologically more complex structures, like the double or triple torus, it is more reasonable to determine the number of handles G and then calculate χ from equation 5.16 than to find a topologically equivalent polyhedron. Generally we find: The more handles, the larger G and the more negative χ.

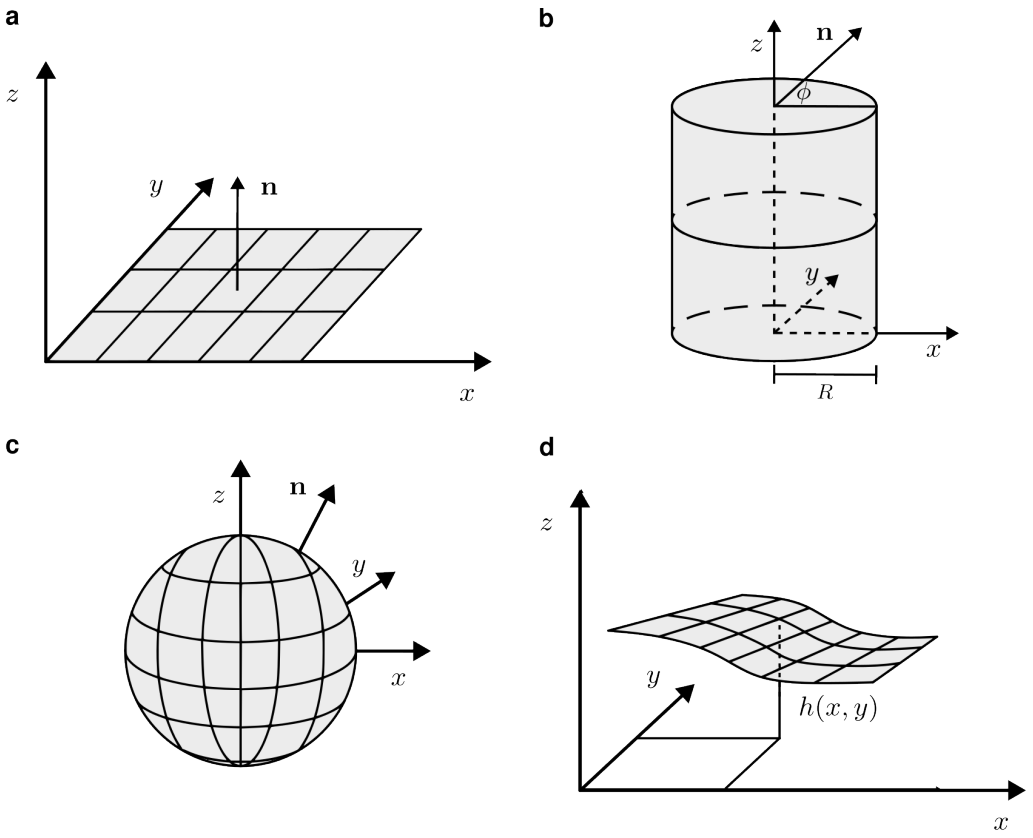

Figure 5.5: Parametrisation of different objects: **a** plane, **b** cylinder, **c** sphere, **d** monge parametrisation of a nearly flat surface.

1. **Plane** (figure 5.5a)

$$\vec{f} = \begin{pmatrix} x \\ y \\ 0 \end{pmatrix} \quad \Rightarrow \quad \partial_x \vec{f} = \begin{pmatrix} 1 \\ 0 \\ 0 \end{pmatrix}, \ \partial_y \vec{f} = \begin{pmatrix} 0 \\ 1 \\ 0 \end{pmatrix}, \ \vec{n} = \begin{pmatrix} 0 \\ 0 \\ 1 \end{pmatrix}$$

$$\Rightarrow g = \begin{pmatrix} 1 & 0 \\ 0 & 1 \end{pmatrix} \quad \Rightarrow \quad \det g = 1, \ dA = \sqrt{\det g}\, dxdy = dxdy$$

$$h = a = \begin{pmatrix} 0 & 0 \\ 0 & 0 \end{pmatrix} \quad \Rightarrow \quad H = K = 0$$

2. **Cylinder** (figure 5.5b, internal coordinates ϕ and z)

$$\vec{f} = \begin{pmatrix} R\cdot\cos\phi \\ R\cdot\sin\phi \\ z \end{pmatrix} \Rightarrow \partial_\phi \vec{f} = \begin{pmatrix} -R\cdot\sin\phi \\ R\cdot\cos\phi \\ 0 \end{pmatrix},\ \partial_z \vec{f} = \begin{pmatrix} 0 \\ 0 \\ 1 \end{pmatrix},\ \vec{n} = \begin{pmatrix} \cos\phi \\ \sin\phi \\ 0 \end{pmatrix}$$

$$\Rightarrow g = \begin{pmatrix} R^2 & 0 \\ 0 & 1 \end{pmatrix} \Rightarrow \det g = R^2,\ dA = R\,d\phi dz$$

$$h = \begin{pmatrix} -R & 0 \\ 0 & 0 \end{pmatrix} \qquad a = \begin{pmatrix} -\frac{1}{R} & 0 \\ 0 & 0 \end{pmatrix}$$

$$\Rightarrow H = -\frac{1}{2R},\ K = 0$$

3. **Sphere** (figure 5.5c, internal coordinates φ and θ)

$$\vec{f} = R\cdot\begin{pmatrix} \cos\theta\cdot\cos\varphi \\ \cos\theta\cdot\sin\varphi \\ \sin\theta \end{pmatrix} \Rightarrow \partial_\varphi \vec{f} = R\cdot\begin{pmatrix} -\cos\theta\cdot\sin\varphi \\ \cos\theta\cdot\cos\varphi \\ 0 \end{pmatrix},$$

$$\partial_\theta \vec{f} = R\cdot\begin{pmatrix} -\sin\theta\cdot\cos\varphi \\ -\sin\theta\cdot\sin\varphi \\ \cos\theta \end{pmatrix},$$

$$\vec{n} = \frac{1}{R}\cdot\vec{f}$$

$$\Rightarrow g = \begin{pmatrix} R^2\cdot\cos^2\theta & 0 \\ 0 & R^2 \end{pmatrix} \Rightarrow \det g = R^4\cdot\cos^2\theta,\ dA = R^2\cdot\cos\theta\,d\varphi d\theta$$

$$h = -\frac{1}{R}\cdot g \qquad a = -\frac{1}{R}\hat{\mathbb{I}}$$

$$\Rightarrow H = -\frac{1}{R},\ K = \frac{1}{R^2}$$

4. **Monge parametrization** (figure 5.5d). This parametrization is valid for surfaces without overhangs (such a surface is also called a *graph*). The surface is described by a height function $h(x,y)$. In the following we will assume the surface to be nearly flat, i.e. $\left|\vec{\nabla}h(x,y)\right| \ll 1$.

$$\vec{f} = \begin{pmatrix} x \\ y \\ h(x,y) \end{pmatrix} \Rightarrow \partial_x \vec{f} = \begin{pmatrix} 1 \\ 0 \\ \partial_x h \end{pmatrix},\ \partial_y \vec{f} = \begin{pmatrix} 0 \\ 1 \\ \partial_y h \end{pmatrix},$$

$$\vec{n} = \frac{1}{\sqrt{1+(\partial_x h)^2+(\partial_y h)^2}}\begin{pmatrix} \partial_x h \\ \partial_y h \\ 1 \end{pmatrix}$$

$$\Rightarrow g = \begin{pmatrix} 1+(\partial_x h)^2 & \partial_x h\cdot\partial_y h \\ \partial_x h\cdot\partial_y h & 1+(\partial_y h)^2 \end{pmatrix} \Rightarrow \det g \approx 1+(\partial_x h)^2+(\partial_y h)^2 = 1+(\vec{\nabla}h)^2$$

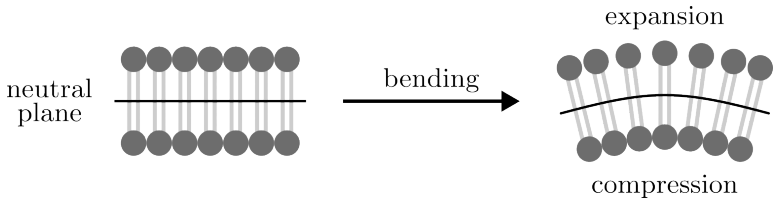

Figure 5.6: Sketch of a bent lipid double layer.

$$dA \approx \sqrt{1+(\vec{\nabla}h)^2}\,dxdy \approx [\underbrace{1}_{\substack{\text{reference}\\ \text{plane}}} \underbrace{+\frac{1}{2}(\vec{\nabla}h)^2}_{\text{excess area, }>0}]\,dxdy \tag{5.26}$$

$$h = \frac{1}{\sqrt{\det g}}\begin{pmatrix} \partial_{xx}h & \partial_{xy}h \\ \partial_{xy}h & \partial_{yy}h \end{pmatrix} \approx a$$

For calculating the Weingarten matrix, in lowest order we have $g \approx 1$ and thus $a \approx h$. Therefore the mean and Gaussian curvatures are

$$H \approx \frac{1}{2}(\partial_{xx}h + \partial_{yy}h) = \frac{1}{2}\Delta h \tag{5.27}$$

$$K \approx \partial_{xx}h \cdot \partial_{yy}h - (\partial_{xy}h)^2 \tag{5.28}$$

5.2 Curvature energy and minimal energy shapes

5.2.1 Bending Hamiltonian

What is the energy of a biomembrane? Because the membrane is fluid, it has no in-plane elastic energy (the shear modulus vanishes). As a fluid, it has in-plane compression, but the corresponding energy cost is so high due to the dense packing of the hydrocarbon chains, so that we can neglect this mode compared to others. Assuming mechanical equilibrium, the viscosity of the fluid membrane also does not count. As a fluid, the membrane has no physical coordinate system and thus its energy cannot depend on its parametrization. Thus the only relevant energy contribution we are left with is out-off-plane bending of the membrane. Hence, the Hamiltonian must be a function of the curvatures H and K

$$\mathcal{H} \;=\; \int dA\, f(H,K)$$

One can expand the Hamiltonian in small curvatures (or, in other words, in small $1/R$) up to order $1/R^2$ to obtain [17, 18, 19, 20]

$$\boxed{\mathcal{H} = \int dA\,\{\sigma + 2\kappa(H-c_0)^2 + \bar{\kappa}K\}} \qquad \textbf{Helfrich-Canham Hamiltonian}$$

Recall that $H \sim \mathcal{O}(1/R)$ and $K \sim \mathcal{O}(1/R^2)$. Higher order terms have also been investigated but lead to very complex structures.

The Helfrich-Canham Hamiltonian contains four material parameters:

1. σ denotes the surface tension. $\mathcal{H} = \sigma \int dA$ governs the physics of liquid droplets and soap bubbles. It can be interpreted as a chemical potential for the area. For liquid droplets and soap bubbles, surface area can be generated by simply changing film thickness. This is not possible for lipid bilayers, but there too reservoirs for surface area exist: first there is excess area stored in membrane fluctuations, and second lipids can flow into the area of interest. In cells, there are more biological reservoirs for area, like protein-mediated membrane invaginations called *caveolae* and vesicles close to the membrane that fuse on demand. The value of the surface tension of the water-air interface is very high (73 mN/m = 73 dyn/cm) because water is such a cohesive fluid. In our body, such a high surface tension can harm biomolecules and cells avoid to have direct contact to air; a notable exception are our lungs, where this cannot be avoided and special precautions have to be taken to prevent collapse. Usually cells are surrounded by aqueous medium and the surface tensions in the plasma membrane are much smaller (of the order of 300 pN/μm = 0.3 mN/m as measured by tether pulling, see below). The cortical tension of human cells is around 2 mN/m, but this should not be confused with the membrane tension, the lipid bilayer would rupture at that value, so it has to be protected from such high values (cortex and plasma membrane are connected by linkers which couple them).

2. κ denotes the bending rigidity. $\mathcal{H} = 2\kappa \int dA\, H^2$ is the bending Hamiltonian which governs the physics of vesicles. As a typical value one finds $\kappa = 20\, k_B T$, both for vesicles and cells. κ is a classical elastic modulus that also emerges in elasticity theory of thin plates.

3. c_0 reflects any asymmetry of the bilayer, hence denoting the spontaneous (mean) curvature of the membrane. Asymmetries can be caused for instance by embedded or adsorbed proteins or different lipid composition of the two opposing layers of the bilayer, to name but a few.

4. $\bar{\kappa}$ is called the saddle-splay modulus and is related to the topology by the Gauss-Bonnet theorem (equation 5.15). $\bar{\kappa}$ denotes a chemical potential for the number of objects and hence describes the membrane's tendency to merge or split.

If we consider $\sigma = 0$ and $c_0 = 0$, then :

$$\begin{aligned}
\mathcal{H} &= \int dA\, \{2\kappa H^2 + \overline{\kappa} K\} \\
&= \int dA\, \{2\kappa (\frac{\kappa_1 + \kappa_2}{2})^2 + \overline{\kappa} \cdot \kappa_1 \kappa_2\} \\
&= \int dA\, \{\frac{\kappa_+}{2}(\kappa_1 + \kappa_2)^2 + \frac{\kappa_-}{2}(\kappa_1 - \kappa_2)^2\}
\end{aligned}$$

with $\kappa_+ = \kappa + \frac{\overline{\kappa}}{2}$ and $\kappa_- = -\frac{\overline{\kappa}}{2}$. This indicates two topological instabilities:

- $\kappa_+ < 0 \Longrightarrow \kappa_1 = \kappa_2 \longrightarrow \infty$, describes a system of many small droplets.

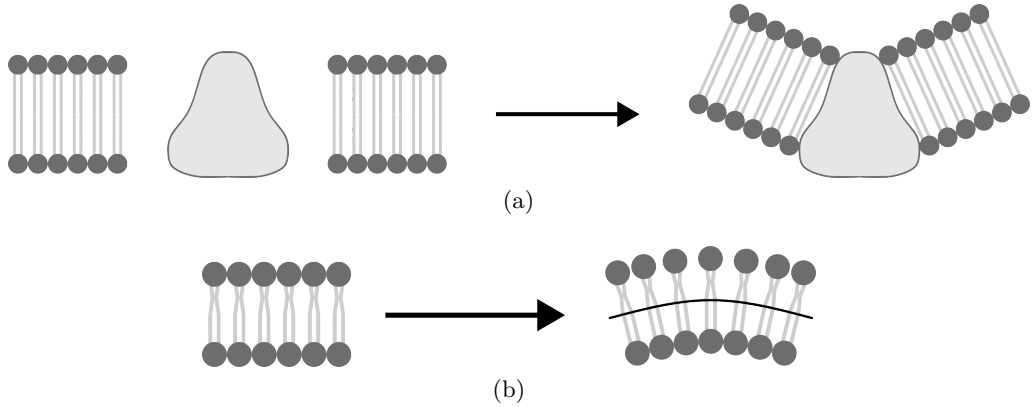

Figure 5.7: Spontaneous curvature of the membrane due to asymmetries caused by (a) embedded proteins (adsorbed proteins would have similar effect) and by (b) different lipid compositions in outer versus inner leaflet.

- $\kappa_- < 0 \Longrightarrow \kappa_1 = -\kappa_2 \longrightarrow \infty$, describes a saddle-like surface with very small lattice constant (e.g sponge or egg-carton).

This is why stability requires κ_+ and κ_- both to be larger than zero. This implies $-2\kappa < \overline{\kappa} < 0$, so $\overline{\kappa}$ is expected to be small and negative.

One can use the elasticity theory for linear isotropic material to derive the two elastic moduli of the thin membrane as a function of the two elastic moduli of the bulk material:

$$\kappa = \frac{Ed^3}{12(1-\nu)^2},\ \overline{\kappa} = \frac{-Ed^3}{6(1+\nu)} \tag{5.29}$$

where E is the Young's modulus of the material and ν its Poisson's ratio. The bulk material relevant here is the hydrocarbon fraction of the bilayer. $d = 4nm$ is its thickness. With the value $\nu = 0.5$ for incompressible material, a bending rigidity κ of 20 k_BT is achieved for a Young's modulus around $E = 10$ MPa, which is a very reasonable value. For the saddle splay modulus we have $\overline{\kappa}/\kappa = -1/3$, which lies in the range between -2 and 0 discussed above.

The bending Hamiltonian is an *energy functional* — it is a scalar that depends on a function, e.g. in Monge representation $\mathcal{H} = \mathcal{H}[h(x, y)]$. We now have to deal with two important issues that complement each other:

- **Energetics** deals with the question what is the surface with minimal energy. These surfaces have to solve the Euler-Lagrange equations, also called shape equations $\frac{\delta\mathcal{H}}{\delta h} = 0$. Here $\frac{\delta}{\delta h}$ is a *functional derivative.*
- **Statistics** answers the question what is the effect of thermal fluctuations on membranes. Here the starting point is the partition sum $Z = \int \mathcal{D}h \exp(-\beta\mathcal{H}[h])$, which is a *path integral* or *functional integral* (integral over all possible functions).

Together the minimal energy state and the fluctuations around it describe the main features of interest.

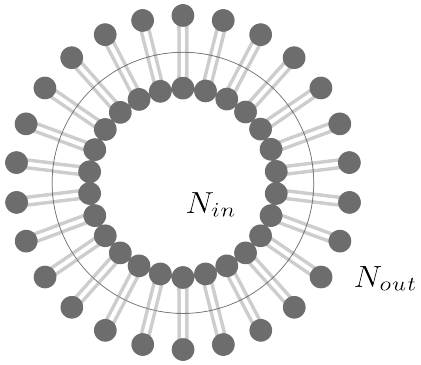

Figure 5.8: Schematics of a lipid vesicle with constant surface A and volume V. Although lipid bilayers are permeable to water, there are always some ions caged in the vesicle, fixing an osmotic pressure, which keeps the volume constant. Also the number of lipids on the outside N_{out} and inside N_{in} is constant, because of the energy barrier that does not allow for the lipids to jump from one side of the membrane to the other or to escape.

5.2.2 Minimal energy shapes for vesicles

In this section we are looking at closed surfaces; therefore $\overline{\kappa}$ is irrelevant due to the Gauss-Bonnet theorem. Also $c_0 = 0$ because we assume symmetric membranes. We add a term $-pV$ to control the volume. In practice, one prepares a suspension of vesicles, e.g. by ultrasound or electroporation acting on a lipid-water mixture, and then selects vesicles of interest, e.g. with optical tweezers or a micropipette. Each vesicle then has fixed values for area and volume which can be measured with e.g. video or fluorescence microscopy. Using $A = 4\pi R_0^2$, one can define the radius of the equivalent sphere. Then the only relevant parameter of the system is the reduced volume v:

$$v = \frac{V}{\frac{4\pi}{3} R_0^3}$$

Each vesicle class has an individual value for v, and $v \leq 1$ should be always fulfilled; $v < 1$ describes a deflated vesicle with excess area for non-trivial shapes. Shape with $v = 1$ is a sphere and has the optimal $\frac{A}{V}$ ratio. Note that

$$\mathcal{H} = 2\kappa \int dA\, H^2 \underbrace{=}_{\text{for sphere}} 2\kappa\, 4\pi R^2 \cdot \frac{1}{R^2} = 8\pi\kappa = const.$$

which indicates that the solutions are independent of rescaling (this is part of a more general property called *conformal invariance*).

In order to obtain a phase diagram as a function of v, we have to solve the corresponding Euler-Lagrange equations (*shape equations*). These are derived by varying the surface in normal direction

$$\vec{f}(x, y) = \vec{f}_0(x, y) + \epsilon\phi(x, y)\vec{n}(x, y) \tag{5.30}$$

and then asking for the first ϵ-derivative of the energy functional to vanish for arbitrary $\phi(x, y)$ (one can show that a tangential variation does not matter in

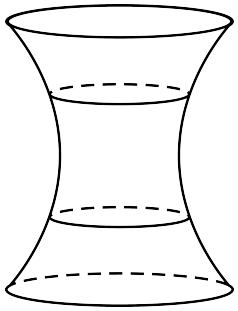

Figure 5.9: Catenoid as an example of a minimal surface, which is not compact and has $H = 0$.

this order). The result can be written as [21]

$$\boxed{p + 2\sigma H - 2\kappa(2H\,(H^2 - K) - \Delta H) = 0} \quad \text{Euler-Lagrange equation} \tag{5.31}$$

where Δ is the Laplace-Beltrami operator (only for the almost flat membrane we get the Laplace operator $\Delta = \partial_x^2 + \partial_y^2$). The Euler-Lagrange equation is a partial differential equation (PDE) of the 4^{th} order with a famous limit for $\kappa = 0$, namely the Laplace law for soap bubbles

$$\boxed{H = -\tfrac{p}{2\sigma}} \quad \text{Laplace law for soap bubbles} \tag{5.32}$$

Here a simple derivation of the Laplace law

$$\begin{aligned} \sigma\, dA &= -p\, dV \\ \sigma\, d(4\pi R^2) &= -p\, d\left(\frac{4\pi}{3} R^3\right) \\ \sigma\, 4\pi\, 2R\, dR &= -p\, \frac{4\pi}{3}\, 3R^2\, dR \\ \Rightarrow \frac{1}{R} &= -\frac{p}{2\sigma} \end{aligned} \tag{5.33}$$

As the only compact surface with constant mean curvature (CMC-surface) is the sphere, a soap bubble is spherical. CMC-surfaces are critical points of the area functional under the constraint of a constant volume.

For $p = 0$ the shape equation is simply $\boxed{H = 0}$, which describes a minimal surface, i.e. a surface under tension with minimal energy given a particular boundary curve. Those surfaces are always saddle-like, because $H = 0$ means $R_1 = -R_2 \Rightarrow K = -\frac{1}{R_1^2}$, which is always negative. The implication is that those surfaces cannot be compact, because a surface that is saddle-shaped cannot be enclosed by a boundary. A well-known example for a minimal surface is the catenoid connecting two wireframes, compare figure 5.9.

The solutions to the Euler-Lagrange equation for $\sigma = 0$ and finite κ are called *Wilmore surfaces*. Because they are solutions to $\mathcal{H} = 2\kappa \int dA\, H^2$, minimal surfaces with $H = 0$ are included. But due to their saddle-like shape, minimal

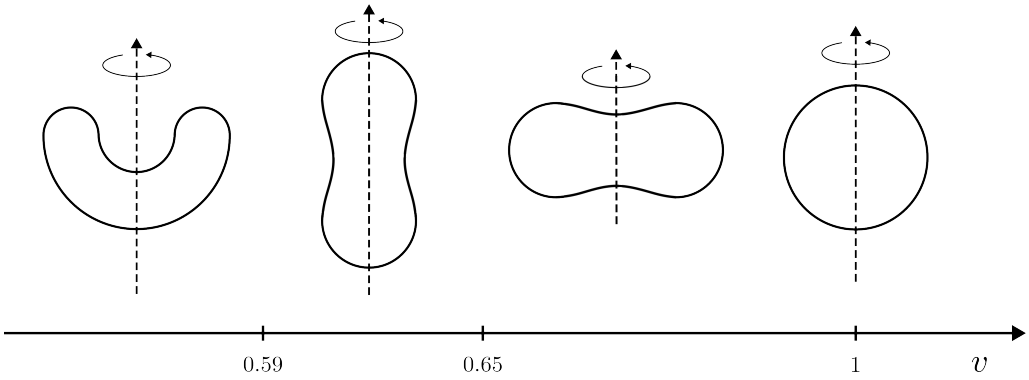

Figure 5.10: The shape diagram represents the minimal energy shapes for given points in the phase space. Starting at small v we observe stomatocyte, oblate, prolate and sphere at $v = 1$. There are two bifurcation points at 0.059 and 0.65. Oblate resembles RBC, but exists only over a small range of v.

surfaces without edges cannot be compact, so we are interested in Wilmore surfaces with $H \neq 0$ as solutions for the vesicle shape problem. Note that these solutions will not be CMC-surfaces, which arise from another energy function.

The main methods to solve the shape equations for the vesicles are solution of the shape equations for axisymmetric shapes (4th order ODE), solutions for the shape equations with FEM-methods for arbitrary shapes (4th order PDE) or minimization for triangulated surfaces (e.g. with the software *Surface Evolver* from Ken Brakke). Each of these methods gives the one-dimensional shape diagram shown in figure 5.10 [22]. One clearly sees a sequence of symmetry breaks as the reduced volume goes down (in terms of the differential equations, we are dealing with bifurcations; this is in analogy to phase transitions in thermodynamics). The obtained shapes describe many of the observed vesicle and cell shapes, e.g. the biconcave vesicle looks like a red blood cell (discocyte). The problem of this theory is that it does not describe all the shapes seen in nature, e.g. budding vesicles. This means that we are close to the right solution, but the model has to be expanded and more features of the real system have to be added.

A more complete theory is given by the Area Difference Elasticity model (ADE model) [23], which has two parameters. In addition to the reduced volume, we now also consider the possibility that the number of lipids may be different in the outside and the inside monolayers of the lipid bilayer. Until now we assumed an infinitely thin membrane, but now we no longer disregard its thickness. We define an area difference $\Delta A_0 = a(N_{in} - N_{out})$, where N_{in} is the number of lipids on the inner side of the vesicle, N_{out} is the number on the outside, and a, which is the typical area per lipid, has the dimensions of nm^2. Since A_{in} and A_{out} do not change, for energy reasons, ΔA_0 stays constant for a vesicle. The bending Hamiltonian for the ADE model is

$$\mathcal{H} = 2\kappa \int dA\, H^2 + \frac{\alpha}{2}(\Delta A - \Delta A_0)^2$$

The differential geometry result for the integrated mean curvature is $\Delta A = 2d \int dA\, H$, with d being the thickness of the membrane. The resulting shape

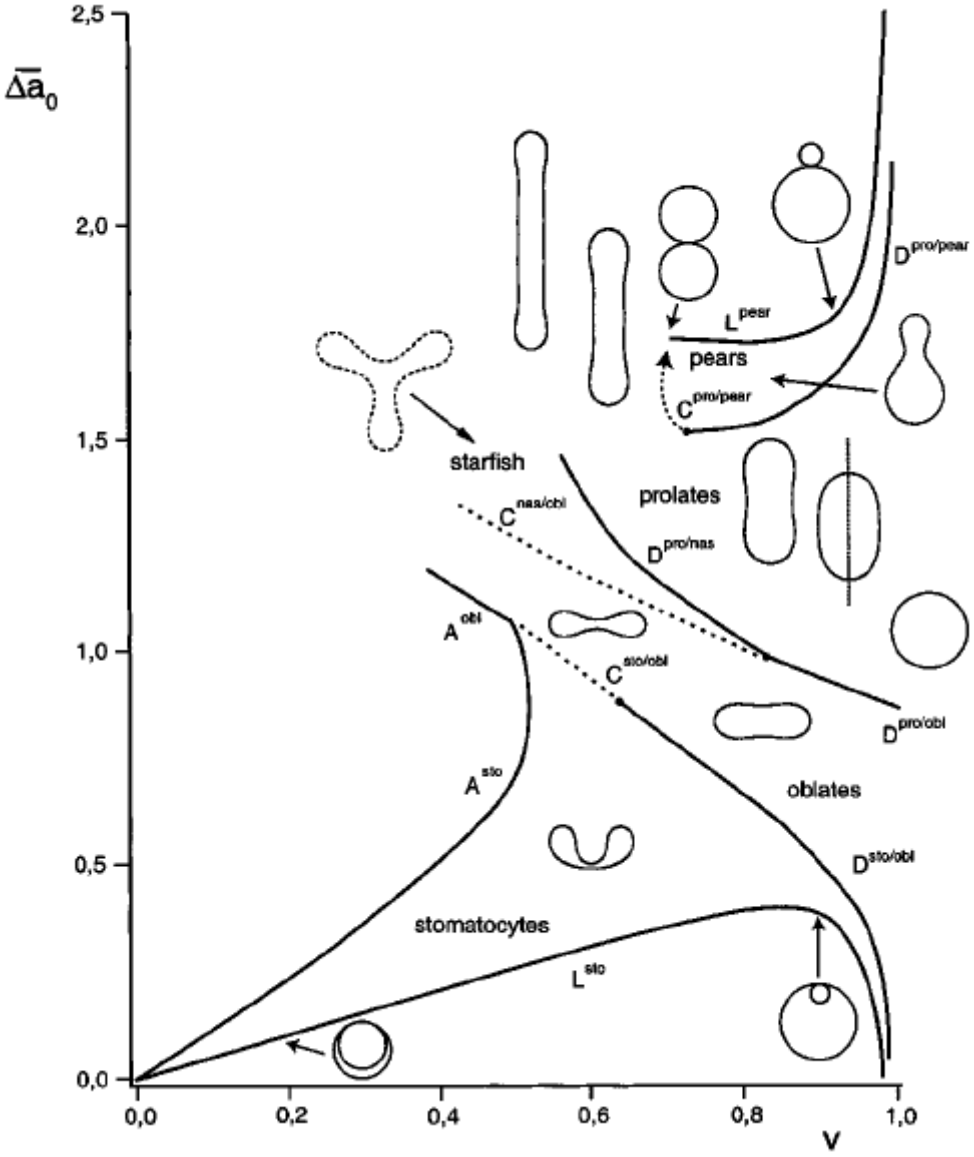

Figure 5.11: Two dimensional shape diagram from ADE model. For each region, minimal energy shapes are indicated. The horizontal axis is the reduced volume v; spheres again correspond to $v = 1$. The vertical axis shows the effective differential area between inside and outside monolayers.

diagram is now two-dimensional as shown in Fig. 5.11. It now contains the budded shape as well as non-axisymmetric shapes like the starfish vesicle. In the literature, many similar models have been discussed, including the spontaneous curvature and the bilayer-couple models, to explain the zoo of vesicle shapes, but the ADE-model seems to be the most appropriate one. Therefore it is also used as the standard starting point to explain the shape of red blood cells, which are known to have very asymmetric membrane leaflets.

5.2.3 Tether pulling

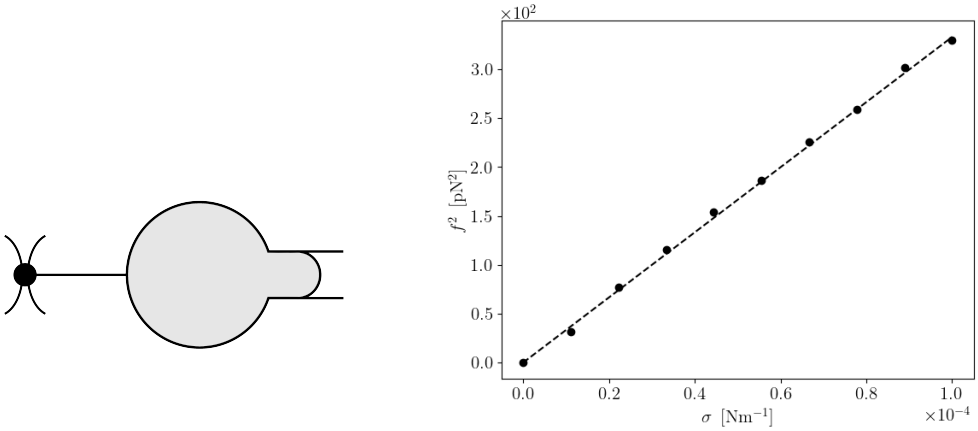

(a) (b)

Figure 5.12: The force to pull a tether out of a vesicle scales with the square root of the tension [24].

We briefly discuss a first case of minimal energy shapes, namely if a tether is pulled out of a vesicle or cell, which is a standard setup to measure membrane tension [24]. Experimentally one first sucks a vesicle into a micropipette with underpressure and thus sets the tension in the membrane. Then one grabs an adhesive bead with an optical tweezer and moves it onto the membrane. If adhesion is successful, a cylindrical tether is pulled out of the membrane upon retraction. The corresponding force can be measured from the displacement of the bead away from the focus of the laser bead. Experimentally it was found that after overcoming an initial barrier, this force will be constant; in contrast to an elastic situation, when force should rise with distance, this indicates that membrane is flowing into the tether. Only when a very large tether is pulled, the reservoir will be depleted and force goes up.

We write the Helfrich-Hamiltonian for a cylinder with tension and bending rigidity and add a term for the pulling:

$$E = 2\pi RL\left[\frac{\kappa}{2R^2} + \sigma\right] - FL \tag{5.34}$$

where L is the length of the cylinder and F the pulling force. We minimize for

R to get:

$$R = \sqrt{\frac{\kappa}{2\sigma}} \tag{5.35}$$

At equilibrium, membrane energy and pulling energy should balance and thus

$$F = 2\pi\sqrt{2\kappa\sigma} \tag{5.36}$$

Therefore the force F scales as the square root of σ, as has been shown experimentally, compare Fig. 5.12. Thus the force can now be used to measure σ.

5.2.4 Particle uptake

Cells continuously take up small particles or viruses with sizes of the order of $10 - 300\,\mathrm{nm}$ (endocytosis). Essentially these particles are wrapped by the membrane due to some gain of adhesion energy. In addition, a clathrin coat is usually assembled on the intracellular side, which provides an additional driving force for wrapping. This principle is universal and used by different organelles (endosome, Golgi apparatus, endoplasmatic recticulum), although the polymer coats are different (e.g. COPI and II). Particle uptake and vesicle budding require that the energetic gain of particle adhesion and coat polymerisation overcomes the energetic cost of membrane deformations.

We first aim for a simple phase diagram of particle uptake [25, 26]. For simplicity, for the moment being we neglect the contribution from the free membrane and approximate the growing coat region as sphercial cap. In general, for a particle to be taken up, it has to be adhesive and the adhesion energy has to balance the bending energy. The Helfrich Hamiltonian reads

$$\mathcal{H} = \int dA(2\kappa H^2 + \sigma) - wA_{ad} \tag{5.37}$$

where A_{ad} is the adherent membrane area and w the adhesion energy area density. A typical value would be $w = 0.1\ \mathrm{mJ/m^2}$.

We next consider a sphere of radius R. If we denote the angle α to describe where the contact line between membrane and sphere is located (compare figure 5.13), then the wrapping variable $z = 1 - \cos\alpha$ will run from 0 to 2 as the membrane wraps the particle. If we neglect the contributions from the bending of the free membrane, we get

$$E = 4\pi z\kappa + \pi R^2 z^2 \sigma - 2\pi R^2 z w \tag{5.38}$$

The first term is the bending energy, which is independent of radius. The second and last term are the surface tension and adhesion energy terms, respectively. While both have the same R^2-scaling, they have different scaling with z. The last term has the trivial z-scaling. The second term however scales as z^2, because here the excess area $A_{excess} = A_{ad} - A_{projected}$ matters:

$$A_{excess} = 2\pi R^2(1 - \cos\alpha) - \pi R^2 \sin^2\alpha = \pi R^2(1 - 2\cos\alpha + \cos^2\alpha) = \pi R^2 z^2 \tag{5.39}$$

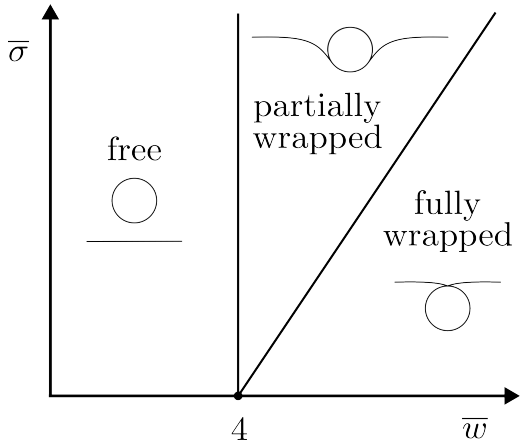

Figure 5.13: Phase diagram of particle wrapping by membranes as function of surface tension σ and adhesion energy w.

We now non-dimensionalize the energy and get

$$\bar{E} = \frac{E}{\pi\kappa} = 4z + \bar{\sigma}z^2 - \bar{w}z = -(\bar{w} - 4)z + \bar{\sigma}z^2 \tag{5.40}$$

where $\bar{\sigma} = \sigma R^2/\kappa$ and $\bar{w} = 2wR^2/\kappa$. This energy function gives rise to a phase diagram as shown in figure 5.13. For $\bar{w} < 4$, the energy is always positive and no wrapping can occur. This corresponds to the free state. Note that $\bar{w} = 4$ translates into a minimal radius $R = \sqrt{2\kappa/w} \approx 20$ nm, below which uptake is not possible. For $\bar{w} > 4 + 4\bar{\sigma}$, the minimal energy is found for $z = 2$, the fully wrapped state. In between there is a parameter region where the minimum lies at a finite value of z, here the partially wrapped state is stable.

5.2.5 Free membrane around particle

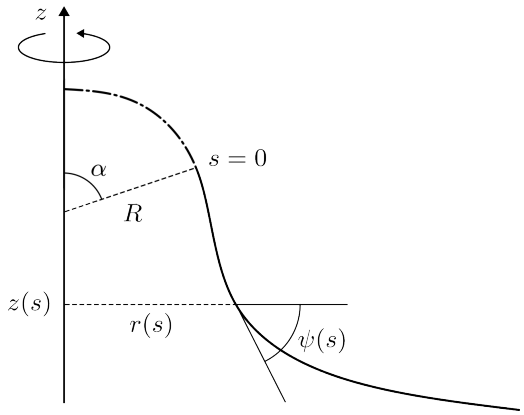

Figure 5.14: Parametrisation of the free membrane around a spherical particle. The slightly dashed curve represents the part of the membrane that adheres to the particle and/or is covered by the coat; the solid line is the free part of the membrane, which becomes horizontal at infinity.

Until now we have neglected the shape of the free membrane surrounding the contact area, where the membrane has the shape of the spherical particle that is taken up. We now minimize the Helfrich Hamiltonian for the shape of the free membrane using the calculus of variation [27, 28]. Because the situation is axisymmetric, we parametrize membrane shape by cylindrical coordinates $r(s)$ and $z(s)$, where s is the arc length along the shape contour of the membrane and ϕ is the polar angle

$$\vec{r} = \begin{pmatrix} r(s)\cos\phi \\ r(s)\sin\phi \\ z(s) \end{pmatrix} . \tag{5.41}$$

Importantly, we can express $r(s)$ and $z(s)$ by means of the the tangential angle $\psi(s)$ as

$$\dot{r} = \cos\psi(s) \qquad \dot{z} = -\sin\psi(s) \tag{5.42}$$

Our aim is to calculate the principal curvatures κ_1 and κ_2. Hence, we calculate the metric g, the normal vector $\vec{n}$, the second fundamental form h and the Weingarten matrix a. We find

$$g = \begin{pmatrix} 1 & 0 \\ 0 & r^2 \end{pmatrix} \tag{5.43}$$

$$\vec{n} = \begin{pmatrix} \cos\phi\sin\psi \\ \sin\phi\sin\psi \\ \cos\psi \end{pmatrix} \tag{5.44}$$

$$h = \begin{pmatrix} -\dot{\psi} & 0 \\ 0 & -r\sin\psi \end{pmatrix} \tag{5.45}$$

$$a = \begin{pmatrix} -\dot{\psi} & 0 \\ 0 & -\sin\psi/r \end{pmatrix} \tag{5.46}$$

Thus, the principal curvatures are given by the eigenvalues of a, $\kappa_1 = -\dot{\psi}$ and $\kappa_2 = -\sin\psi/r$. Then the Helfrich Hamiltonian reads with the mean curvature $2H = \kappa_1 + \kappa_2$

$$\mathcal{H} = \int \mathrm{d}s\mathrm{d}\phi \left\{ \sigma + \frac{\kappa}{2}\left(\dot{\psi} + \sin\frac{\psi}{r}\right)^2 \right\} r\,. \tag{5.47}$$

In order to minimise $\mathcal{H}$ with respect to $r(s)$ and $\psi(s)$ we have to include an additional Lagrange multiplier $\gamma(s)$ to incorporate Eq. (5.42). We note that because of the spherical geometry we do not need a second Lagrange multiplier, as variations of the contour endpoints are independent. We define an action

$$\mathcal{S}[r(s),\psi(s)] = \frac{\mathcal{H}}{2\pi\kappa} + \int \mathrm{d}s\gamma(s)(\dot{r} - \cos\psi) = \int \mathrm{d}s\mathcal{L}(\psi,\dot{\psi},r,\dot{r})\,, \tag{5.48}$$

with a Lagrange function $\mathcal{L}$

$$\mathcal{L}(\psi,\dot{\psi},r,\dot{r}) = \frac{1}{2}\left(\dot{\psi} + \frac{\sin\psi}{r}\right)^2 r + \frac{r}{\lambda^2} + \gamma(\dot{r} - \cos\psi)\,, \tag{5.49}$$

where $\lambda = \sqrt{\kappa/\sigma}$ defines the characteristic length scale of the membrane. The Euler-Lagrange equations are the solutions to the variational problem

$$\delta\mathcal{S} = 0 \leftrightarrow \frac{\mathrm{d}}{\mathrm{d}s}\frac{\partial\mathcal{L}}{\partial\dot{q}_k} - \frac{\partial\mathcal{L}}{\partial q_k} = 0\,, \tag{5.50}$$

where $q_k = \{r, \psi\}$. Thus,

$$\begin{aligned}\ddot{\psi} &= -\frac{\dot{\psi}\cos\psi}{r} + \frac{\cos\psi\sin\psi}{r^2} + \frac{\gamma\sin\psi}{r}\\ \dot{\gamma} &= \frac{1}{2}\dot{\psi}^2 - \frac{\sin^2\psi}{2r^2} + \frac{1}{\lambda^2}\,.\end{aligned} \tag{5.51}$$

In the usual case, the contour length is variable. Because $\mathcal{L}$ does not explicitly depend on s, $F = \dot{r}\partial_{\dot{r}}\mathcal{L} + \dot{\psi}\partial_{\dot{\psi}}\mathcal{L} - \mathcal{L}$ is conserved. Since a variation of $\mathcal{S}$ with respect to the contour lengths at the two end points has to vanish, one obtains that F has to vanish at the end points. Hence

$$F = \frac{r\dot{\psi}^2}{2} - \frac{r}{2}\left(\frac{\sin\psi}{r}\right)^2 - \frac{r}{\lambda^2} + \gamma\cos\psi = 0\,. \tag{5.52}$$

Using Eq. (5.52) we can eliminate γ from Eq. (5.51) to get the shape equation for axial symmetry

$$\ddot{\psi}\cos\psi + \frac{\dot{\psi}\cos^2\psi}{r} + \frac{\dot{\psi}^2\sin\psi}{2} - \frac{\sin\psi}{2r^2}\left(2\cos^2\psi + \sin^2\psi\right) - \frac{1}{\lambda^2}\sin\psi = 0\,. \tag{5.53}$$

Eq. (5.53) together with Eq. (5.42) and the boundary conditions

$$r(0) = R\sin\alpha\,, \psi(0) = \alpha\,, \psi(\infty) = 0\,, \dot{\psi}(\infty) = 0\,, z(\infty) = 0\,, \tag{5.54}$$

then fully describe the membrane's shape.

In general the shape equations, as a set of ODEs, can be solved numerically, for example by means of the shooting method. The membrane parameter λ sets the typical extension of the membrane deformation (cf. Fig. 5.15). Note that for typical parameter values of κ and σ we get $\lambda = 10 - 100\,\mathrm{nm}$. Depending on the λ and the particle or coat radius R one can define three membrane regimes.

- For a tense membrane ($\lambda/R \ll 1$) the deformation is concentrated in a very narrow and highly curved region near the particle or coat.
- For an intermediate membrane ($\lambda/R \approx 1$) the deformation propagates some intermediate distance into the membrane
- For a loose membrane($\lambda/R \gg 1$) the deformation propagates far from the particle or coat into the membrane.

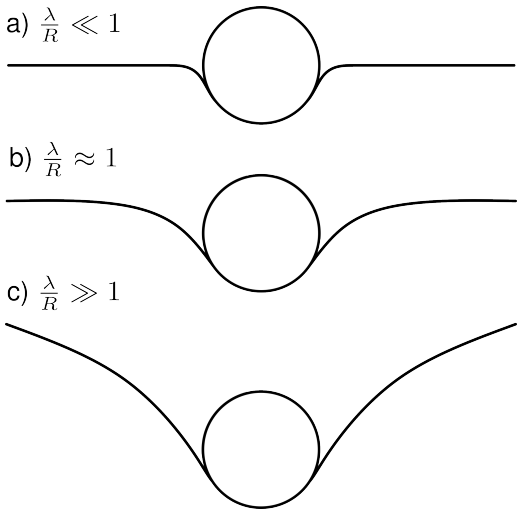

Figure 5.15: Membrane shapes for different regimes according to λ/R. a) $\lambda/R \ll 1$ represent tense membrane, b) $\lambda/R \approx 1$ represents intermediate membrane and $\lambda/R \gg 1$ represents loose membrane.

5.3 Membrane fluctuations

5.3.1 Thermal roughening of a flat membrane

In this section we will investigate the mean square deviation $< h^2 >$ of a flat lipid membrane fluctuating at temperature T, see figure 5.16. Its square root is a measure for the size of typical excursions. In lowest order, the energy functional for the almost flat membrane is (compare equations 5.26 and 5.27)

$$\mathcal{H}\left[h(x,y)\right] = 2\kappa \int dA\, H^2 = \frac{\kappa}{2} \int dxdy (\Delta h(x,y))^2$$

Calculating this correlation function is a standard problem in statistical field theory and we solve it using Fourier transforms. Because we have $d = 2$ for membranes, we now use vector notation:

$$h(\vec{x}) = \frac{1}{(2\pi)^{d/2}} \int d\vec{k}\, h(\vec{k})\, \exp(i\vec{k}\cdot\vec{x}) \tag{5.55}$$

$$h(\vec{k}) = \frac{1}{(2\pi)^{d/2}} \int d\vec{x}\, h(\vec{x})\, \exp(-i\vec{k}\cdot\vec{x}) \tag{5.56}$$

$$\delta(\vec{k}) = \frac{1}{(2\pi)^{d}} \int_{-\infty}^{\infty} d\vec{x}\, \exp(i\vec{k}\cdot\vec{x}) \tag{5.57}$$

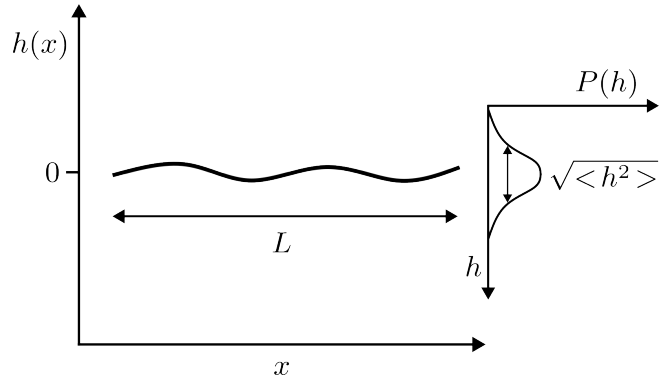

Figure 5.16: Fluctuating membrane of lateral length L and typical deviation from a flat membrane $\sqrt{< h^2 >}$

$h(\vec{x})$ has to be real

$$\begin{aligned} h(\vec{x}) &= \frac{1}{(2\pi)^{d/2}} \int d\vec{k}\, h(\vec{k})\, \exp(i\vec{k}\cdot\vec{x}) \\ &= h(\vec{x})^* = \frac{1}{(2\pi)^{d/2}} \int d\vec{k}\, h(\vec{k})^*\, \exp(-i\vec{k}\cdot\vec{x}) \\ \Rightarrow\ & h(\vec{k}) = h(-\vec{k})^* \end{aligned}$$

Now we write $h(\vec{k})$ in real and imaginary part

$$\begin{aligned} h(\vec{k}) &= a(\vec{k}) + i\, b(\vec{k}) \\ \Rightarrow a(\vec{k}) &= a(-\vec{k}) \\ b(\vec{k}) &= -b(-\vec{k}) \end{aligned}$$

The Hamiltonian can be calculated as

$$\begin{aligned} \mathcal{H} &= \frac{\kappa}{2(2\pi)^d} \int d\vec{x} \left(\int d\vec{k}\, (ik)^2 h(\vec{k}) \exp(i\vec{k}\cdot\vec{x}) \right) \left(\int d\vec{k'}\, (ik')^2 h(\vec{k'}) \exp(i\vec{k'}\cdot\vec{x}) \right) \\ &= \frac{\kappa}{2} \int d\vec{k} \int d\vec{k'}\, k^2 k'^2 \delta(\vec{k}+\vec{k'}) h(\vec{k}) h(\vec{k'}) \\ &= \frac{\kappa}{2} \int d\vec{k}\, k^4 h(\vec{k}) h(-\vec{k}) \\ &= \frac{\kappa}{2} \int d\vec{k}\, k^4 h(\vec{k}) h(\vec{k})^* \end{aligned}$$

$$\boxed{\mathcal{H}[h(\vec{k})] = \kappa \textstyle\int_{k>0} d\vec{k}\, k^4 [a^2(\vec{k}) + b^2(\vec{k})]} \tag{5.58}$$

The result is the same for $k > 0$ and for $k < 0$ and the case $k = 0$ is irrelevant, because $a(\vec{k}) = a(-\vec{k})$ and $b(\vec{k}) = b(-\vec{k})$. Therefore we restrict the integration to positive k, which gives a factor of 2. The bending energy is the sum of the squares of the decoupled amplitudes. The k^4-dependency is typical for bending.

The partition sum is a functional integral over all possible membrane conformations

$$\begin{aligned} Z &= \int \mathcal{D}h \, \exp(-\beta \mathcal{H}[h(x)]) \\ &= \prod_{k>0} \int_{-\infty}^{\infty} da(\vec{k}) \int_{-\infty}^{\infty} db(\vec{k}) \, \exp(-\beta\kappa k^4 [a(\vec{k})^2 + b(\vec{k})^2]) \\ &= \prod_{k>0} \frac{k_B T}{\kappa k^4} \end{aligned}$$

because this is simply a product of many Gauss integrals. For the free energy per unit area, we therefore get

$$\frac{F}{A} = -k_B T \ln Z = k_B T \int_{k>0} d\vec{k} \ln \frac{\kappa k^4}{k_B T} \tag{5.59}$$

However, here we are interested in the correlation functions, not in Z or F directly. For each $\vec{k}$, there are two independent and harmonic degrees of freedom. We therefore have

$$\begin{aligned} < a^2(\vec{k}) > \quad &= \quad \frac{k_B T}{2\kappa k^4} \\ < b^2(\vec{k}) > \quad &= \quad \frac{k_B T}{2\kappa k^4} \\ < a(\vec{k}) a(\vec{k}') > \quad &= \quad < a(\vec{k}) >< a(\vec{k}') >= 0 \qquad \text{etc.} \\ &\quad \vec{k} \neq \vec{k}', \vec{k} \neq -\vec{k}' \end{aligned}$$

which is an example of the equipartition theorem for harmonic systems. For h this means

$$\begin{aligned} < h(\vec{k}) h(\vec{k}') > &= < \Big(a(\vec{k}) + ib(\vec{k})\Big) \Big(a(\vec{k}') + ib(\vec{k}')\Big) > \\ &= < a(\vec{k}) a(\vec{k}') > + i < a(\vec{k}) b(\vec{k}') > + i < b(\vec{k}) a(\vec{k}') > - < b(\vec{k}) b(\vec{k}') > \\ &= < a(\vec{k}) a(\vec{k}') > - < b(\vec{k}) b(\vec{k}') > \\ &= \begin{cases} 0 - 0 = 0 & \vec{k}' \neq \vec{k}, \vec{k}' \neq -\vec{k} \\ < a^2(\vec{k}) > - < b^2(\vec{k}) >= 0 & \vec{k}' = \vec{k} \\ < a^2(\vec{k}) > + < b^2(\vec{k}) >= \frac{k_B T}{\kappa k^4} & \vec{k}' = -\vec{k} \end{cases} \end{aligned} \tag{5.60}$$

where in the last line we have used $b(-\vec{k}) = -b(\vec{k})$. We now get in Fourier space:

$$\boxed{< h(\vec{k}) h(\vec{k}') >= \frac{k_B T}{\kappa k^4} \delta(\vec{k} + \vec{k}')} \tag{5.61}$$

For the backtransform to real space, we get

$$\begin{aligned} < h^2(\vec{x}) > &= < \left(\frac{1}{(2\pi)^{d/2}} \int d\vec{k} \, h(\vec{k}) \exp(i\vec{k}\vec{x}) \right) \left(\frac{1}{(2\pi)^{d/2}} \int d\vec{k}' \, h(\vec{k}') \exp(i\vec{k}'\vec{x}) \right) > \\ &= \frac{1}{(2\pi)^d} \int d\vec{k} \int d\vec{k}' \exp(i(\vec{k} + \vec{k}')\vec{x}) \frac{k_B T}{\kappa k^4} \delta(\vec{k} + \vec{k}') \end{aligned}$$

Now the space-dependence drops out due to the delta function (the underlying reason is translational invariance) and we are left with one integral only. If we define a as the microscopic cutoff (molecular size) and L as macroscopic cutoff (system size) and use $d = 2$, we get in polar coordinates:

$$\begin{aligned} < h^2(x,y) > &= \frac{2\pi}{(2\pi)^2} \int_{\frac{2\pi}{L}}^{\frac{2\pi}{a}} k\, dk\, \frac{k_B T}{\kappa k^4} \\ &= \frac{2\pi}{(2\pi)^2} \frac{1}{2} \frac{k_B T}{\kappa} \left[\left(\frac{L}{2\pi} \right)^2 - \left(\frac{a}{2\pi} \right)^2 \right] \\ &= \boxed{\frac{k_B T}{16\pi^3 \kappa} L^2 =< h^2 >} \end{aligned} \tag{5.62}$$

Equation 5.62 shows that the mean square deviation is proportional to temperature T, inversely proportional to bending rigidity κ, and increases quadratically with the system size L. Note that the limit $a \longrightarrow 0$ is unproblematic.

In order to better understand the fluctuations of membranes we can put in numbers:

$$\kappa = 20 k_B T$$

$$\begin{aligned} L &= 10\,\text{nm} \Rightarrow \sqrt{< h^2 >} = 1\,\text{Å} \\ L &= 1\,\text{cm} \Rightarrow \sqrt{< h^2 >} = 100\,\mu\text{m} \end{aligned}$$

Thus the effect is relatively weak on the scale of vesicles, but relatively strong on macroscopic scales. For a biomembrane fluctuations are relevant, but not on small scales.

It is instructive to compare this result to the one for interfaces under tension (e.g. oil droplets or soap bubbles). The we start from the Hamiltonian

$$\mathcal{H}\left[h(x,y)\right] = \frac{\sigma}{2} \int dxdy (\nabla h(x,y))^2$$

and therefore arrive at

$$< h(\vec{k}) h(\vec{k}') >= \frac{k_B T}{\sigma k^2} \delta(\vec{k} + \vec{k}') \tag{5.63}$$

The backtransform then gives

$$< h^2 >= \frac{k_B T}{2\pi\sigma} \ln(\frac{L}{a}) \tag{5.64}$$

which is a much weaker dependence on L than for membranes. For $\sigma = 100\, erg/cm^2$ and $a = 3$ Å, a system size of $L = 10\ nm$ gives a mean deviation of 1.5 Å. For $L = 1\ cm$, this goes up only to 3.4 Å.

Another way to quantify membrane fluctuations is to investigate how much the membrane loses its orientation due to fluctuations. A measure for this is the

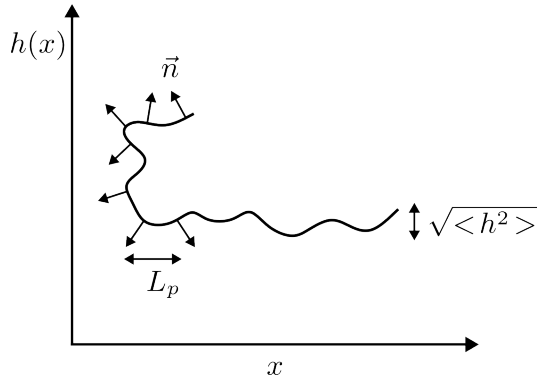

Figure 5.17: Persistent length L_p for fluctuating membrane, Monge representation. $\vec{n}$ is the normal to the membrane vector.

persistence length L_p. Systems with characteristic length shorter than L_p can be considered as elastic planes or rods (for polymers). The properties of systems with characteristic length larger than L_p solutions can be described with statistical methods for random walks. Formally, the persistence length is defined as the length over which correlations in the direction of the normal are lost.

Let us again work in the Monge representation, see figure 5.17. The normal vector is

$$\begin{aligned}\vec{n} = \frac{1}{\sqrt{\det g}} \begin{pmatrix} h_x \\ h_y \\ 1 \end{pmatrix}, \text{ with } \det g = 1 + (\nabla h)^2 \\ = \frac{1}{\sqrt{1 + \partial_x h^2 + \partial_y h^2}} \begin{pmatrix} h_x \\ h_y \\ 1 \end{pmatrix}\end{aligned}$$

Let us define the angle between normal vectors at different points on the membrane as θ and

$$\cos\theta \backsimeq 1 - \frac{\theta^2}{2} = n_z = \frac{1}{\sqrt{1 + \partial_x h^2 + \partial_y h^2}} \simeq 1 - \frac{1}{2}(\underbrace{\partial_x h^2 + \partial_y h^2}_{=(\nabla h)^2})$$

This means that

$$\begin{aligned}< \theta^2 > &= \underbrace{< (\vec{\nabla} h)^2 >}_{\text{avarage over all possible h}} \\ &= \frac{2\pi k_B T}{(2\pi)^2 \kappa} \int_{\frac{2\pi}{L_p}}^{\frac{2\pi}{a}} k\, dk\, \frac{k^2}{k^4} \\ &= \frac{k_B T}{(2\pi)\kappa} \ln\left(\frac{L_p}{a}\right)\end{aligned}$$

If we now set $< \theta^2 >= \pi^2$ for the extreme case that orientation has turned around, we can define a length scale at which the membrane is not flat anymore:

$$\boxed{L_p = a \exp(2\pi^3 \tfrac{\kappa}{k_B T})} \qquad \begin{matrix}\textbf{Persistence length} \\ \textbf{for membranes}\end{matrix} \tag{5.65}$$

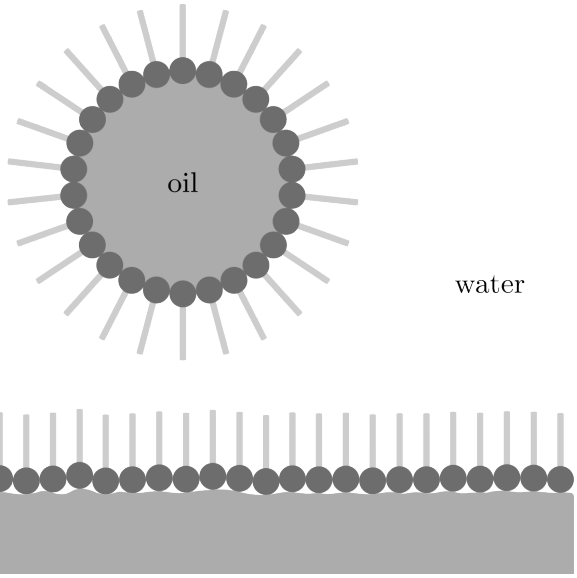

Figure 5.18: Surface interaction between oil and water mediated by tensides. The tensides, represented by red circles with black tails, are responsible for the dispersion of oil droplets into water. They reduce the surface tension, that is why the interface is rough.

The persistence length for membranes was calculated by de Gennes and Taupin in 1982 [29].

For better illustration we look again at typical numbers. As already mentioned in this section, for biomembranes $\kappa \backsimeq 20 k_B T$, which makes $L_p \simeq a \cdot \exp(1240)$. For $a = 1$ nm, this gives $L_p \approx 10^{538}$ m (the diameter of the observable universe is 10^{27} m). Although membranes are only 4 nm thick, this thickness is sufficient to conserve their rigidity and flatness. Another example is the water-oil interface stabilized by tensides (substances, that reduce surface tension and allow easier dispersion), see figure 5.18. In this case $\kappa \simeq 1 \cdot k_B T$, L_p is small and the interface is thermally roughened.

5.3.2 Steric (Helfrich) interactions

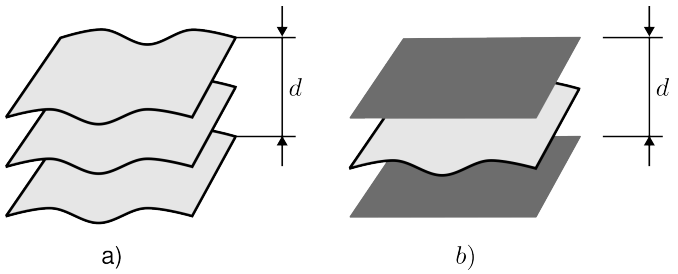

Figure 5.19: Steric interactions for (a) stack of membranes and (b) membrane trapped between two walls. Characteristic dimension is the distance d for both cases. The principal idea for the description of both cases is the same, but there are more degrees of freedom for the stack of membranes.

In the chapter on interactions we have learned that entropic effects might lead to effective interactions, e.g. the attractive depletion interaction between large particles in a sea of small particles or the crystallization of hard spheres at high density. We now will see that entropic effects lead to an effective repulsion between membranes. Consider a stack of membranes or a single membrane trapped between two walls, see figure 5.19. We are interested in the free energy of the system, which in this case is a function of the distance d between the membranes or the membrane and the wall. We already can sense that this free energy will decrease with increasing d because the membrane will gain entropy if the confinement decreases.

Scaling argument

The membrane has "humps" of size $h^2 \sim \frac{k_B T}{\kappa} \cdot L_p^2$ as calculated above. For each hump, the membrane loses entropy per area $\frac{k_B}{L_p^2}$ and the bending energy per area for a hump is $\kappa \left(\frac{h}{L_p^2}\right)^2$. From this argument we can conclude, that the free energy per area is

$$\frac{\Delta F}{A} \sim \kappa \left(\frac{h}{L_p^2}\right)^2 - T\left(\frac{-k_B}{L_p^2}\right) \sim \frac{(k_B T)^2}{\kappa} \cdot \frac{1}{h^2}$$

For a membrane in a stack or between two walls, h scales like d and therefore we get the fluctuation or Helfrich interaction [30]:

$$\boxed{\frac{\Delta F}{A} \sim \frac{(k_B T)^2}{\kappa} \cdot \frac{1}{d^2}} \qquad \text{Helfrich 1978}$$

Although this argument involves bending energy, this too arises from thermal fluctuations. Therefore the whole effect is a thermal one and vanishes with $T \to 0$.

More rigorous treatment

An exact solution is not known, but a reasonable calculation starts with the confinement effect modeled by a harmonic potential [31]. Thus we consider the mean squared deviation in the Monge representation for an almost flat membrane that fluctuates under a harmonic potential:

$$\mathcal{H} = \frac{\kappa}{2} \int dx\, dy \left\{ (\triangle h)^2 + \frac{1}{\xi^4} h^2 \right\} = \frac{1}{2} \int dx\, dy \left\{ \kappa (\triangle h)^2 + \gamma h^2 \right\}$$

where ξ is called the confinement length and γ the confinement parameter. We transform the problem into Fourier space:

$$\begin{aligned} < h^2 > &= \frac{1}{(2\pi)^2} 2\pi \int dk\, k\, \frac{k_B T}{\kappa (k^4 + \xi^{-4})} \\ &= \frac{k_B T}{8\kappa} \cdot \xi^2 = \frac{k_B T}{8\sqrt{\kappa\gamma}} \end{aligned}$$

We now assume a simple geometrical scaling of the excursion with the confinment, $< h^2 >= \mu d^2$. Here μ is a constant prefactor, that has been found in Monte-Carlo

computer simulations to be $\mu = \frac{1}{6}$. Combining the two expressions for $< h^2 >$, we can solve for ξ as a function of d. Because we have a harmonic (Gaussian) system, for the free energy difference between the confined and the free membrane we get (compare the introduction, free energy of a harmonic system)

$$\begin{aligned} \frac{\Delta F}{A} &= -k_B T \cdot \ln Z \\ &= \frac{k_B T}{(2\pi)^2} 2\pi \int k\, dk\, \ln\left(\frac{k^4 + \xi^{-4}}{k^4}\right) \\ &= \frac{k_B T}{8} \cdot \xi^{-2} \end{aligned}$$

From this follows:

$$\boxed{\frac{\Delta F}{A} = \frac{(k_B T)^2}{64 \kappa \mu d^2}} \qquad \text{Steric interaction between membranes}$$

This is the same result as from the scaling analysis, but now with exact prefactors. This result has been confirmed both with computer simulations and in experiments.

If we repeat the same analysis for the case of surface tension, we have for the squared mean displacement

$$< h^2 >= \frac{1}{(2\pi)^2} 2\pi \int dk\, k\, \frac{k_B T}{\sigma k^2 + \gamma} \tag{5.66}$$

Now the integral is not $(1/2)\arctan(k^2)$, but $(1/2)\ln(1 + k^2)$, thus it diverges for large k and we have to use a microscopic cutoff. If we combine both surface tension and bending rigidity, however, we get a well-defined result again.

5.4 Red blood cells

5.4.1 Shape of red blood cells

We have seen above that the Helfrich Hamiltonian predicts shapes that resemble the biconcave disc of a red blood cell (RBC, also known as erythrocyte). However, this discocyte is stable only over a very small range of reduced volume v. The ADE-model predicts a variety of additional shapes, including stomatocytes (shaped like a cup or mouth). However, it does not predict echinocytes (shaped like a hedgehog), which are also often observed for RBCs. In general, there is whole zoo of RBC-shapes seen under different conditions (pH, ATP-concentration, temperature, lipid composition, etc). A comprehensive understanding of these RBC-shapes is very important because it is often used to detect pathological situations by simply checking for shapes under the microscope. In Fig. 5.20 we show the main shapes that are seen experimentally and how they can be predicted computationally. The upper left part shows electron microscopy images arranged in the so-called stomatocyte-discocyte-echinocyte (SDE) sequence, a sequence of shape transitions that can be caused by different agents that all

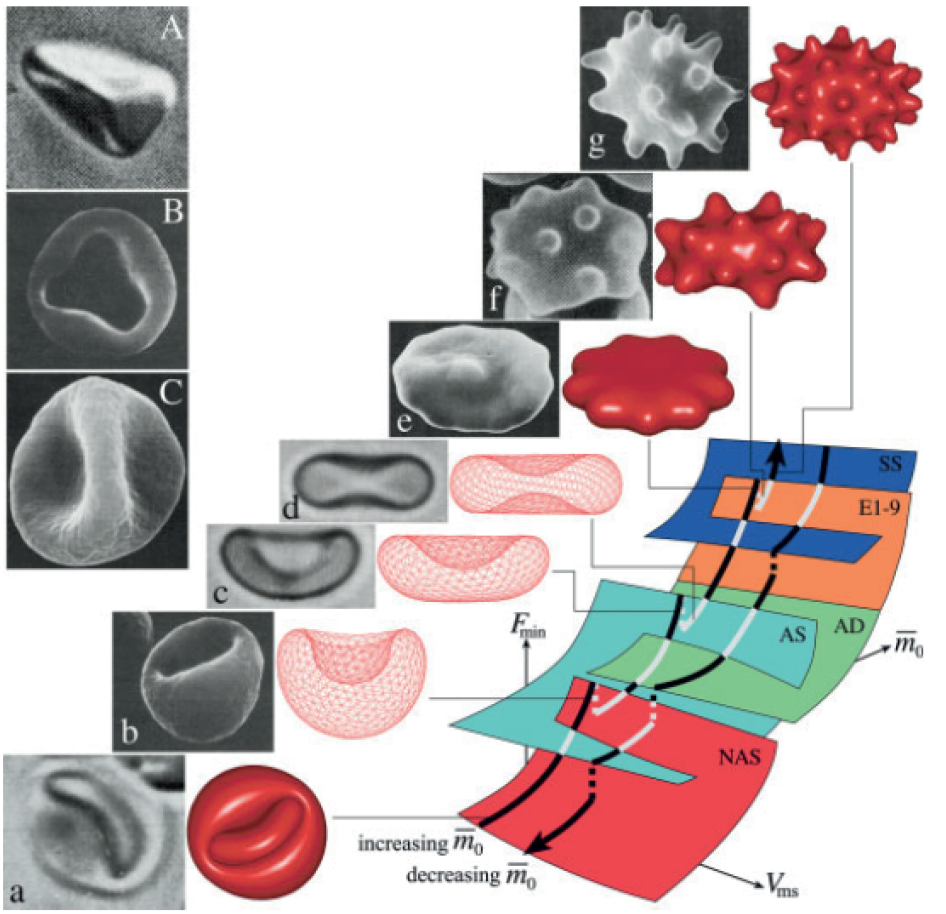

Figure 5.20: Shape of red blood cells: comparison of experimentally observed and computationally predicted shapes and their transitions. From the review by Gerald Lim and colleagues.

seem to have the same physical consequences. The lower right half shows shapes predicted by an expanded ADE Hamiltonian as explained below. It also shows the sequence of free energy surfaces which leads to the transitions. We conclude that the shape of RBCs can be understood very well from physical shape models[2].

We start our discussion with some general remarks on RBCs. First observed by Anton van Leeuwenhoek in 1674, they are the carriers of hemoglobin and therefore of oxygen in our body. During their 120 days lifetime, they travel 10^5

[2]A comprehensive review is given by Gerald Lim H. W., Michael Wortis and Ranjan Mukhopadhyay, Red Blood Cell Shapes and Shape Transformations: Newtonian Mechanics of a Composite Membrane, in the book Soft Matter, Vol. 4: Lipid Bilayers and Red Blood Cells, edited by G. Gompper and M. Schick, Wiley-VCH Weinheim 2008. The original paper was HW Gerald Lim, Michael Wortis and Ranjan Mukhopadhyay, Stomatocyte-discocyte-echinocyte sequence of the human red blood cell, PNAS 99: 16766, 2002. A more recent treatment along these lines is Geekiyanage et al., A coarse-grained red blood cell membrane model to study stomatocyte-discocyte-echinocyte morphologies, PLoS One 14: e0215447, 2019.

times through our circulation (each round trip takes 100 s) before they are sorted out because they become stiffer. There are around 2.6 10^{13} RBCs in our body (out of 3.1 10^{13} all together), making them the most abundant cell type[3]. An amazing number of 2 10^6 new ones are produced in every second in our bone marrow. A RBC has a diameter of 8 μm, a thickness of 2 μm at the rim and of 1 μm at the middle of the biconcave disc. Its volume is 100 μm^3 and its area 140 μm^2. This corresponds to a reduced volume of $v = 0.642$, in agreement with the range from the vesicle theory in which we expect discocytes.

Under physiological conditions, area and volume do not change much and therefore can be taken as constant for our mathematical treatment. For area, this results from the large area expansion modulus of $K_A = 0.5\ J/m^2$. The corresponding energy is $(K_A/2)\Delta A^2/A_0$ and if we equate this with the bending energy $\kappa = 50\ k_BT$ of RBCs, we get $\Delta A/A_0 = 10^{-5}$, thus area does not change significantly. In fact the membrane would rupture at one percent relative area dilation and the large area expansion modulus protects it from this.

Volume control is more complicated. It mainly arises from osmotic pressure arising from $c_0 = 290\ mM$ of osmotically active molecules inside the cell. This leads to an osmotic modulus $K_V = RTc_0 = 7\ 10^5 J/m^3$. Equating the energy $(K_V/2)\Delta V^2/V_0$ with the bending energy κ, we now get $\Delta V/V_0 = 10^{-5}$, thus volume is also constant for practical purposes.

The standard model for RBC-shape was established in the beautiful paper by Lim, Wortis and Mukhopadhyay in PNAS 2002. As shown in Fig. 5.21, the plasma membrane of the RBC is reinforced by a polymer network (made mainly from the intermediate filament spectrin) underlying it, thus forming a composite or sandwich structure. The overall thickness however is so small that the system can still be considered to be two-dimensional on the scale of the cell. Therefore the authors expanded the ADE-model for the membrane by an elastic energy for the polymer network. This elastic component is modeled as an isotropic hyperelastic material. Isotropy is justified by the hexagonal network structure, but linearity is not because the RBC is known to strain harden under the conditions in the blood flow. Similar to the derivation of the Helfrich Hamiltonian, we write the elastic Hamiltonian as a Taylor expansion, but this time not as a function of curvature, but as a function of the two in-plane strain invariants α and β:

$$\mathcal{H} = \frac{K_\alpha}{2}\int dA\left(\alpha^2 + \alpha_3\alpha^3 + \alpha_4\alpha^4\right) + \mu\int dA\left(\beta + b_1\alpha\beta + b_2\beta^2\right) \tag{5.67}$$

where K_α is the stretch modulus and μ the shear modulus. The two strain invariants follow from the principal extension ratios λ_1 and λ_2 of a deformed ellipse as

$$\alpha = \lambda_1\lambda_2 - 1,\ \beta = \frac{1}{2}\left(\frac{\lambda_1}{\lambda_2} + \frac{\lambda_2}{\lambda_1} - 2\right) \tag{5.68}$$

In contrast to the Hamiltonian for the lipid bilayer, one now also needs a reference shape to calculate the elastic energy. A computational procedure has been

[3]Compare the book by Ron Milo and Rob Phillips, Cell biology by the numbers, Garland Science 2016

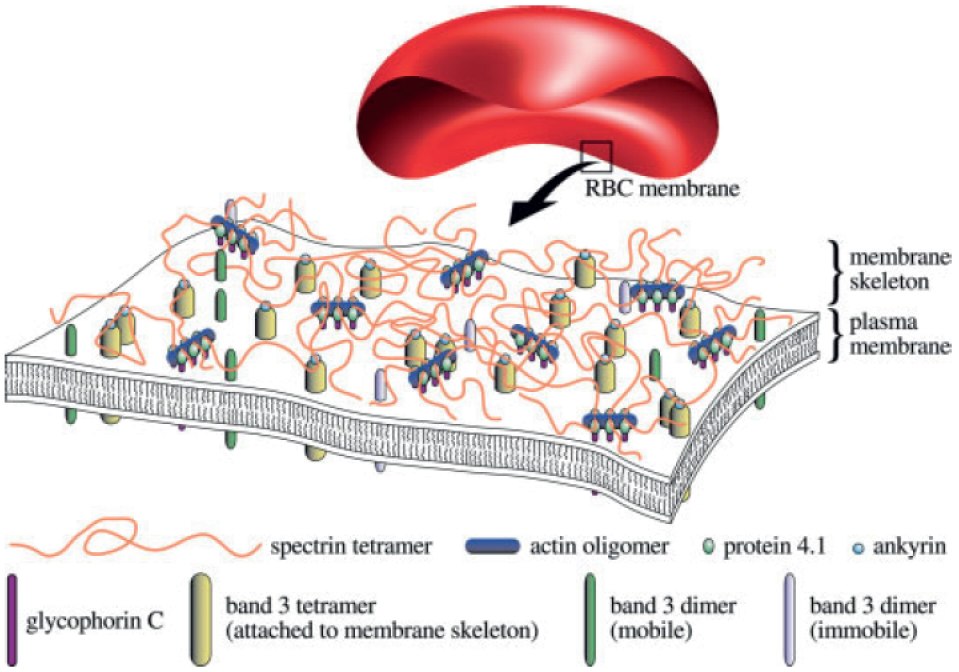

Figure 5.21: The shape of RBCs is determined by the nature of its composite membrane. While the outside layer is a lipid membrane with differential lipid composition in the two leaflets, the inside layer is a polymer network (made mainly from the polymer spectrin) that is attached to the membrane at discrete points (band 3 tetramer, band 4.1 protein). These anchor points form a hexagonal lattice and have a typical distance of 76 nm.

developed to estimate this shape (which is determined by microscopic defects and cannot be measured directly) and it has been found to be an oblate (not a sphere as used by earlier models). The final shape as shown in Fig. 5.20 is then calculated by minimization of triangulated shapes under the combined action of the ADE- and the elastic Hamiltonians. The excellent agreement with the experiments validate the theory. It is also in agreement with the famous 1974 bilayer couple hypothesis by Sheetz and Singer who suggested that different agents lead to the same SDE-sequence because the main control parameter is membrane curvature. Finally the theory explains the origin of the echinocyte, which was missing from the Helfrich-type models: it corresponds to a membrane that wants to bud, but the budding is prevented by strong stretch in the spectrin network.

We finally can ask how RBC-shape changes as the cell is moving in shear flow, both at low and high density (in the blood of healthy persons, RBCs make up 45 percent of the volume, the so-called *hematocrit*). This requires hydrodynamic theories and has been studied recently with many different methods [32]. One finds that single RBCs assume parachute and slipper shapes, and that multiple RBCs arrange in zig-zack-configurations, as observed experimentally. Interestingly, single RBCs at the wall are lifted up due to high Reynolds-number effects and due to their deformability. At physiological hematocrit, they all move as a

plug in the middle of the capillary, leaving a cell-free-layer at the side that effectively lubricates the flow and thus makes it faster than expected for a Newtonian fluid (*Fahraeus effect*). Other cells like white blood cells, platelets, tumour or stem cells also circulating with the blood are expelled from the plug and tend to contact the wall (*margination*).

5.4.2 Flickering spectroscopy for red blood cells

RBCs are continuously fluctuating (*flickering*), as can be observed and measured with an optical microscope. There are two ways to analyze such data. First one can assume that one observes the fluctuations of the membrane as it is constrained by the spectrin network. Then the relevant Hamiltonian would be [33]

$$\mathcal{H}\left[h(x,y)\right] = \int dxdy \left\{ \frac{\sigma}{2}(\nabla h(x,y))^2 + \frac{\kappa}{2}(\Delta h(x,y))^2 + \frac{\gamma}{2}h(x,y)^2 \right\}$$

where γ is a confinement parameter. In Fourier space we then have

$$< h(\vec{k})h(\vec{k'}) >= \frac{k_B T}{\sigma k^2 + \kappa k^4 + \gamma}\delta(\vec{k} + \vec{k'}) \tag{5.69}$$

This procedure has been applied successfully to RBCs under various conditions and is has been found that shape is the main determinant of the fluctuations [34]. We note that assuming an almost flat membrane is a strong assumption and that a more rigorous analysis had to consider also the role of curvature.

Alternatively, one can assume that the whole shell is one composite and fluctuates as such, as we have assumed above to derive the minimal energy shape. Then one has to work with thin shell elasticity and the results are much more complicated. In this way, it has been shown that at low and high frequencies, the fluctuations are dominated by active and passive fluctuations [35, 36]. Active fluctuations depend on ATP and arise e.g. from the actin-spectrin network or ion pumps and channels.

Chapter 6

Physics of polymers

Polymers are chain molecules that can be described as space curves in three dimensions $\vec{r}(s)$ using the language and tools of differential geometry as introduced in the membrane chapter. Motivated by the phenomenological approach to membranes, we could start in a continuum framework with a bending Hamiltonian:

$$\mathcal{H}[\vec{r}(s)] = \frac{\kappa_p}{2} \int_0^L ds \left(\frac{d^2\vec{r}(s)}{ds^2} \right)^2 \tag{6.1}$$

where $\kappa_p = k_B T l_p$ is a bending rigidity for polymers and l_p is the persistence length. This Hamiltonian describes a *semi-flexible polymer* (also called *worm-like chain* (WLC) or *Kratky-Porod model*). Below we will derive it as a limit of the freely rotating chain (FRC) model. In biophysics, this is the most relevant polymer model as many biofilaments (actin, collagen, cellulose, etc) are semi-flexible.

In contrast to membranes, however, this bending Hamiltonian is just one out of several important models. Due to the variety of different types of polymers, their microscopic physics is richer. Note that biomembranes assemble due to the hydrophobic effect and form large structure whose mechanics does not depend on the molecular details of the lipids, while polymers are formed by covalent bonds between monomers who are strongly exposed to the environment. As we will see below, there is actually a simpler phenomenological model for polymers than the WLC:

$$\mathcal{H}[\vec{r}(s)] = \frac{3k_B T}{2b} \int_0^L ds \left(\frac{d\vec{r}(s)}{ds} \right)^2 \tag{6.2}$$

where b is the Kuhn length (effective monomer length) of the polymer. This *Gaussian chain* (GC) model is the continuum limit of the freely jointed chain (FJC) model which is purely entropic in nature. This polymer model is appropriate for many synthetic polymers like for example polyethylene. In this chapter we will discuss both cases (WLC versus GC) as the two most important classes of polymer models[1].

[1]The two standard textbooks on polymer physics are M Doi and SF Edwards, *The theory of*

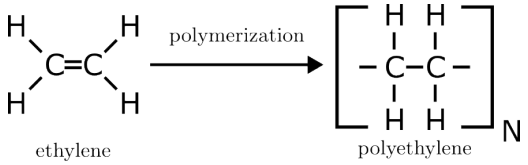

Figure 6.1: Polymerization of ethylene. Polyethylene (PE) is made by opening the double bond between the carbon atoms in ethylene, flipping it over and thus connecting to the next ethylene monomer. The subscript N is the degree of polymerization.

6.1 General introduction to polymers

Polymers are made by binding monomers together in a process called polymerization, see figure 6.1. The number of monomers N, is called degree of polymerization. A typical value for synthetic polymers is $N = 10^5$, but it can go up to $N = 10^{10}$ monomers.

Often monomers can be bonded together in different ways ("isomerism"). Isomers are molecules with the same chemical composition, but different space configuration, see figure 6.2, and hence have different physical properties. Therefore, microscopic interactions are vital for the configurations of polymers. This is true both for the conformation of single chains and for the interactions of different chains.

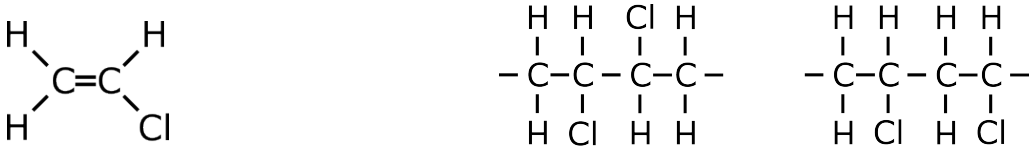

Figure 6.2: Isomers of polyvinyl chloride (PVC)

The study of polymer physics started in the 1920s (mainly through the work of Hermann Staudinger at Freiburg, who was awarded the Nobel prize for chemistry in 1953), when people realized that polymers are chain molecules that can be build up of only one type of monomers (homopolymers) or of different monomers (heteropolymers), see table 6.1.

Polymers can have different architectures, see Table 6.2. This affects many of the physical properties of the polymers, including their size and their interaction, e.g. their ability to slide on top of one another.

If the polymers in a melt are connected by crosslinks one gets a "polymer network". These polymer networks are elastic solids with shape memory, see figure 6.3. Therefore, we can define an elasticity modulus for this polymer gel. To first

polymer dynamics, Oxford University Press 1986 and Michael Rubinstein and Ralph H. Colby, *Polymer physics*, Oxford University Press 2003.

Type of polymer	Sketch	Example
homopolymer	-A-A-...-A-	Homopolymers are mostly synthetic polymers, e.g. PE
heteropolymer	-A-B-A-C-...-	DNA, which has 4 different monomers Proteins, which have 20 different monomers
diblock-copolymer	-A-...-A-B-...-B-	Those are heteropolymers with two blocks, each build up of a different monomer. This structure is similar to lipids.

Table 6.1: Different types polymers, separation on type of building blocks.

Type of polymer	Sketch	Remarks
linear polymer	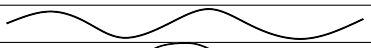	
ring polymer	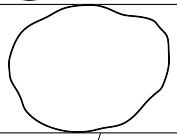	1D analog to vesicles
star polymer	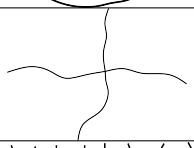	For the description of star polymers one needs to know the number of arms and the length of each one of them In the case of $N \to 0$, it becomes a soft sphere.
comb polymer	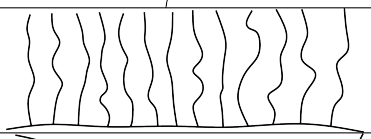	Can be compared with polymer brushes, which have immobile backbones.
H-polymer	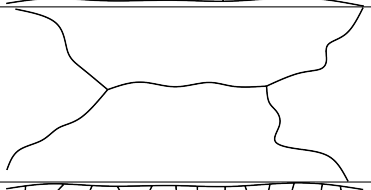	
ladder polymer	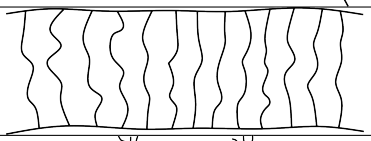	
dendrimer	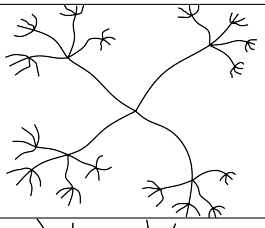	To form a dendrimer you start with a given number of branches, then after a certain length from the end point of each branch evolve the same number of branches and so on. This is a self controling shape, because after a certain number of branches the system becomes too dense, and the growth stops.
branched polymer	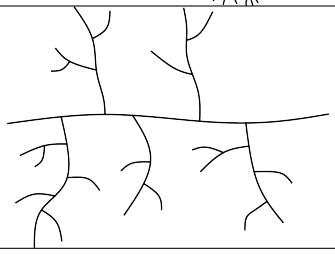	This structure is typical for sugars.

Table 6.2: Polymer architectures.

approximation the Young's modulus is

$$E = \frac{k_B T}{\xi^3} \tag{6.3}$$

where ξ is the meshsize of the network. The most common examples of permanently cross-linked polymer networks are rubber (e.g. vulcanized natural rubber, polyisoprene) and silicone elastomers (e.g. polydimethylsiloxane, PDMS).

If the crosslinkes are not permanent, which is usually the case in biological polymer networks, they will flow like a fluid on a long time scale. The theory of flowing systems is called rheology. A hydrogel is a polymer network in water. In order to investigate the elastic properties of a hydrogel, we have to put the gel between two plates and then rotate or shear them (in conical or parallel plate rheometers, respectively), see figure 6.3. The prime examples for biological hydrogels are cytoskeleton and extracellular matrix, giving structural stability to cells and tissues, respectively.

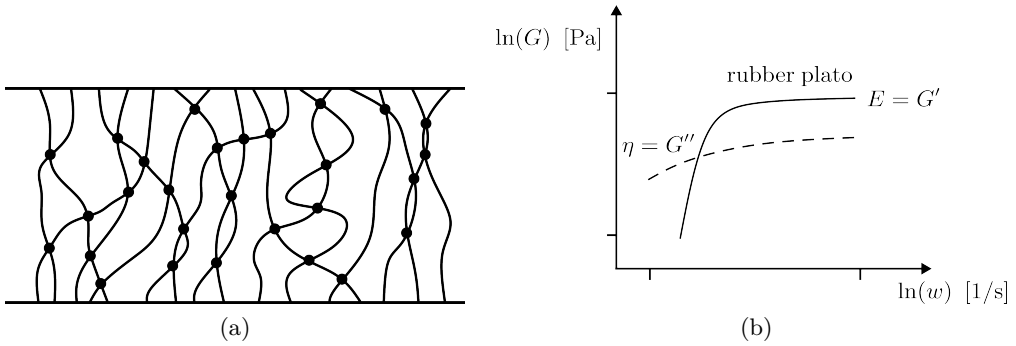

Figure 6.3: The elastic properties of polymer gels can be studied by putting the them between two walls and then rotating or shearing those walls against each other. The typical mechanical behaviour of the polymer network is depicted on the right side. The logarithm of the elastic moduli is shown as a function of the logarithm of the frequency w. At low frequencies the material is viscous, but it becomes elastic at high frequencies.

6.2 Basic models for polymers

6.2.1 Freely jointed chain (FJC)

This is the simplest microscopic model for a polymer. It considers N segments or links, $\vec{r_i}$, each representing a monomer with a constant length a:

$$\begin{aligned} \vec{r_i} &= \vec{R}_i - \vec{R}_{i-1} \\ |\vec{r_i}| &= a \end{aligned}$$

The $\vec{R}_i$ are the position vectors for the nodes of the chain. $\vec{R}$ is the end-to-end vector, giving a characteristic dimension of the polymer, see figure 6.4. As each

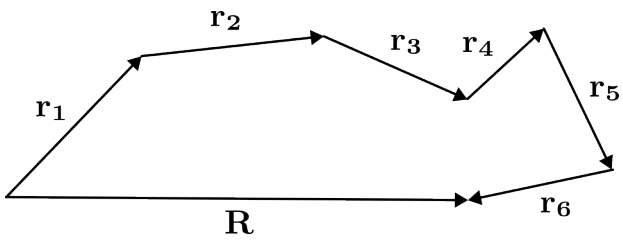

Figure 6.4: Freely jointed chain FJC model for polymers. A short polymer is schematically depicted, as a chain consisting of segments $\vec{r_i}$, represented as vectors. All segments have the same length a. $\vec{R}$ is the end-to-end vector.

link points in a random direction, we have

$$< R >= \sum_{i=1}^{N} < \vec{r_i} >= 0 \ .$$

In analogy to the mean squared deviation $< h^2 >$ for membranes, we look at the mean squared end-to-end distance

$$\begin{aligned} < R^2 > &= < \left(\sum_i \vec{r_i} \right) \left(\sum_j \vec{r_j} \right) > \\ &= \sum_{i=1}^{N} \underbrace{< \vec{r_i}^2 >}_{=a^2} + \sum_{i \neq j} \underbrace{< \vec{r_i} \cdot \vec{r_j} >}_{=0} = Na^2 \end{aligned} \tag{6.4}$$

$$\boxed{R = \sqrt{N} a} \quad \begin{array}{c} \text{typical extension of} \\ \text{polymer chain} \end{array} \tag{6.5}$$

The square root relation is typical for a random walk. We introduce time $t = N\tau$ (with stepping time τ) and get

$$< R^2 >= 2dDt$$

with $D = a^2/2\tau$ the diffusion constant and d spatial dimension. In fact our polymer model is exactly the prescription of how to implement a random walk.

In a real polymer there are correlations between the different bond vectors, $< \vec{r_i} \cdot \vec{r_j} >\neq 0$ even for $i \neq j$. However, in most cases, the polymer becomes "ideal" in the sense that there are no correlations between monomers at large distance along the chain, $< \vec{r_i} \cdot \vec{r_j} >= 0$ for $|i - j| \longrightarrow \infty$. Therefore the sum over these

Ideal polymer	C_∞	b[Å]
polyethylene $-CH_2\,CH_2-$	7.4	14
polybutadiene $-CH_2\,CH=CH\,CH_2-$	5.3	9.6
polyisoprene (rubber) $-CH_2\,CH=CH\,CH\,CH_3-$	4.6	8.2
polydimethylsiloxane (elastomere) $-O\,Si\,(CH_3)_2-$	6.8	13

Table 6.3: Flory's characteristic ratio and Kuhn lengths for different polymers

correlations converges to a finite value:

$$\begin{aligned} < R^2 > &= a^2 \sum_{i=1}^{N} \sum_{j=1}^{N} < \cos\theta_{ij} > \\ &= a^2 \sum_{i=1}^{N} C_i \\ &= a^2 N \underbrace{\frac{1}{N} \sum_{i=1}^{N} C_i}_{=:C_N} \\ &= C_N N a^2 \overset{N\to\infty}{\longrightarrow} C_\infty N a^2 \end{aligned} \tag{6.6}$$

with $C_\infty = C_i\ \forall i$ with $1 \leq C_\infty < \infty$. C_∞ is called " Flory's characteristic ratio", see table 6.3.

Ideal polymers correspond to a FJC with redefined monomer length b and degree of polymerization N:

$$L = N \cdot b,\ < R^2 >= N \cdot b^2 = b \cdot L$$

$$\boxed{\begin{array}{c} b = \frac{<R^2>}{L} \\ N = \frac{<R^2>}{b^2} = \frac{L^2}{<R^2>} \end{array}} \quad \text{Kuhn length} \tag{6.7}$$

The Kuhn length is a measure for the statistical segment length and tabulated in table 6.3.

6.2.2 Freely rotating chain (FRC)

We now fix not only the monomer size a, but also the bond angle θ, see figure 6.5. The degree of freedom that is left is the torsion angle ϕ, which keeps our polymer flexible. For polyethylene, $a = 1.54\,$Å and $\theta = 68^o$. Only the component along the bond vectors is transmitted down the chain. For each bond only a component $\cos\theta$ remains:

$$< \vec{r_i} \cdot \vec{r_j} >= a^2 (\cos\theta)^{|j-i|}$$

Because $\cos\theta < 1$, the series decays exponentially:

$$(\cos\theta)^{|j-i|} = e^{|j-i|\ln(\cos\theta)} = e^{-\frac{|j-i|a}{l_p}} \tag{6.8}$$

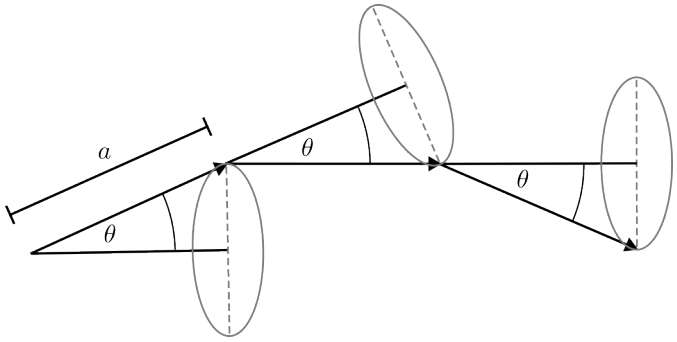

Figure 6.5: Schema of the freely rotating chain model (FRC). Here the length a and the bond angle θ, between the segments, are kept constant. The torsion angle ϕ is still free and makes the FRC flexible.

Here l_p is the persistence length:

$$l_p = -\frac{a}{\ln(\cos\theta)} \tag{6.9}$$

The persistence length has the same meaning as in membrane physics, it denotes the length scale over which the correlations decay.

We now can use this exponential decay to calculate the mean squared end-to-end distance:

$$\begin{aligned}
< R^2 > &= \sum_{i=1}^{N}\sum_{j=1}^{N} < \vec{r_i}\cdot\vec{r_j} > && (6.10)\\
&= \sum_{i=1}^{N}\left(\sum_{j=1}^{i-1} < \vec{r_i}\cdot\vec{r_j} > + < \vec{r_i} >^2 + \sum_{j=i+1}^{N} < \vec{r_i}\cdot\vec{r_j} >\right) && (6.11)\\
&= a^2N + a^2\sum_{i=1}^{N}\left(\sum_{j=1}^{i-1}(\cos\theta)^{i-j} + \sum_{j=i+1}^{N}(\cos\theta)^{j-i}\right) && (6.12)\\
&= a^2N + a^2\sum_{i=1}^{N}\left(\sum_{k=1}^{i-1}(\cos\theta)^{k} + \sum_{k=1}^{N-i}(\cos\theta)^{k}\right) && (6.13)
\end{aligned}$$

The two sums can be extended to infinity because at large distances, the correlation has decayed. We then simply have a geometrical series:

$$\sum_{k=1}^{\infty}(\cos\theta)^k = \frac{\cos\theta}{1-\cos\theta}$$

Therefore

$$< R^2 >= a^2N + 2a^2N\frac{\cos\theta}{1-\cos\theta} \tag{6.14}$$

such that the final result reads

$$\boxed{< R^2 >= Na^2\tfrac{1+\cos\theta}{1-\cos\theta}} \qquad \begin{matrix}\text{mean square}\\ \text{end-to-end distance}\\ \text{for freely rotating chain}\end{matrix} \tag{6.15}$$

If we compare this result with equation 6.6 , we see that $C_\infty = \frac{1+\cos\theta}{1-\cos\theta}$. The values for C_∞ are typically between 5 and 8, see table 6.3.

6.2.3 Worm-like chain (WLC)

In the limit of $\theta \longrightarrow 0$, the chain becomes very stiff and rod-like:

$$\begin{aligned} \cos\theta &\approx 1 - \frac{\theta^2}{2} \\ \ln\cos\theta &\approx -\frac{\theta^2}{2} \end{aligned}$$

That means, that the persistence length l_p and Flory's characteristic ratio C_∞ both diverge:

$$l_p = \frac{2a}{\theta^2} \, , C_\infty = \frac{2 - \frac{\theta^2}{2}}{\frac{\theta^2}{2}} \approx \frac{4}{\theta^2} \tag{6.16}$$

The WLC model as shown in figure 6.6 is defined in the limit $\theta \to 0$ and $a \to 0$ such that $l_p = \frac{2a}{\theta^2} = const.$ Then also the Kuhn length will be finite and simply twice as large as the persistence length:

$$b = \frac{< R^2 >}{L} = \frac{C_\infty N a^2}{Na} = \frac{4a}{\theta^2} = 2l_p \tag{6.17}$$

For example a double stranded DNA (dsDNA) has persistence length $l_p = 50\,\text{nm}$ and Kuhn length $b = 100\,\text{nm}$.

The mean-square end-to-end distance of the WLC can be evaluated using the exponential decay of correlations between tangent vector along the chain:

$$\begin{aligned} < R^2 > &= a^2 \sum_{i=1}^{N} \sum_{j=1}^{N} (\cos\theta)^{|j-i|} \\ &= a^2 \sum_j \sum_i e^{-|j-i|a/l_p} \end{aligned}$$

In the continuum limit we get

$$\begin{aligned} < R^2 > &= \int_0^L du \int_0^L dv \, e^{-|u-v|/l_p} \\ &= \int_0^L du \int_0^u dv \, e^{-(u-v)/l_p} + \int_0^L du \int_u^L dv \, e^{-(v-u)/l_p} \\ &= 2l_pL - 2l_p^2(1 - e^{-L/l_p}) \end{aligned} \tag{6.18}$$

$$\boxed{< R^2 >= 2l_pL - 2l_p^2(1 - e^{-L/l_p})} \tag{6.19}$$

Looking at equation 6.19 we can distinguish two limiting cases:

1. $L \gg l_p$ so we can neglect the exponential term and get a flexible polymer with
$$< R^2 >= 2l_pL = bL = b^2N \ll L^2 \tag{6.20}$$

2. $L \ll l_p$ now the exponential term becomes important and we make a Taylor expansion. Then we get a rigid chain with

$$< R^2 >= 2l_pL - 2l_p^2\left(1 - 1 + \frac{L}{l_p} - \frac{1}{2}\left(\frac{L}{l_p}\right)^2\right) = L^2 \qquad (6.21)$$

The general expression is a smooth crossover between the two, see figure6.6b:

$$\frac{< R^2 >}{L^2} = \frac{2}{x} - \frac{2}{x^2}(1 - e^{-x})$$

with $x = L/l_p$. This defines three different regimes: the flexible chain at $x \gg 1$, the semiflexible chain with $x \approx 1$, and the rigid polymer with $x \ll 1$. Biological examples are DNA, actin and microtubules.

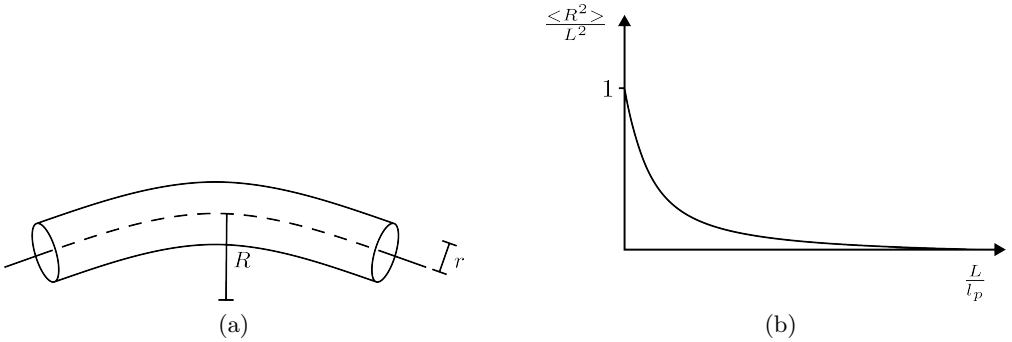

Figure 6.6: a.) The worm-like chain model describes an elastic rod. This polymer model is similar to the Helfrich Hamiltonian for membranes. b.) The dependency of the mean squared end-to-end distance on the ratio of the contour and persistence lengths of a polymer in the WLC model.

6.2.4 Radius of gyration

The mean squared end-to-end distance $< R^2 >$ gives a measure for the extension of the polymer, but it is very hard to measure it directly and what one usually measures in experiments is the *radius of gyration* (e.g. with light scattering or size-exclusion chromatography). We now clarify the relation between the two. Assumed the monomer mass is constant, for the center of mass we have:

$$\vec{R}_{cm} = \frac{1}{N}\sum_{i=1}^{N}\vec{R}_i$$

Now we will calculate the mean squared radius of gyration $< R_g^2 >$:

$$\begin{aligned} R_g^2 &= \frac{1}{N}\sum_{i=1}^{N}(\vec{R}_i - \vec{R}_{cm})^2 \\ &= \frac{1}{N}\sum_{i=1}^{N}({\vec{R}_i}^2 - 2\vec{R}_i\vec{R}_{cm} + \vec{R}_{cm}^2) \\ &= \frac{1}{N}\sum_{i=1}^{N}{\vec{R}_i}^2 \underbrace{\left(\frac{1}{N}\sum_{j=1}^{N}\right)}_{=1} - \frac{1}{N}\sum_{i=1}^{N}2\vec{R}_i\frac{1}{N}\sum_{j=1}^{N}\vec{R}_j \\ &\quad + \left(\frac{1}{N}\sum_{i=1}^{N}\vec{R}_i\right)\left(\frac{1}{N}\sum_{j=1}^{N}\vec{R}_j\right) \\ &= \frac{1}{N^2}\sum_i\sum_j({\vec{R}_i}^2 - \underbrace{2\vec{R}_i\vec{R}_j + \vec{R}_i\vec{R}_j}_{=-\vec{R}_i\vec{R}_j}) \end{aligned} \tag{6.22}$$

This expression does not depend on the choice of summation indices and we rewrite it in a symmetric form:

$$\begin{aligned} R_g^2 &= \frac{1}{N^2}\frac{1}{2}\left[\sum_i\sum_j({\vec{R}_i}^2 - \vec{R}_i\vec{R}_j) + \sum_j\sum_i({\vec{R}_j}^2 - \vec{R}_j\vec{R}_i)\right] \\ &= \frac{1}{2N^2}\sum_i\sum_j({\vec{R}_i}^2 - 2\vec{R}_j\vec{R}_i + {\vec{R}_j}^2) \\ &= \frac{1}{2N^2}\sum_i\sum_j(\vec{R}_i - \vec{R}_j)^2 \\ &= \frac{1}{N^2}\sum_{i=1}^{N}\sum_{j=i}^{N}(\vec{R}_i - \vec{R}_j)^2 \end{aligned}$$

$$\boxed{< R_g^2 >= \tfrac{1}{N^2}\textstyle\sum_{i=1}^{N}\sum_{j=i}^{N} < (\vec{R}_i - \vec{R}_j)^2 >} \tag{6.23}$$

The radius of gyration can be expressed in terms of the average square distance between all pairs of monomers.

For an ideal polymer chain, the sums can be changed into contour integrals:

$$< R_g^2 >= \frac{1}{N^2}\int_0^N du \int_u^N dv \; < (\vec{R}(u) - \vec{R}(v))^2 >$$

We now use the fact that the contour between u and v should behave also like a (shorter) ideal chain, see figure 6.7:

$$< (\vec{R}(u) - \vec{R}(v))^2 >= (v-u)b^2$$

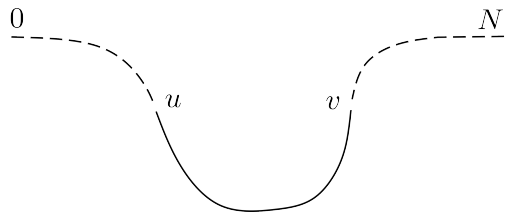

Figure 6.7: Integration along the ideal polymer. Assumption that the contour between u and v also behave like an ideal chain.

with $v \geq u$, Kuhn length b and independent of the outer segments:

$$\begin{aligned} < R_g^2 > &= \frac{b^2}{N^2} \int_0^N du \int_u^N dv\,(v-u) \\ &\overset{v-u=v'}{=} \frac{b^2}{N^2} \int_0^N du \int_0^{N-u} dv'\,v' \\ &= \frac{b^2}{N^2} \int_0^N du\,\frac{1}{2}(N-u)^2 \\ &\overset{N-u=u'}{=} \frac{b^2}{2N^2} \int_0^N du'\,u'^2 = \frac{Nb^2}{6} \end{aligned} \tag{6.24}$$

$$\boxed{< R_g^2 >= \frac{<R^2>}{6}} \quad \text{Debye result} \tag{6.25}$$

This is a very important result. It means that for an ideal chain we can work both with $< R^2 >$ or $< R_g^2 >$, they are essentially the same, except for a constant factor of 6.

6.2.5 Gaussian Chain model (GCM)

Until now we have calculated $< R^2 >$ and $< R_g^2 >$ as measures for the **average** spatial extension of a polymer. We now calculate the full distribution $p(\vec{R})$ for the end-to-end distance of the FJC. We start from the probability distribution for the segments:

$$p(\vec{r_1}, \ldots, \vec{r_N}) = \prod_{i=1}^{N} \frac{1}{4\pi a^2} \delta(|\vec{r_i}| - a) \tag{6.26}$$

In the FJC, the segments have fixed length a, but free orientation. We then have:

$$\begin{aligned} 1 &= \int \left(\prod_{i=1}^{N} d\vec{r_i} \right) p(\vec{r}_1, \ldots, \vec{r}_N) \\ p(\vec{R}) &= \int \left(\prod_{i=1}^{N} d\vec{r_i} \right) p(\vec{r}_1, \ldots, \vec{r}_N) \delta(\vec{R} - \sum_{i=1}^{N} \vec{r_i}) \end{aligned} \tag{6.27}$$

with

$$\delta(\vec{R} - \sum_{i=1}^{N} \vec{r_i}) = \frac{1}{(2\pi)^3} \int d\vec{k}\, e^{i\vec{k}(\vec{R} - \sum \vec{r_i})}$$

We therefore obtain

$$p(\vec{R}) \;=\; \frac{1}{(2\pi)^3} \int d\vec{k}\, e^{i\vec{k}\vec{R}} \left[\int d\vec{r}\, e^{-i\vec{k}\vec{r}} \frac{1}{4\pi a^2} \delta(|\vec{r}| - a) \right]^N$$

Evaluating the integral in the brackets

$$\begin{aligned} \int d\vec{r}\, e^{-i\vec{k}\vec{r}} \frac{1}{4\pi a^2} \delta(|\vec{r}| - a) &= \frac{1}{4\pi a^2} \int_0^\infty r^2 dr \int_0^{2\pi} d\phi \int_0^1 d(\cos\theta)\, e^{-ikr\cos\theta} \delta(r - a) \\ &= \frac{2\pi}{4\pi a^2} \int dr\, r^2 \delta(r - a) 2 \frac{\sin kr}{kr} \\ &= \frac{\sin(ka)}{ka} \end{aligned}$$

because

$$\int_{-1}^{1} e^{-ikrx} dx = \frac{1}{-ikr}(e^{-ikr} - e^{ikr}) = 2\frac{\sin(kr)}{kr} = 2\mathrm{sinc}(kr)$$

So we get:

$$\begin{aligned} p(\vec{R}) &= \frac{1}{(2\pi)^3} \int d\vec{k}\, e^{i\vec{k}\vec{R}} \left(\frac{\sin(ka)}{ka} \right)^N \\ &= \frac{1}{(2\pi)^3} \int d\vec{k}\, e^{i\vec{k}\vec{R}}\, e^{N \ln \frac{\sin(ka)}{ka}} \end{aligned}$$

For $N \gg 1$ the main contribution to the integral comes for the $\vec{k}$ close to the global maximum of $\ln \frac{\sin(ka)}{ka}$ and we can use the saddle-point approximation or method of steepest descent to evaluate the integral. Since $\mathrm{sinc}(x)$ is maximal in $x = 0$, we may write:

$$\ln \mathrm{sinc}(x) \;\approx\; -\frac{x^2}{6}$$

yielding:

$$\begin{aligned} p(\vec{R}) &= \frac{1}{(2\pi)^3} \underbrace{\int d\vec{k}\, e^{i\vec{k}\vec{R}} e^{-\frac{Nk^2a^2}{6}}}_{\text{Gauss integral}} \\ &= \frac{1}{(2\pi)^3} \prod_{\alpha=x,y,z} \int dk_\alpha e^{ik_\alpha R_\alpha - Nk_\alpha^2 \frac{a^2}{6}} \\ &= \frac{1}{(2\pi)^3} \left(\frac{6\pi}{Na^2} \right)^{\frac{3}{2}} e^{-\frac{3}{2}\frac{\vec{R}^2}{a^2 N}} \end{aligned} \tag{6.28}$$

Our final result thus is

$$\boxed{p(\vec{R}) = \left(\frac{3}{2\pi N a^2}\right)^{\frac{3}{2}} e^{-\frac{3\vec{R}^2}{2Na^2}}} \tag{6.29}$$

The distribution function of the end-to-end vector is Gaussian. The feature that $R > Na$ is an artifact of our expansion, but that does not matter, because the respective weights are negligible.

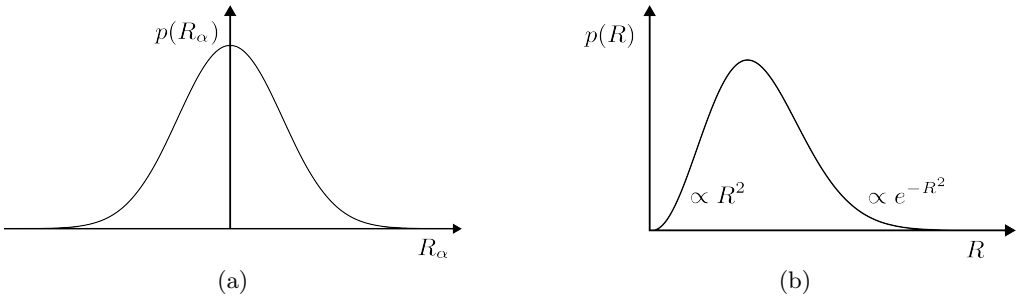

Figure 6.8: (a) Gaussian distribution of one component R_α of the end-to-end distance vector $\vec{R}$. (b) Probability distribution of the radial component of $\vec{R}$ (in spherical coordinates). Note the similarity to the Maxwell-Boltzmann distribution.

Note that we could have guessed beforehand that the resulting distribution is a Gaussian since $\vec{r_i}$ are independent and identically distributed random variables and $\vec{R} = \sum_{i=1}^{N} \vec{r_i}$ should be normal distributed for large N by the virtue of the central limit theorem.

In Cartesian coordinates, equation 6.29 reads for the single components (compare also figure 6.8a):

$$\begin{aligned} & p(\vec{R}) = \prod_{\alpha=x,y,z} \left(\frac{3}{2\pi N a^2}\right)^{\frac{1}{2}} \exp\left(-\frac{3R_\alpha^2}{2Na^2}\right) \\ \Rightarrow \quad & \int dR_\alpha \, p(R_\alpha) = 1 \\ \Rightarrow \quad & < R_\alpha^2 >= \int dR_\alpha \, p(R_\alpha) R_\alpha^2 = \frac{Na^2}{3} \end{aligned} \tag{6.30}$$

In spherical coordinates, one finds for the modulus of the radius:

$$p(R) = \left(\frac{3}{2\pi N a^2}\right)^{\frac{3}{2}} \exp\left(-\frac{3R^2}{2Na^2}\right) \cdot 4\pi R^2 \tag{6.31}$$

This result for $p(R)$ (figure 6.8b) is equivalent to the Maxwell-Boltzmann distribution for the distribution of the modulus of the velocity for an ideal gas. The same Gaussian distribution is obtained by starting from a symmetric random walk on a lattice, i.e. from the binomial distribution.

These results from the FJC motivate us to define a new polymer model that assumes the Gaussian property to be valid for every segment. In the Gaussian chain model (GCM) one assumes that every bond has a Gaussian length distribution

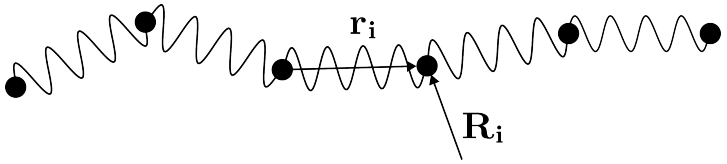

Figure 6.9: The Gaussian Chain Model. The Gaussian length distribution of the bond lengths are depicted as springs with the entropic spring constant k.

(instead of a fixed length a as in the FJC):

$$p(\vec{r}) = \left(\frac{3}{2\pi a^2}\right)^{\frac{3}{2}} \exp\left(-\frac{3\vec{r}^2}{2a^2}\right) \tag{6.32}$$

That implies that $< \vec{r}^2 >= a^2$. With $\vec{r}_i = \vec{R}_i - \vec{R}_{i-1}$ it follows that

$$p(\vec{r_1}, \ldots, \vec{r_N}) = \left(\frac{3}{2\pi a^2}\right)^{\frac{3N}{2}} \exp\left(-\sum_{i=1}^{N} \frac{3(\vec{R}_i - \vec{R}_{i-1})^2}{2a^2}\right) \tag{6.33}$$

This corresponds to a Boltzmann distribution for $N+1$ bonds connected by harmonic springs (compare figure 6.9). The Hamiltonian now reads:

$$\mathcal{H} = \frac{3}{2a^2} k_B T \sum_{i=1}^{N} (\vec{R}_i - \vec{R}_{i-1})^2 \tag{6.34}$$

with

$$\boxed{k = \frac{3k_B T}{a^2}} \qquad \begin{array}{c}\textbf{entropic spring constant} \\ \textbf{of a single bond}\end{array} \tag{6.35}$$

In the continuum limit:

$$\mathcal{H} = \frac{3k_B T}{2a^2} \int_0^N dn \left(\frac{\partial \vec{R}}{\partial n}\right)^2 = \frac{3k_B T}{2a} \int_0^L ds \left(\frac{\partial \vec{R}}{\partial s}\right)^2$$

where we have used the substitution $ds = adn$. Note that this Hamiltonian is fundamentally different from the WLC Hamiltonian from equation 6.1 because it describes stretching and not bending.

We now consider the free energy of the Gaussian chain:

$$\begin{aligned} F &= \underbrace{U}_{=0} - TS \\ &= -T \cdot k_B \ln \Omega(\vec{R}) \\ &= -k_B T \cdot \ln\left(p(\vec{R}) \cdot \int d\vec{R}\, \Omega(\vec{R})\right) \end{aligned}$$

Since $\int d\vec{R}\, \Omega(\vec{R})$ is independent of $\vec{R}$, the free energy F can be written as:

$$\boxed{F = \frac{3}{2} k_B T \frac{\vec{R}^2}{Na^2} + F_0} \tag{6.36}$$

where F_0 does not depend on $\vec{R}$. The free energy of a Gaussian chain increases quadratically with R, because the number of possible configurations and hence the entropy decreases. This leads to Hooke's law:

$$\vec{F} = -\frac{3k_BT}{Na^2} \cdot \vec{R} \tag{6.37}$$

where $3k_BT/(Na^2)$ is the entropic spring constant of the whole chain.

Note that for higher temperatures, the entropic spring constant increases or, in other words, the bonds become harder to stretch. In the limit $T \to \infty$, the chain contracts into a single point. The reason for this suprising behaviour is that the effective energy that is needed to stretch the polymer is entirely related to the loss of entropy. It is therefore easier to stretch polymers with a larger number of monomers N, larger monomer size a and *lower* temperature T. This is different for energy-dominated materials such as metals, which become softer at *higher* temperature.

6.3 Stretching polymers

6.3.1 Stretching the FJC

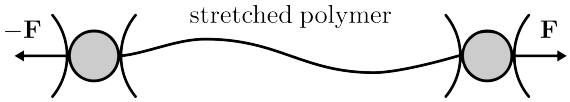

Figure 6.10: A force applied to two beads attached to the polymer, e.g. by optical tweezers. The polymer is stretched and the force needed to stretch it to a certain length is measured.

The entropic spring constant energy of the Gaussian Chain suggests to study the behavior of a FJC under stretch. Imagine placing beads at the ends and pulling them apart along the z-axis with optical tweezers (figure 6.10). Today, the pulling of biopolymers with AFM, optical or magnetic tweezers, electric fields or hydrodynamic flow, to name but a few, is a standard experiment in biophysics. Obviously, the Gaussian result (equation 6.29) cannot be true for large extensions, i.e. close to the contour length. In the following we will approach the problem of calculating the force-extension curve for finite contour length first by a scaling argument and then by an analytical calculation.

Scaling analysis

We now introduce a powerful scaling approach for polymers, namely "blobology". Stretching the polymer changes the symmetry to an oriented random walk. On large scales, the polymer is oriented in z-direction. On small scales ζ, however, it is an unperturbed random walk, represented by a "blob" with ideal chain statistics (figure 6.11):

$$\zeta^2 = gb^2 \tag{6.38}$$

where ζ denotes the blob size and g denotes the number of monomers per blob. Hence, the total number of blobs is simply N/g. From here on we use the symbol b for the Kuhn length as the segment length.

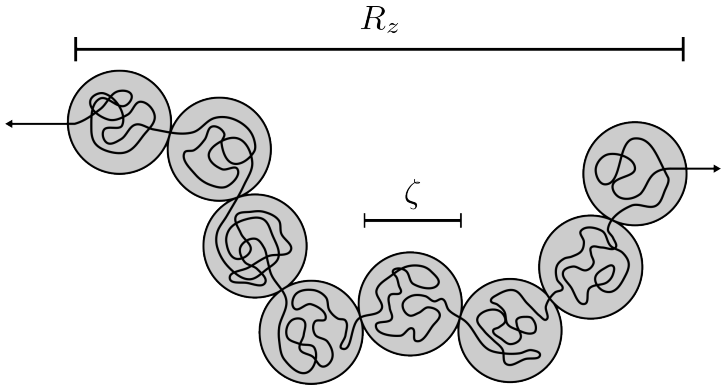

Figure 6.11: Polymer depicted as a chain of "blobs" which on the blob scale ζ behaves as an unperturbed random walk. On the large scale R_z, the blobs are oriented in z-direction.

The blobs are arranged sequentially:

$$R_z \approx \zeta \cdot \frac{N}{g} = \frac{Nb^2}{\zeta} \tag{6.39}$$

$$\Rightarrow \quad \zeta = \frac{Nb^2}{R_z},\ g = \frac{N^2 b^2}{R_z^2} \tag{6.40}$$

Being extended on the large scale R_z, but not on the small scale ζ, allows the chain to maximize its conformational entropy. On the other hand, due to stretching on the length scale ζ a blob becomes oriented and therefore the free energy increases with $k_B T$:

$$F \approx k_B T \cdot \frac{N}{g} \approx k_B T \cdot \frac{R_z^2}{Nb^2} \tag{6.41}$$

As we have now seen, the scaling argument also results in Hooke's law with an entropic spring constant $k = k_B T/(Nb^2)$. Except for a numerical prefactor 3 which does not affect the overall scaling, it is the same as already obtained for the Gaussian chain (equation 6.35).

From the free energy F the force needed to stretch the chain F_z can immediately be calculated:

$$F_z = \frac{\partial F}{\partial R_z} \approx k_B T \cdot \frac{R_z}{Nb^2} = \frac{k_B T}{\zeta} \tag{6.42}$$

Full analytical calculation

We parametrize each bond vector $\vec{r}_i$ as:

$$\vec{r}_i = b \begin{pmatrix} \sin\Theta_i \cdot \cos\phi_i \\ \sin\Theta_i \cdot \sin\phi_i \\ \cos\Theta_i \end{pmatrix} \tag{6.43}$$

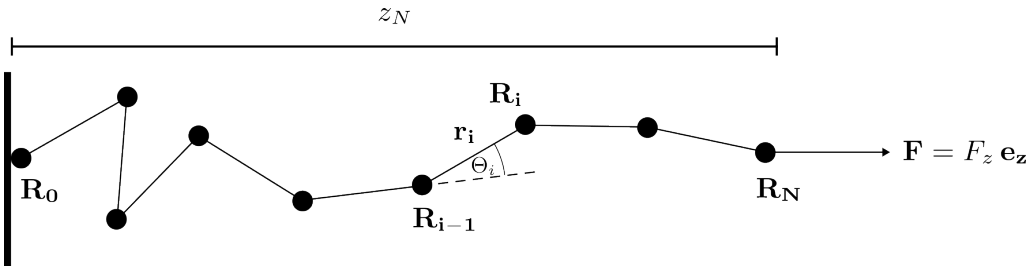

Figure 6.12: A force F_z applied to a freely jointed chain. The chain consists of N bond vectors $\vec{r}_i$ with a fixed length b.

The FJC is purely entropic, but stretching it introduces some energy represented by the following Hamiltonian (compare figure 6.12):

$$\mathcal{H} = -F_z \cdot R_z = -F_z \sum_{i=1}^{N} b \cdot \cos\Theta_i \tag{6.44}$$

$$\begin{aligned}
\Rightarrow \mathcal{Z} &= \int_0^{2\pi} \int_{-1}^{1} \left(\prod_{i=1}^{N} d\phi_i \, d(\underbrace{\cos\Theta_i}_{:=x_i}) \right) e^{-\frac{\mathcal{H}}{k_B T}} \\
&= \int_0^{2\pi} \int_{-1}^{1} \left(\prod_{i=1}^{N} d\phi_i \, dx_i \right) \exp\left(\underbrace{\frac{F_z b}{k_B T}}_{:=f} \cdot \sum_{i=1}^{N} x_i \right) \\
&= \left(2\pi \int_{-1}^{1} dx \, e^{fx} \right)^N \\
&= \left[\frac{2\pi}{f} (e^f - e^{-f}) \right]^N = \left(\frac{4\pi}{f} \sinh(f) \right)^N
\end{aligned} \tag{6.45}$$

For the free energy F we find:

$$F = -k_B T \ln \mathcal{Z} = -k_B T N [\ln(4\pi \sinh f) - \ln f] \tag{6.46}$$

With the free energy, the expectation value of the spatial extension in z-direction can be computed:

$$\begin{aligned}
&< R_z >= -\frac{\partial F}{\partial F_z} = -\frac{\partial F}{\partial f} \cdot \frac{\partial f}{\partial F_z} \\
\Rightarrow \quad &\boxed{< R_z >= bN \cdot [\coth f - \tfrac{1}{f}] = bN \cdot \mathcal{L}(\mathrm{f})}
\end{aligned} \tag{6.47}$$

where we introduced the Langevin function $\mathcal{L}(f)$. Equation 6.47 has two interesting limits (compare also figure 6.13):

1. **The limit of small force: $\mathbf{f \ll 1}$.**

In this regime $\mathcal{L}(f)$ can be approximated by a linear function:

$$\begin{aligned}
\coth f &= \frac{e^f + e^{-f}}{e^f - e^{-f}} \\
&\approx \frac{(1 + f + \frac{1}{2}f^2) + (1 - f + \frac{1}{2}f^2)}{(1 + f + \frac{1}{2}f^2 + \frac{1}{6}f^3) - (1 - f + \frac{1}{2}f^2 - \frac{1}{6}f^3)} = \frac{\frac{1}{f} + \frac{f}{2}}{1 + \frac{1}{6}f^2} \\
&\approx (\frac{1}{f} + \frac{f}{2})(1 - \frac{1}{6}f^2) \\
&\approx \frac{1}{f} + \frac{1}{3}f \\
\Rightarrow \mathcal{L}(f) &\approx \frac{f}{3}
\end{aligned}$$

$$\Rightarrow \boxed{< R_z >= bN \frac{F_z b}{3 k_B T}} \tag{6.48}$$

2. **The limit of large force: $\mathbf{f \gg 1}$.**
   In this regime we find

$$\begin{aligned}
\coth f &\approx \frac{e^f}{e^f} = 1 \\
\Rightarrow \mathcal{L}(f) &= 1 - \frac{1}{f}
\end{aligned}$$

$$\Rightarrow \boxed{< R_z >= bN \left(1 - \frac{k_B T}{F_z b}\right)} \tag{6.49}$$

   The force F_z diverges at the contour length $L = bN$:

$$F_z = \frac{k_B T}{b} \left(\frac{L}{L - < R_z >}\right) \tag{6.50}$$

   with an exponent -1.

6.3.2 Stretching the WLC

Bending Hamiltonian

In the beginning of this chapter we already encountered the bending Hamiltonian of the WLC in arc-length parametrization, compare equation 6.1:

$$\mathcal{H} = \frac{\kappa_p}{2} \int_0^L ds \left(\frac{d^2\vec{r}}{ds^2}\right)^2 = \frac{\kappa_p}{2} \int_0^L ds \left(\frac{d\vec{t}}{ds}\right)^2 \tag{6.51}$$

where $\vec{t}$ is the tangential vector ($|\vec{t}| = 1$). There are three ways to derive this Hamiltonian:

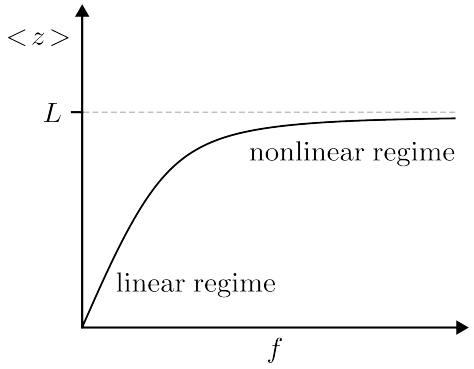

Figure 6.13: The expectation value of the extension in z-direction as a function of the (dimensionless) force parameter $f = F_z b/(k_B T)$ (left) and vice versa. For small force and small extension, respectively, the relation is approximately linear. For large forces the extension approaches the contour length L and the force diverges.

1. **Phenomenologically**, similar to the Helfrich-Canham Hamiltonian for membranes.

2. From **beam theory**: With the Young's modulus E of the elastic rod one finds

$$\kappa_p \quad = \quad E \cdot I \tag{6.52}$$

where

$$I \quad = \quad \int dA \, \frac{r^2}{2} = 2\pi \int_0^R r dr \, \frac{r^2}{2} = \frac{\pi R^4}{4} \tag{6.53}$$

denotes its area moment of inertia (compare figure 6.6).

3. From **microscopic models** such as the FRC, see above.

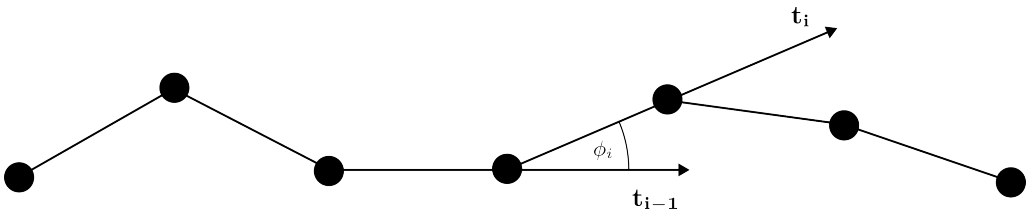

Figure 6.14: The WLC, discretized into small segments.

The bending energy can be calculated by discretizing the WLC into small segments as shown in figure 6.14. This model is similar to the FRC. However, the main difference is that for the FRC the angle Θ was held constant whereas now the second moment $< \Theta^2 > \sim k_B T b/\kappa_p$ is a constant. The bending Hamiltonian

in equation 6.51 then gives

$$\begin{aligned} E_b &= \sum_{i=1}^{N} \frac{\kappa_p}{2b} \cdot (\vec{t}_i - \vec{t}_{i-1})^2 \\ &= \sum_{i=1}^{N} \frac{\kappa_p}{b} \cdot (1 - \cos\Theta_i) \\ \overset{\text{small curvature}}{\Rightarrow} E_b &\approx \sum_{i=1}^{N} \frac{\kappa_p}{2b} \Theta_i^2 \end{aligned} \tag{6.54}$$

Persistence length

In the continuum model the tangential vector diffuses on a sphere (theory of rotational random walks). With Greens function formalism it can be shown that this leads to

$$< \vec{t}(s) \cdot \vec{t}(0) > \;=\; e^{-\frac{k_B T}{\kappa_p} \cdot s} = e^{-\frac{s}{l_p}} \tag{6.55}$$

where

$$\boxed{l_p = \frac{\kappa_p}{k_B T}} \qquad \textbf{persistence length} \tag{6.56}$$

Equation 6.56 can be made plausible by a simple scaling argument (similar to the Bjerrum length in electrostatistics):

$$\begin{aligned} \underbrace{k_B T}_{\substack{\text{thermal} \\ \text{energy}}} &= \underbrace{\frac{\kappa_p}{2} L \cdot \frac{1}{R_{bend}^2}}_{\text{bending energy}} \\ \overset{\substack{\text{on scale } l_p \\ L \approx R_{bend}}}{\Rightarrow} \quad k_B T &= \frac{\kappa_p}{2 l_p} \\ \Rightarrow \quad l_p &\sim \frac{\kappa_p}{k_B T} \end{aligned}$$

Values of the persistence length can vary from several nm ($l_p = 50\,nm$ for ds-DNA) to several μm ($l_p = 17\,\mu m$ for actin) or even several mm ($l_p = 6\,mm$ for microtubules).

With the persistence length we can calculate the mean-square end-to-end distance as before (compare eq. 6.19):

$$\begin{aligned} < \vec{R}^2 > &= \int_0^L du \int_0^L dv \, \exp\left(-\frac{|u-v|}{l_p}\right) \\ &= 2 l_p L - 2 l_p^2 (1 - e^{-\frac{L}{l_p}}) = L^2 f(l_p/L) \end{aligned} \tag{6.57}$$

with $f(x) = 2x - 2x^2(1 - e^{-1/x})$. Below we will make use of the scaling function $f(x)$.

Extension in z-direction

We now stretch the WLC into z-direction:

$$\frac{\mathcal{H}}{k_BT} = \frac{l_p}{2}\int_0^L ds\left(\frac{d\vec{t}}{ds}\right)^2 - \underbrace{\frac{F_z}{k_BT}}_{:=f}\underbrace{\int_0^L ds\, t_z}_{R_z} \tag{6.58}$$

$$\Rightarrow \textbf{extension} \quad < R_z >= \frac{1}{\mathcal{Z}}\int \mathcal{D}\vec{t} R_z e^{-\frac{\mathcal{H}}{k_BT}} = \frac{d\ln\mathcal{Z}}{df} \tag{6.59}$$

In contrast to the FJC an exact solution to equation 6.59 is not known. However, the two asymptotic limits can be treated analytically:

1. **small stretch, $\mathbf{fR_z \ll 1}$:**

We can expand the partition sum $\mathcal{Z}$ in small values of f:

$$\begin{aligned}\mathcal{Z} &= \int \mathcal{D}\vec{t}\, e^{-\frac{l_p}{2}\int_0^L ds\left(\frac{d\vec{t}}{ds}\right)^2}\cdot\left[1 + f\int_0^L dst_z + \frac{f^2}{2}\int_0^L du\int_0^L dv\, t_z(u)t_z(v) + \mathcal{O}(f^3)\right] \\ &= \mathcal{Z}_0\left[1 + f\int_0^L ds\underbrace{< t_z >_0}_{=0} + \frac{f^2}{2}\int_0^L du\int_0^L dv\ < t_z(u)t_z(v) >_0\right]\end{aligned}$$

Since

$$\int_0^L du\int_0^L dv\ < t_z(u)t_z(v) >_0 = \frac{1}{3} < \vec{R}^2 > \overset{L\gg l_p}{\approx} \frac{1}{3}\cdot 2Ll_p$$

we finally find for the partition sum:

$$\mathcal{Z} = \mathcal{Z}_0\left[1 + \frac{f^2 l_p L}{3}\right] \tag{6.60}$$

And hence with equation 6.59

$$< R_z > = \frac{\frac{2fl_pL}{3}}{1 + \frac{f^2 l_p L}{3}} \approx \frac{2fl_pL}{3}$$

$$\Rightarrow \quad \boxed{< R_z >= \tfrac{2l_pL}{3k_BT}\cdot F_z} \qquad \textbf{extension of WLC for small forces} \tag{6.61}$$

Therefore the extension of the WLC in response to a small stretch exhibits, similar to the FJC, a linear force-extension dependency with an entropic spring constant $k_{WLC} = 3k_BT/(2l_pL)$. Recall, that for the entropic spring constant for the FJC we found $k_{FJC} = 3k_BT/(bL)$ (compare equation 6.48).

2. **large stretch, $\mathbf{fR_z \gg 1}$**

In this regime we are dealing with an almost straight chain and can therefore use a Monge parametrization for $\vec{t}$ (compare figure 6.15a):

$$\vec{t} = \begin{pmatrix} t_x \\ t_y \\ 1 - \frac{1}{2}(t_x^2 + t_y^2) \end{pmatrix} \tag{6.62}$$

where for the z-component we have used the fact that $\vec{t}$ is normalized and a Taylor expansion. Our Hamiltonian now reads

$$\begin{aligned} \frac{\mathcal{H}}{k_B T} &= \frac{l_p}{2} \int ds \left[\left(\frac{dt_x}{ds}\right)^2 + \left(\frac{dt_y}{ds}\right)^2 + \underbrace{\left(\frac{dt_z}{ds}\right)^2}_{\approx 0} \right] - f \int ds\, t_z \\ &= \frac{l_p}{2} \int ds \left[\left(\frac{dt_x}{ts}\right)^2 + \left(\frac{dt_y}{ds}\right)^2 \right] + \frac{f}{2} \int ds \left[t_x^2 + t_y^2 \right] - f \cdot L \end{aligned} \tag{6.63}$$

This Hamiltonian is quadratic and therefore the partition sum is a Gaussian path integral (the constant term does not matter). In Fourier space we thus have

$$\overset{\text{Fourier}}{\Rightarrow} |t_\alpha(k)|^2 = \frac{k_B T}{k_B T (l_P k^2 + f)} \tag{6.64}$$

$$\begin{aligned} \Rightarrow < R_z > &= \int_0^L ds \; < t_z > = \int_0^L ds \; < (1 - \frac{1}{2}(t_x^2 + t_y^2) > \\ &= L - \frac{1}{2} \int_0^L ds \, (< t_x^2 > + < t_y^2 >) = L - \frac{1}{2} L \cdot 2 < t_x^2 > \\ &= L \cdot (1 - \frac{1}{2\pi} \int_{-\infty}^{\infty} dk \, \frac{1}{l_p k^2 + f}) = L \cdot (1 - \frac{1}{2\pi f} \int_{-\infty}^{\infty} dk \, \frac{1}{(\sqrt{\frac{l_p}{f}} k)^2 + 1}) \\ &= L \cdot (1 - \frac{1}{2\pi f} \sqrt{\frac{f}{l_p}} \underbrace{\int_{-\infty}^{\infty} dk\prime \, \frac{1}{k\prime^2 + 1}}_{\pi}) \\ &= L(1 - \frac{1}{2\sqrt{f l_p}}) \end{aligned} \tag{6.65}$$

$$\Rightarrow \quad \boxed{\frac{L - < R_z >}{L} = \frac{1}{2\sqrt{f l_p}}} \tag{6.66}$$

This is a square-root divergence $\sim 1/\sqrt{F_z}$ (figure 6.15b). Recall that the FJC in the large extension regime diverges with $1/F_z$ (compare equation 6.50) which is crucially different. In experiments, stretching semiflexible biopolymers like dsDNA has shown that they can *not* be described by the FJC[2].

[2]Smith, Steven B., Laura Finzi, and Carlos Bustamante. Direct mechanical measurements of the elasticity of single DNA molecules by using magnetic beads. Science 258.5085 (1992): 1122-1126; Bustamante, C., Marko, J. F., Siggia, E. D., and Smith, S. Entropic elasticity of lambda-phage DNA. Science (1994): 1599-1599; Bustamante, Carlos, Zev Bryant, and Steven B. Smith. Ten years of tension: single-molecule DNA mechanics. Nature 421.6921 (2003): 423-427.

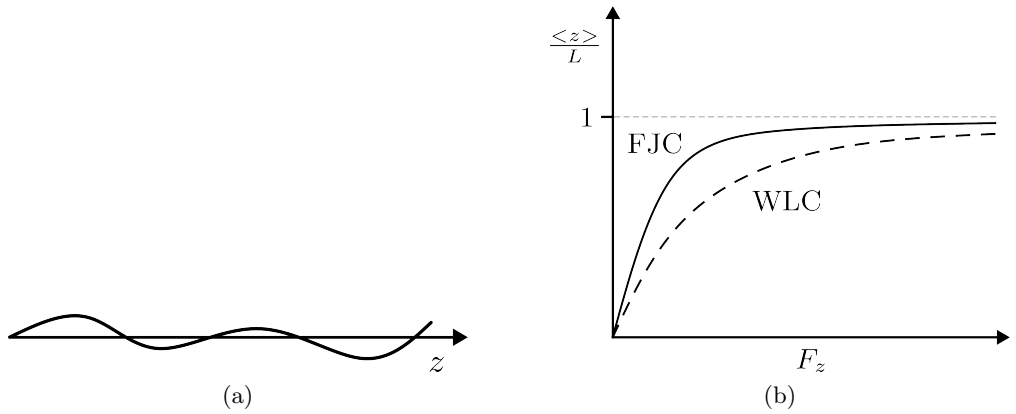

Figure 6.15: (a) A WLC under large stretch. The polymer is now almost straight and can be assumed to have no overhangs. Hence, in analogy to membrane physics, we can chose a parametrization that is similar to the Monge parametrization. (b) Force-extension dependence for the FJC and the WLC. For the FJC the scaling is $(L- < R_z >)/L \sim F_z^{-1}$, whereas for the WLC we find $(L- < R_z >)/L \sim F_z^{-1/2}$.

Although an exact formula for the WLC is still lacking, the two limits shown here can be combined in an interpolation formula with an error smaller than 10%[3]:

$$\text{1. small stretch} \qquad f \cdot l_p = \frac{3 < R_z >}{2L}$$

$$\text{2. large stretch} \qquad f \cdot l_p = \frac{1}{4 \cdot (1 - \frac{<R_z>}{L})^2}$$

$$\Rightarrow \boxed{f \cdot l_p = \frac{F_z l_p}{k_B T} = \frac{<R_z>}{L} + \frac{1}{4 \cdot (1 - \frac{<R_z>}{L})^2} - \frac{1}{4}} \qquad \textbf{interpolation formula} \tag{6.67}$$

Scaling analysis of stretched WLC

The two limiting cases of the stretched WLC can be obtained also from a blob scaling analysis, which helps to better understand the underlying physics. We consider a chain segment of length l which is bent to an angle θ. As discussed above, this costs the bending energy

$$E_b \sim \frac{\kappa_p (1 - \cos\theta)}{l} \approx \frac{\kappa_p \theta^2}{l} \tag{6.68}$$

which diverges with $l \to 0$, because we would get infinite curvature. In order to work against the external force F_z, we need the stretching energy

$$E_s \sim F_z l (1 - \cos\theta) \approx F_z l \theta^2 \tag{6.69}$$

that increases with l. Therefore a crossover length ξ exists at which the two energies balance:

$$\xi := \sqrt{\frac{\kappa_p}{F_z}} = \sqrt{\frac{k_B T l_p}{F_z}} \ . \tag{6.70}$$

[3] JF Marko and ED Siggia: "Stretching DNA", Macromolecules 1995, 28:8759–8770

We interpret ξ as the contour length per blob. Below it, the chain does not feel the effect of force and is dominated by bending. Above it, the chain becomes elongated in z-direction and is dominated by stretching. In the blob picture, we assume that we have an unperturbed WLC below ξ and a stretched FJC of blobs above ξ.

We next recall the two scaling functions that we have calculated above. For the unperturbed WLC, we have defined a scaling function $f(x)$ for the mean squared end-to-end distance in eq. 6.57. We now use it to define the size of a blob as

$$b_b^2 := \xi^2 f(\frac{l_p}{\xi}) \ . \tag{6.71}$$

For the FJC of blobs, we can use the Langevin function $\mathcal{L}(x)$ defined in eq 6.47. We note that we have L/ξ blobs, each of size b_b, and therefore the overall relative extension will be

$$\frac{< R_z >}{L} \sim \frac{1}{L}\frac{L}{\xi} b_b \mathcal{L}(\frac{F_z b_b}{k_B T}) \tag{6.72}$$

where b_b depends on the regime in which the scaling function $f(x)$ is evaluated. A closer look shows that the overall result is controled only by one scaling parameter, namely $f := F_z l_p/(k_B T)$.

We now can look at the two limiting cases. For strong stretching, $f \gg 1$, we have $\mathcal{L}(x) = 1 - 1/x$ and $f(x) = 1$. Thus $b_b = \xi$ (the blob is rigid with linear scaling) and therefore

$$\frac{< R_z >}{L} \sim 1 - \sqrt{\frac{k_B T}{F_z \xi}} \ . \tag{6.73}$$

We rearrange to find

$$\frac{L - < R_z >}{L} \sim \sqrt{\frac{k_B T}{F_z l_p}} \tag{6.74}$$

exactly as found above, except that the scaling analysis misses a factor of 2.

For weak stretching, $f \ll 1$, we have $\mathcal{L}(x) = x/3$ and $f(x) = 2x$. Thus $b_b^2 = 2\xi l_p$ (the blob is flexible with square root scaling) and we get

$$\frac{< R_z >}{L} \sim \frac{\sqrt{\xi l_p}}{\xi}\frac{F_z \sqrt{\xi l_p}}{k_B T} = \frac{F_z l_p}{k_B T} \tag{6.75}$$

because ξ cancels out. This is the linear response regime that we also found above. Here we miss a numerical factor of 2/3 compared with the exact result. Overall we conclude that the blob analysis gives the right scaling results in both limits, in particular the inverse square root for the divergence at strong stretching, which sets the WLC apart from the FJC, and the linear response regime at weak stretching.

Final remarks on stretching the WLC

Experimentally, biopolymers have been shown to correspond to the WLC-model in many different cases, most prominently in the case of dsDNA[4]. For dsDNA,

[4]Smith, Steven B., Laura Finzi, and Carlos Bustamante. Direct mechanical measurements of the elasticity of single DNA molecules by using magnetic beads. Science 258.5085 (1992): 1122-

but also for other biopolymers like actin, it is known that after the thermal fluctuations in the contour length have been pulled out, the backbone can give out additional length due to internal changes (overstretching in the case of dsDNA, twist in the case of actin). This situation is described by the stretchable WLC-model, which can be solved with the same methods as described above for the WLC-model, and which is a combination of the GC and the WLC.

The following references are recommended for further reading:

- R Phillips et al., Physical biology of the cell, chapter 10; especially appendix 10.8 on the math of the WLC on page 401
- P Nelson, Biological Physics, very detailed discussion of different models
- Kroy, Klaus, and Erwin Frey. Force-extension relation and plateau modulus for wormlike chains. Physical Review Letters 77.2 (1996): 306.
- J Kierfeld et al. Stretching of semiflexible polymers with elastic bonds, Eur. Phys. J. E 2004, 14:17-34
- Koester, S., J. Kierfeld, and T. Pfohl. Characterization of single semiflexible filaments under geometric constraints. The European Physical Journal E 25.4 (2008): 439-449.

6.4 Interacting polymers

6.4.1 Self-avoidance and Flory theory

Until now we have neglected the fact that the chain can encounter itself and then becomes repelled as is the case for a real polymer. Due to this excluded volume effect real chains are more extended than ideal ones. The **Edwards-Hamiltonian** takes account of the excluded volume:

$$\beta\mathcal{H} = \frac{k}{2}\int_0^L ds \left(\frac{\partial\vec{r}}{\partial s}\right)^2 + w\int_0^L ds \int_0^L ds\prime\, \delta(\vec{r}(s) - \vec{r}(s\prime)) \qquad (6.76)$$

where w denotes the excluded volume parameter. Unfortunately, further calculation with the Edwards Hamiltonian are rather complicated.

The *Flory theory* offers a very simple and powerful approach to the problem. Here we take a look at the scaling of the involved contributions to the free energy F, namely energy and entropy:

1. **Interaction energy**: we assume infinitely hard potentials that repel monomers. Each collision of the polymer with itself costs k_BT in energy. With a monomer density of $\rho = N/R^3$ and an excluded volume v we end up with an internal free energy:

$$F_{int} \approx k_BTv\rho N = k_BTv\frac{N^2}{R^3} \qquad (6.77)$$

1126; Bustamante, C., Marko, J. F., Siggia, E. D. and Smith, S. (1994). Entropic elasticity of lambda-phage DNA. Science 1599-1599.

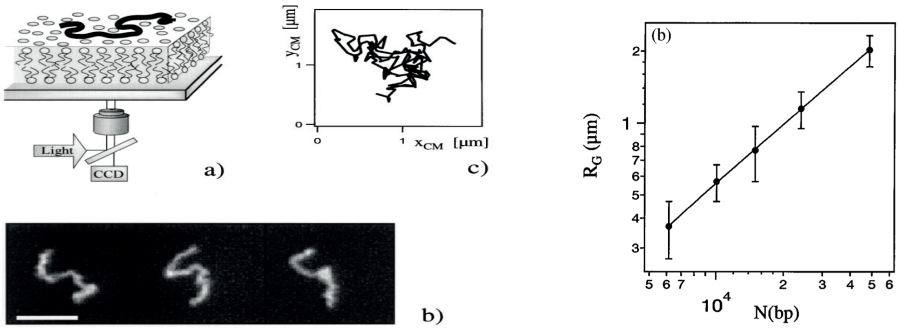

Figure 6.16: The extension of DNA has been measured on supported bilayers and resulted in an exponent 0.79 very close to 2D Flory theory. From B. Maier and J.O. Rädler, Phys. Rev. Lett. 82, 1911, 1999.

2. **Stretching**: what is the counterforce avoiding that the polymers spreads out due to excluded volume effects? Of course this costs entropy as the polymer would be less able to fluctuate. Assuming we stretch a Gaussian chain (compare equation 6.36):

$$F_{stretch} \approx k_B T \frac{R^2}{Nb^2} \tag{6.78}$$

This results in a total free energy:

$$F = F_{int} + F_{stretch} = k_B T (v\frac{N^2}{R^3} + \frac{R^2}{Nb^2}) \tag{6.79}$$

The optimal size R_F follows from the minimizing the free energy F with respect to R:

$$\frac{\partial F}{\partial R} = 0 = k_B T \left(-3v\frac{N^2}{R_F^4} + 2\frac{R_F}{Nb^2} \right)$$

$$\Rightarrow R_F = v^{\frac{1}{5}} b^{\frac{2}{5}} N^{\frac{3}{5}} \tag{6.80}$$

$$\Rightarrow \boxed{R_F \sim N^\nu} \quad \text{with} \quad \nu = \frac{3}{5} = 0.6 \tag{6.81}$$

Computer simulations and experiments yield $\nu = 0.588$. Thus Flory theory seems to be close to reality. In d dimensions one finds $\nu = 3/(d+2)$, which agrees with the exact results in $d = 2$ ($\nu = 3/4$) and $d = 4$ ($\nu = 1/2$). In two dimensions, this exponent has been measured for negatively charged DNA of various lengths absorbed to positively charged lipid bilayers, compare figure 6.16.

However, it is very difficult to improve on Flory theory. The reason is that its success is due to a fortuitous cancellation of errors since both the repulsion energy and the entropic stretching are overestimated. Nevertheless it is very useful for many situations of interest, such as polyelectrolytes, ring polymers or adsorption.

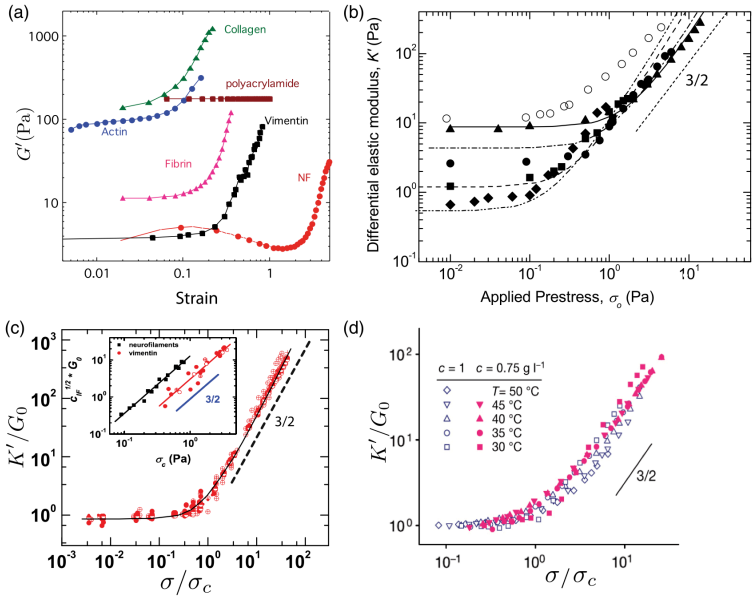

Figure 6.17: Experimental results and scaling laws for the modulus of different polymer networks. (a) Note that the synthetic polyacrylamide gel is the only one that does not strain-stiffen. (b) Actin network crosslinked by scruin. (c) Neurofilament network. (d) Polyisocyanopeptide hydrogel. The power 3/2 is the prediction of the affine thermal model. Taken from Broedersz and MacKintosh review, figure 15.

6.4.2 Semiflexible polymer networks

The mechanical stability of cells and tissues results mainly from networks of semiflexible polymers (e.g. actin inside the cells and collagen between the cells). These kinds of networks are stabilized both by topological entanglement and by crosslinkers (e.g. alpha-actinin, fascin, filamin, fimbrin, scruin etc for actin). Despite the fact that molecular details and network architecture can vary widely in these systems, they all share one outstanding property, namely that they stiffen under strain, as shown in the experimental plots shown in figure 6.17. We have seen this already for the single WLC, but it is non-trivial to find this result also for the network. A nice review on this subject is by Chase P. Broedersz and Fred C. MacKintosh, Reviews of Modern Physics 2014, volume 86, pages 995-1036.

We cannot go into the details here, but would like to mention one difficulty: if one couples different polymers into a bulk material, most deformation modes will include both stretch and compression of polymers. However, these two modes are very asymmetric on the level of the molecules. Under compression, the polymer does buckle at the Euler threshold. This can be seen easily by noting that the thermal fluctuation of a beam is

$$\mathcal{H} \sim (\sigma + \kappa k^2)k^2 \tag{6.82}$$

which can become negative for $\sigma < -\kappa k^2$. Because the critical wavelength is

related to beam length L by $k^* = \pi/L$, we get for the critical tension at buckling

$$\sigma_c = -\kappa(\frac{\pi}{L})^2 = -\pi^2 E(\frac{R}{L})^2 \tag{6.83}$$

with bending stiffness $\kappa = ER^2$, Young's modulus E and radius R. Thus the longer a polymer, the more easily it buckles. A complete theory of a polymer gel has to incorporate this asymmetry, the scale on which the polymers are crosslinked, and the nature of the crosslinks.

Chapter 7

Molecular motors

Molecular motors are molecules that generate motion and force. They do this by converting electrochemical energy into mechanical work, for example by hydrolysing ATP or by letting ions flow down a gradient. Thus they work like heat engines, but they cannot be Carnot engines, because molecular diffusion is too fast as to allow for any temperature gradients. Thus they have to achieve the conversion without the intermediate form of heat and to operate at constant temperature (isothermally). Molecular motors are extremely fascinating molecular machines and it is still not completely clear how they have been optimized by evolution to perform their tasks. An important aspect of understanding them is to build new ones, for example by reengineering their different parts or by using different material (e.g. small molecules or DNA rather than proteins). In 2016, the Nobel prize for chemistry has been awarded *for the design and synthesis of molecular machines* and a Nobel prize for medicine for the investigation of biological molecular motors might come in the future.

Why did nature evolve motors? Obviously this is a very direct way to generate force, e.g. in the muscle for moving body parts or in the beating flagella of sperm cells. In regard to transport, for examples of vesicles and organelles, but also of viruses, motors are needed not only to provide specificity and direction, but also to beat the physical limits of diffusion. With a typical molecular diffusion constant of $(10\ \mu m)^2/s$, diffusion starts to become slow in regard to the required response times of s on the length scale of cells ($10\ \mu m$). With a typical velocity of $\mu m/s$, molecular motors outcompete diffusion on cellular and tissue length scales. However, we also note that for body length scales, we need other transport modes. For example, small molecules such as hormones and many cell types (red blood cells, platelets, white blood cells, stem cells and cancer cells) are transported with the blood (average velocity 0.4 m/s in the aorta and 0.3 mm/s in the capillaries) and nerve impulses are transmitted as action potentials (velocities 10-100 m/s).

In this chapter, we will discuss the theoretical basis of understanding molecular motors. As we will see, the appropriate framework is the one of stochastic equations (master equation, Fokker-Planck equation) and the theory of molecular motors has advanced considerably over the last two decades and still is a very

active research area [1].

7.1 Classification

Molecular motors can be classified in the following way:

Translational motors These motors move along tracks, e.g. myosin motors along actin filaments (e.g. in the muscle), kinesin and dynein along microtubules (e.g. kinesin in axons for transport towards the synaptic cleft, and dynein in cilia and flagella to bend them), and polymerases and helicases along DNA.

Rotary motors These motors typically have a stator embedded into the membrane and containing a rotor. The most important example is the F_0 F_1 ATP Synthase, which in cells of all species generates ATP from ADP and P_i (1 ATP per 120 degree rotation, at 100 Hz this gives 300 ATP per second). It is driven by a proton gradient and needs six protons for each turn. An adult burns 120 W and needs 2.400 kcal / day and thus 1.7×10^{26} ATP molecules, amounting to 140 kg that are essentially produced in our mitochondria. The required energy comes from our metabolism (aerobic respiration of glucose, which essentially was produced before by plants using photosynthesis). If there is plenty of ATP, the motor reverses and builds up the proton gradient. Another famous example is the bacterial flagellar motor, which is basically constructed like a ion turbine using 1.000 protons to drive one turn. This motor has to create more torque than the ATP Synthase because it has to turn the bulky flagellum.

Polymerization motors By (de)polymerization, biopolymers like actin or MT can create force. The most important example is the lamellipodium of migration cells, when a complete network is polymerized against the leading membrane to push the cell forward. Another example are pili of bacteria that pull against their environment by depolymerization of the base in order to move the cell forward.

Translocation motors These are used to push biomolecules through a hole, e.g. when an empty virus capsid is loaded with DNA, when proteins are targeted into a proteasome for degradation, or when a folding protein is threaded from a ribosome directly into another compartment.

Although these motors are very different on the molecular level, they share the basic principle, namely stochastic operation at constant temperature to create biased movement along cyclic phase space trajectories.

[1] In the introduction and the discussion of the force-velocity relation, we follow the book Physical biology of the cell by Rob Phillips and coworkers. For the more mathematical discussion, we follow two excellent review papers on this subject: Frank Jülicher, Armand Ajdari and Jacques Prost, Modeling molecular motors, Reviews of Modern Physics 69, 1269-1281, 1997; Tom Duke, Modelling motor protein systems, course 3 in Physics of bio-molecules and cells, volume 75 of the Les Houches series, pages 95-143, 2002.

In order to foster model building, we start with the simplest example, namely a translational motor walking along a track. We consider a processive motor like kinesin or myosin V, that can make many steps without falling off the track (this is different for non-processive motors like myosin II, that stay on track only for a short time and thus can work productively only in groups). Such motors are typically two-headed and move in a hand-over-hand fashion. Moreover each step is related to exactly one ATP being consumed. We label the track position by the spatial coordinate x and assume that each motor has only a finite number of discrete states, which we label with the index m. Thus our central quantity is the probability $p_m(x,t)$ to be in state m and at position x at time t.

7.2 One-state model

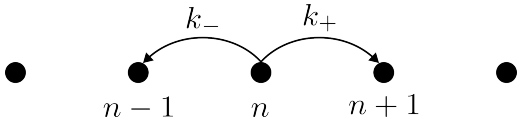

Figure 7.1: Scheme of a one state model.

We start with a one-state model, thus we can drop the label m. We assume that the motor jumps to the right and to the left with rates k_+ and k_-, respectively. Note that in a model for passive physical particles, these two rates should be equal; here we already assume some kind of symmetry break that for molecular motors should be related to track polarity and ATP consumption. We allow only for discrete binding sites at $x = na$. We now deal with a discrete one-dimensional random walk with bias and can write the following flux balance:

$$p(n,t+\Delta t) = k_+\Delta t p(n-1,t) + k_-\Delta t p(n+1,t) + (1-k_-\Delta t - k_+\Delta t)p(n,t) \quad (7.1)$$

The two gain terms come from motors hopping in from left and right, respectively, and the two loss terms come from motors hopping away to the left and right, respectively. We rearrange and take the continuum limit $\Delta t \to 0$ to get

$$\dot{p}(n,t) = k_+(p(n-1,t) - p(n,t)) + k_-(p(n+1,t) - p(n,t)) \quad (7.2)$$

We next take the continuum limit in regard to space and use the Taylor expansion

$$p(x \pm a, t) \approx p(x,t) \pm p'(x,t)a + \frac{1}{2}p''(x,t)a^2 \quad (7.3)$$

We then end up with the famous Fokker-Planck or Smoluchowski equation

$$\dot{p}(x,t) = -vp'(x,t) + Dp''(x,t) \quad (7.4)$$

with drift velocity and diffusion constant defined by

$$v = (k_+ - k_-)a, \; D = (k_+ + k_-)\frac{a^2}{2} \quad (7.5)$$

For a Delta function as initial condition, this equation is solved by

$$p(x,t) = \frac{1}{\sqrt{4\pi Dt}} e^{-(x-vt)^2/4Dt} \tag{7.6}$$

Thus the motor moves with a drift velocity v to the right, but it also disperses with a diffusion constant D.

We also note that one can derive a dispersion relation from here. We use the Fourier ansatz $p(x,t) = C\exp(i(kx - \omega t))$ and get

$$(-i\omega + vik + Dk^2)C = 0 \tag{7.7}$$

which in turn leads to

$$\omega = vk - iDk^2 \tag{7.8}$$

The first term is well-known from e.g. electromagnetic waves (photons) or mechanical waves in crystals (phonons), which have linear dispersion relations (for phonons only for small k). The second term is special for diffusion.

7.3 Force dependence

Next we discuss the force dependence of the motor drift velocity $v = (k_+ - k_-)a$. We go back to the discrete picture and consider steady state, so the time dependence drops out. The principle of detailed balance says that at equilibrium, the currents between two states should cancel each other:

$$k_+ p(n) = k_- p(n+1) \tag{7.9}$$

The state probabilities themselves should obey Boltzmann statistics in equilibrium:

$$p(n) = \frac{1}{Z} e^{-\beta(G_n + Fna)} \tag{7.10}$$

where G_n is the Gibbs free energy at position n and F is the external force against which the motor has to work. Thus equilibrium dictates

$$\frac{k_+}{k_-} = e^{-\beta(\Delta G + Fa)} \tag{7.11}$$

where $\Delta G = G_{n+1} - G_n$. Obviously ΔG has to be negative for the motor to gain free energy as it moves to the right hand side (compare Fig. 7.2a). We immediately see that the motor gets stalled ($v = 0$) if the force reaches the stall force value $F_s = -\Delta G/a$ (we define a positive force to pull to the left).

We now turn to non-equilibrium. As we have seen, the equilibrium considerations only determine how the ratio of the two rates should depend on F. In the absence of more information, we now consider two extreme cases. We first consider the possibility that the force dependence resides completely in k_+. Then we get for the force-velocity relation

$$v(F) = a(k_+(F) - k_-) = ak_- \left(e^{-\beta(\Delta G + Fa)} - 1\right) \tag{7.12}$$

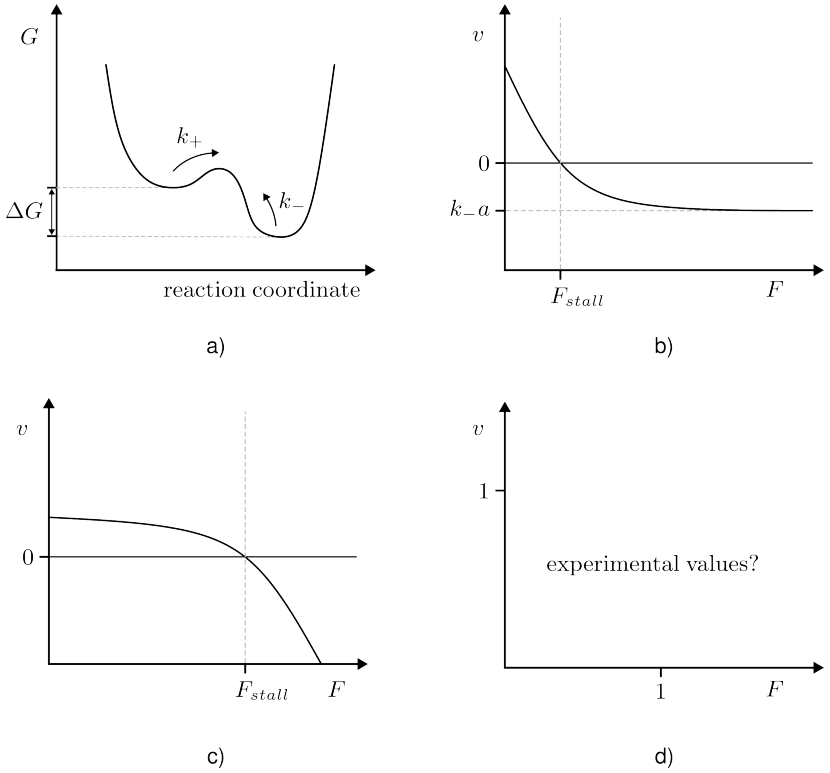

Figure 7.2: Force dependence. a) Scheme how force will change the free energy landscape of a motor hopping to the right. b) Force-velocity relation when force dependence is in k_+. c) Force-velocity relation when force dependence is in k_-. d) Some experimentally measured force-velocity relations: kinesin (green), RNA polymerase (blue), phage packaging motor (red). All four graphs taken from the book Physical Biology of the Cell, chapter 16 on molecular motors.

using the equilibrium condition from equation 7.11. Thus we get a finite free velocity at $F = 0$, then a convex up decay to the stall force F_s and finally a plateau at negative values (compare 7.2b). Indeed such a force-velocity relation is known from many motors, e.g. for myosin II (although this is a non-processive motor, so this is the average result when working in a group) and to some extent for kinesin.

An alternative scenario would be that the force dependence resides completely in k_-. We then get

$$v(F) = a(k_+ - k_-(F)) = ak_+ \left(1 - e^{\beta(\Delta G + Fa)}\right) \tag{7.13}$$

This force-velocity relation is convex down (compare Fig. 7.2c) and is similar to the one measured for myosin V, although the divergence to negative values at large F is of course unrealistic. Fig. 7.2d) shows some examples for measured force-velocity curves and demonstrates that we were able to capture their general features well with our simple one-state model.

7.4 ATP dependence

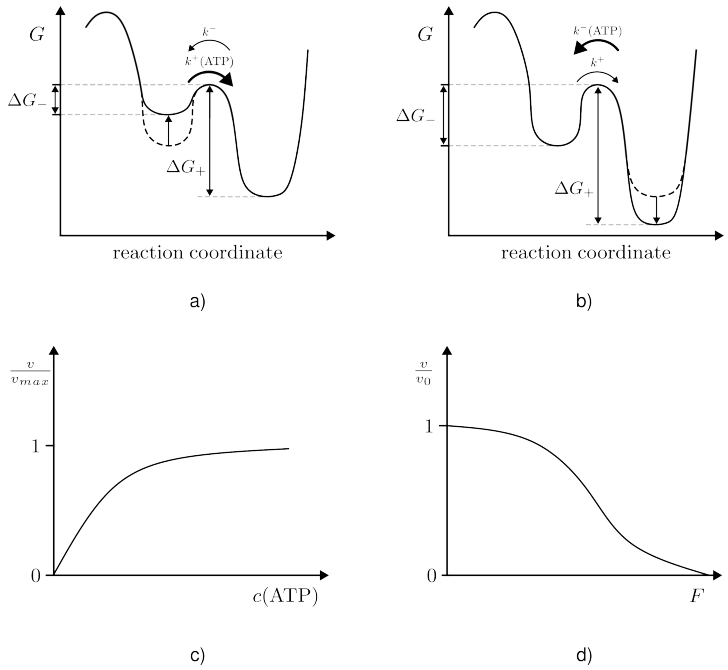

Figure 7.3: ATP dependence. a) When the ATP-dependence is only in the forward rate, then only the free energy barrier height ΔG_+ changes when ATP concentration is changed. b) When the ATP-dependence is only in the backward rate, then only the free energy barrier height ΔG_- changes when ATP concentration is changed. b) The experimental results for kinesin show the linear dependence at low ATP and the plateau at high ATP predicted by the theory. d) Force dependence of kinesin for different ATP concentrations. All four graphs taken from the book Physical Biology of the Cell, chapter 16 on molecular motors.

Like for the force dependence, we start with a statement how the free energy landscape is changed by ATP-concentration. We use the well-known formula for dilute solutions (derivation with chemical potential for ideal gas):

$$\Delta G_h = \Delta G_0 - k_B T \ln \frac{[ATP]}{[ADP][P_i]} \tag{7.14}$$

The first term represents the energetic part of breaking the high-energy bond in ATP and gives a value around $-12.5 k_B T$ (to avoid entropic effects, here we consider very high concentrations, namely M). The second term represents the entropic part and corresponds to the law of mass action. For physiological conditions ($[ATP] = mM$, $[ADP] = 10\mu M$, $[P_i] = mM$) and the reference concentration of M to make the argument dimensionless, we get $-11.5 k_B T$. Thus together we have $\Delta G_h = -24 k_B T$. Note that an ATP-molecule is an energy currency that is valid twice as much inside the cell than with the reference concentrations, because the cell keeps ATP at a much higher concentration than ADP. In general, the free energy gain from ATP-hydrolysis depends on environmental conditions

but usually is between $20k_BT$ and $30k_BT$. This is usually more than enough for a molecular motor to perform its powerstroke. With a powerstroke distance of around $8nm$ and a stall force of around $5pN$ (typical values for kinesin), we have an energy of $40nmpN \approx 10k_BT$, which correspond to an efficiency of around 0.5, if one ATP-molecule gives around $20k_BT$.

Like for the force dependence, the equilibrium considerations do not completely determine the ATP-dependence of the jump rates. We again consider the two extreme cases that the external factor affects only one of the two rates. We first consider that ATP only affects the forward rate. We now use Kramers reaction rate theory that states that the transition rate k depends on attempt frequency Γ and barrier height ΔG as

$$k = \Gamma e^{-\beta \Delta G} \tag{7.15}$$

The exponential dependence between barrier height and transition rate is also known as Arrhenius factor in physical chemistry and should not be understood to be a Boltzmann factor. This law means that the transition rate goes down dramatically (exponentially) if the barrier height increases.

For our problem we can write

$$-\Delta G_h = \Delta G_- - \Delta G_+ \tag{7.16}$$

to relate the two barrier heights to each other (we count the two barrier heights as positive, while the free energy difference is negative, therefore the minus sign on the left). If we assume that only the forward rate is changed by ATP, then this means that only ΔG_+ is changed when changing ATP (compare Fig. 7.3(A)). We now can write the two rates as

$$k_+ = \Gamma_+ e^{-\beta \Delta G_+} = \Gamma_+ e^{-\beta(\Delta G_- + \Delta G_h)} \tag{7.17}$$

$$k_- = \Gamma_- e^{-\beta \Delta G_-} \tag{7.18}$$

and therefore the velocity follows as

$$v = a(k_+([ATP]) - k_-) = a(\Gamma_+ e^{-\beta(\Delta G_- + \Delta G_0)} \frac{[ATP]}{[ADP][P_i]} - \Gamma_- e^{-\beta \Delta G_-}) \tag{7.19}$$

where except for $[ATP]$, all other quantities are constant. Thus it increases linearly with ATP-concentration. However, this relation cannot be valid at high $[ATP]$, because then the barrier disappears (the left well is pushed up over the barrier) and Kramers theory is not valid anymore. Thus this must be a result for low $[ATP]$.

As the second case, we assume that only the backward rate is ATP-dependent. Now only the barrier height ΔG_- is assumed to be ATP-dependent (compare Fig. 7.3(B)) and we get

$$k_+ = \Gamma_+ e^{-\beta \Delta G_+} \tag{7.20}$$

$$k_- = \Gamma_- e^{-\beta \Delta G_-} = \Gamma_- e^{-\beta(\Delta G_+ - \Delta G_h)} \tag{7.21}$$

and therefore

$$v = a(k_+ - k_-([ATP])) = a(\Gamma_+ e^{-\beta\Delta G_+} - \Gamma_- e^{-\beta(\Delta G_+ - \Delta G_0)} \frac{[ADP][P_i]}{[ATP]}) \quad (7.22)$$

Thus now the dependence is inverse in $[ATP]$. The divergence at low $[ATP]$ cannot be valid because then the barrier vanishes (the right well is pushed up over the barrier). Thus this result says that the dependence should plateau at high $[ATP]$.

Together, we now have found that the velocity should increase linearly at low $[ATP]$ and the plateau at a constant value at high $[ATP]$. This is exactly the experimentally measured dependence for all motors. Fig. 7.3(C) shows this for kinesin. The plateau velocity is typically around $\mu m/s$ and the crossover concentration at sub-mM. Fig. 7.3(D) shows the force-velocity relation for kinesin for different ATP concentrations.

7.5 Two-state model

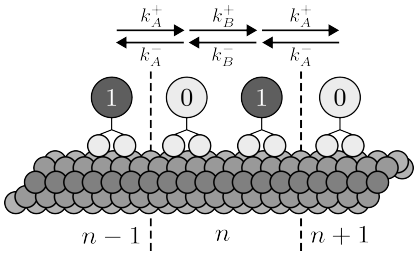

Figure 7.4: In the two-state model, the motor in state 0 has to convert to state 1. During this process, it can remain stationary or take a step to the left. The motor in state 1 has to convert to state 0. During this process, it can remain stationary or take a step to the right.

Molecular motors are often modeled as N-state systems. The different states of the system are difficult to determine, this requires careful experimentation or molecular dynamics simulations. As a first step towards the complexity of molecular motors, we consider $N = 2$. Thus each motor has two internal states, 0 and 1, with probabilities $p_0(n,t)$ and $p_1(n,t)$, respectively. The system can move to the left and right only through the state 0 and 1, respectively, with the rates given in Fig. 7.4. The corresponding master equations are

$$\frac{dp_0(n,t)}{dt} = k_A^+ p_1(n-1,t) + k_B^- p_1(n,t) - k_A^- p_0(n,t) - k_B^+ p_0(n,t)\,, \quad (7.23)$$

$$\frac{dp_1(n,t)}{dt} = k_A^- p_0(n+1,t) + k_B^+ p_0(n,t) - k_A^+ p_1(n,t) - k_B^- p_1(n,t)\,. \quad (7.24)$$

These dynamical equations can be solved by using a continuum limit and a Fourier ansatz. To obtain the drift velocity, however, it is sufficient to use steady state arguments. We introduce the total probabilities to be in state 0 or 1: $P_i(t) = \sum_n p_i(n,t)$. The different positions in the master equation now do not

matter anymore because we sum over them. The dynamic equations for the total probabilities follow from above as

$$\frac{dP_0(t)}{dt} = (k_A^+ + k_B^-)P_1(t) - (k_A^- + k_B^+)P_0(t)\,, \tag{7.25}$$

$$\frac{dP_1(t)}{dt} = (k_A^- + k_B^+)P_0(t) - (k_A^+ + k_B^-)P_1(t)\,. \tag{7.26}$$

These linear equations can be solved easily. For the steady state, however, we do not even have to do this, but we simply set the time derivatives to zero and get

$$(k_A^+ + k_B^-)P_1^{ss} = (k_A^- + k_B^+)P_0^{ss} \tag{7.27}$$

With the normalization $P_0^{ss} + P_1^{ss} = 1$, we finally get

$$P_0^{ss} = \frac{(k_A^+ + k_B^-)}{(k_A^- + k_B^- + k_A^+ + k_B^+)}\,, \tag{7.28}$$

$$P_1^{ss} = \frac{(k_A^- + k_B^+)}{(k_A^- + k_B^- + k_A^+ + k_B^+)}\,. \tag{7.29}$$

We now can calculate the drift velocity:

$$v = a(k_A^+ P_1^{ss} - k_A^- P_0^{ss}) = \frac{(k_A^+ k_B^+ - k_A^- k_B^-)}{(k_A^- + k_B^- + k_A^+ + k_B^+)} \tag{7.30}$$

from which we can also read of the effective rates defined by $v = a(k_+ - k_-)$:

$$k_+ = \frac{(k_A^+ k_B^+)}{(k_A^- + k_B^- + k_A^+ + k_B^+)}\,, \tag{7.31}$$

$$k_- = \frac{(k_A^- k_B^-)}{(k_A^- + k_B^- + k_A^+ + k_B^+)}\,. \tag{7.32}$$

We note that this form of the overall rate is rather generic and also follow e.g. for the steady state approximation of Michaelis-Menten kinetics for enzymatic processes. The numerator is a product of rates because it describes a sequence of steps, and the denominator is a sum of all rates, which is the speed limit for the process.

7.6 Ratchet model for single motors

In principle, we now could go on with a two-state model and try to solve the corresponding master equation in time. We also could start to include more relevant states, compare Fig. 7.5 for myosin II, which generates force in our muscles. As one can see from the scheme, the different states can be grouped into bound and unbound. Thus we have arrived at the model class of *crossbridge models*, where a motor cycles between bound and unbound by forming a crossbridge to the filament. In a three-state model, we would in addition add the powerstroke on the filament. We also could add the recovery stroke and distinguish between

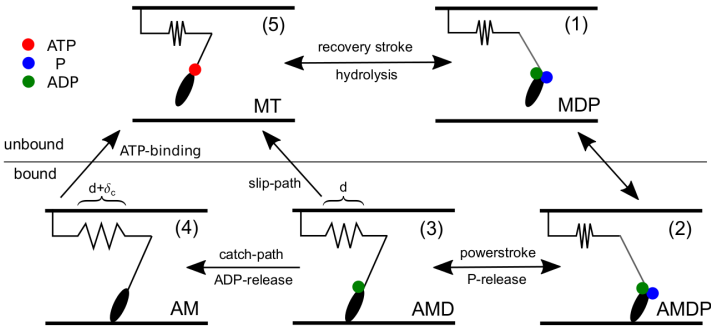

Figure 7.5: Schematics of the myosin II motor cycle with five steps. The two states above the line are unbound and the three below are bound. Binding and unbinding corresponds to establishing and removing a crossbridge between motor and actin filament, respectively. Myosin II makes two powerstrokes with the second one being a catch bond (slower under force), such that muscle can work also under high load. It also has a safety exit (the slip path) to unbind if force is too large. It finally unbinds from the rigor state by binding ATP. If no ATP is present, the system crosslinks and becomes rigid (this happens in dead bodies).

release of ADP and P_i, arriving at more states. For single motor heads like the myosin II heads in a minifilament or muscle, one rarely goes beyond five-state crossbridge-models. However, if one analyses a two-headed motor like kinesin, one can easily get more states. The same holds of course for assemblies of motor heads. In general, one ends up with high-dimensional and complex master equations that have to be treated with computer simulations. Most importantly, in crossbridge models one does not model the movement of the motor explicity, but it is associated implicitly with one of the transitions. This agrees with experimental observations and results from molecular dynamics simulations that show that movement of motor parts is always much faster than the dwelling times in the different states.

Here we want to follow another route and turn to a two-state model that uses the concept of continuous diffusion to explain how directed motion can emerge out of random switching. This class of models is called *isothermal ratchet models* and they are more general, but also less specific than crossbridge models. In contrast to the Feynman ratchet or a Carnot machine, the system does not operate at different temperatures, but isothermally. Here we present the mathematical analysis that identifies the two essential prerequisites to obtain directed motion.

We start with the Fokker-Planck equation from eq. 7.4 and rewrite it as continuity equation

$$\dot{p}(x,t) + J'(x,t) = 0 \tag{7.33}$$

with the flux

$$J = vp - Dp' \tag{7.34}$$

We next assume overdamped dynamics (no mass) and write the velocity as

$$v = \mu F = \mu \left[-W' - F_{ext}\right] \tag{7.35}$$

where the mobility μ is the inverse of the friction coefficient and the force F is divided into force from a potential $W(x)$ and an external force F_{ext} (the minus for F_{ext} means that the force is positive if it acts to the left, against the movement of the motor, like above for the one-state motor). We also make use of the Stokes-Einstein relation $D = k_B T\mu$, which is an example of the fluctuation-dissipation theorem (D is fluctuation, μ is dissipation, and the two are not independent of each other, but related by temperature). Thus we now have for the flux

$$J = -\mu \left[(W' + F_{ext})p + k_B T p' \right] \tag{7.36}$$

Together Eqs. 7.33 and 7.36 define the FPE as we use it here.

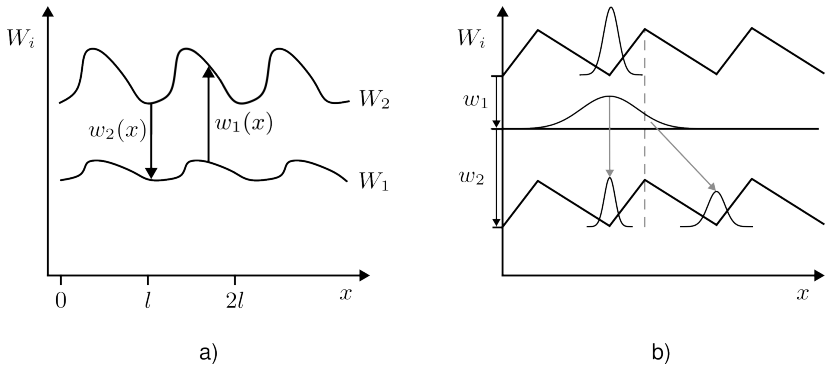

Figure 7.6: a) Typical potentials for the two-state isothermal ratchet model. Both the potentials W_i and the transition rates ω_i have to be periodic. Motion ensues if detailed balance for the rates is broken. c) The simplest example would be the switch between a flat potential and an asymmetric sawtooth potential.

We now write the Fokker-Planck equations for two states with switching between them:

$$\dot{p}_1 + J_1' = -\omega_1(x)p_1(x,t) + \omega_2(x)p_2(x,t) \tag{7.37}$$

$$\dot{p}_2 + J_2' = \omega_1(x)p_1(x,t) - \omega_2(x)p_2(x,t) \tag{7.38}$$

$$J_i = -\mu_i \left[(W_i' + F_{ext})p_i + k_B T p_i' \right] \tag{7.39}$$

Note that the switching terms with the rates ω_1 and ω_2 differ only by a minus sign between the two states. For simplicity, in the following we assume $\mu_1 = \mu_2 = \mu$. The two potentials W_i define the two states. An extreme case would be a sawtooth potential and a flat potential, for example because one state is charged and the other is not. At any rates, the potentials $W_i(x)$ and the switching rates $\omega_i(x)$ should have the same periodicity with unit cell size l, because this is imposed by the track with repeat distance l. We also note that the two potentials are of purely physical (passive) origin and therefore should not be tilted, which means that

$$\Delta W_i = W_i(x + l) - W_i(x) = 0 \tag{7.40}$$

Otherwise the motor would exhibit motion to the right simply because it moves down a gradient. What we want to model here is the opposite, namely the

fact that molecular motors spontaneous generate motion in a non-tilted energy landscape by locally burning energy, without a global gradient.

The beauty of this model is that we do not have to specify potentials and rates to get the general results we are after. We define total probability and total flux as

$$P(x,t) = \sum_i p_i(x,t), \;\; J(x,t) = \sum_i J_i(x,t) \tag{7.41}$$

If we sum up the first two equations from Eq. 7.39, the switching terms drop out and we get a FPE without source terms:

$$\dot{P}(x,t) + J'(x,t) = 0 \tag{7.42}$$

We next define local fractions of occupation

$$\lambda_i(x,t) = \frac{p_i(x,t)}{P(x,t)} \Rightarrow \sum_i \lambda_i = 1 \tag{7.43}$$

We now calculate the total flux. Using $p_i = \lambda_i P$ and the product rule we get

$$J = -\mu \sum_i \left[\lambda_i W_i' + k_B T \lambda_i' + \lambda_i F_{ext})P + k_B T \lambda_i P'\right] \tag{7.44}$$

$$= -\mu \left[(\sum_i \lambda_i W_i' + 0 + F_{ext})P + k_B T P'\right] \tag{7.45}$$

Thus we have exactly the general form for the flux, compare eq. 7.36, if we define an effective potential by

$$W_{eff}(x,t) = \int_0^x dx' \left(\sum_i \lambda_i(x',t) W_i'(x')\right) \tag{7.46}$$

If we further consider the steady state of the system, in which J =constant, the effective potential becomes only dependent on position

$$W_{eff}(x) = \int_0^x dx' \left(\sum_i \lambda_i(x') W_i'(x')\right) \tag{7.47}$$

Note that the switching rates ω_i enter indirectly through the occupancies λ_i.

We now consider the case without external force F_{ext} and ask under which conditions the system can generate directed motion by itself. Such motion appears if the effective potential is tilted over one period. We therefore define

$$\Delta W_{eff} = \int_0^l dx' \left(\sum_i \lambda_i(x') W_i'(x')\right) \tag{7.48}$$

and ask under which conditions this quantity becomes finite. We then immediately see that two conditions have to be satisfied:

- The potentials $W_i(x)$ and/or the transition rates $\omega_i(x)$ have to be asymmetric under $x \to -x$. Otherwise the integrand was symmetric and the integral vanished. A simple example for this would be an asymmetric sawtooth potential. Then the transition rates in principle could be symmetric, but one can show that this is not very efficient, so one expects both potentials and transition rates to be asymmetric.

- The switching rates have to break detailed balance, which means that the system has to be out of equilibrium. Otherwise the steady state distribution would be the Boltzmann distribution

$$\lambda_i(x) = \frac{e^{-W_i/k_BT}}{\sum_i e^{-W_i/k_BT}} \tag{7.49}$$

  We then would have

$$\sum_i \lambda_i(x) W_i'(x) = \partial_x \left[(-k_BT) \ln(\sum_i e^{-W_i(x)/k_BT}) \right] \tag{7.50}$$

  Thus the integrand in Eq. 7.48 would be a total derivative and the integral would vanish.

These two conclusions are non-trivial and must be valid for any specific motor model. One also can show that they are true for the case $\mu_1 \neq \mu_2$.

For many purposes, it is useful to define the deviation from equilibrium. This can be done by writing

$$\omega_1 = \omega_2 e^{\beta(W_1 - W_2)} + \Omega(x) \tag{7.51}$$

thus detailed balance corresponds to $\Omega(x) = 0$. If one further defines $\Omega(x) = \Omega\theta(x)$, then the scalar amplitude Ω is a measure for deviation from equilibrium. The excitation distribution $\theta(x)$ usually is localized around the minimum of the potential W_1 (active site). Note that switching from the minimum is exactly the opposite of what would happen in equilibrium, where switching would occur at the maximum due to detailed balance.

7.7 Ratchet model for motor ensembles

As we have seen, the isothermal two-state ratchet model is ideal to identify the conditions for movement of a single motor. We now carry this approach further to address collective effects in ensembles of molecular motors (alternatively, we could look at collective effects in master equations for groups of motors). In the cell, motors rarely work alone, but usually are coupled together in a group, e.g. when transporting cargo along filaments or generating force in the cytoskeleton, in flagella and cilia, or in the muscle. We consider the case that the motors are coupled to a rigid backbone, thus at each time t, they have the same velocity v. As we will see, this coupling is sufficient to result in collective effects which resemble

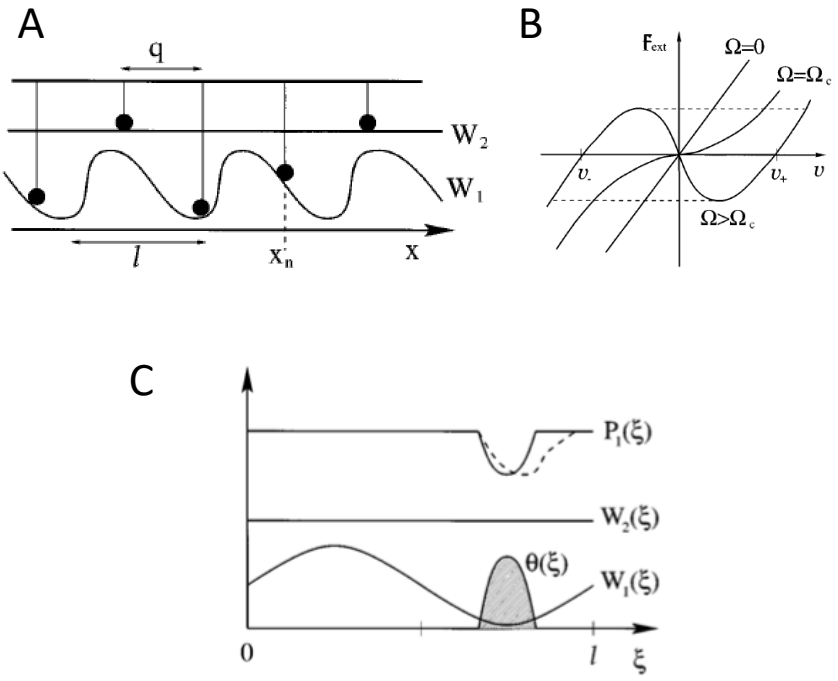

Figure 7.7: (A) We consider an ensemble of motors that is coupled through a rigid backbone. Each motor can bind to the filament and slide down the potential corresponding to the current state. (B) For sufficient deviation $\Omega > \Omega_c$ from equilibrium, the force-velocity relation becomes negative and spontaneous symmetry breaking with finite velocities v_+ and v_- occurs at cero forcing. As the external force is varied, a hysteresis loop emerges. (C) Spontaneous motion occurs because excitation causes a dip in $p_1(x)$ that then moves to the right with velocity v. This effectively increases the numbers of motors pulling further to the right. Like during a phase transition, this is an instability.

phase transitions. Each of the motors can bind to the filament at position x and then generates a force $F = -\partial_x W_i(x)$, depending on which state i it is in.

We consider a mean field theory, that is many motors that are homogeneously distributed along the backbone, in a manner that is incommensurable with the potentials with periodicity l, compare Fig. 7.7(A). We consider the variable x to be cyclic, thus we only have to deal with a unit cell with $0 \leq x \leq l$. We again consider the Fokker-Planck equation for two states, but now for a common velocity v:

$$\dot{p}_1 + v\partial_x p_1 = -\omega_1(x)p_1 + \omega_2(x)p_2 \tag{7.52}$$

$$\dot{p}_2 + v\partial_x p_2 = \omega_1(x)p_1 - \omega_2(x)p_2 \tag{7.53}$$

Note that, because we consider a large cargo, we neglect the effect of diffusion. The force balance reads

$$v = \mu(F_{ext} + F_{int}) \tag{7.54}$$

where μ is mobility and F_{ext} is the given external force (provided e.g. by an optical tweezer). The internal force is

$$F_{int} = -\int_0^l dx(p_1\partial_x W_1 + p_2\partial_x W_2) \tag{7.55}$$

Normalization reads

$$p_1(x,t) + p_2(x,t) = \frac{1}{l} \Rightarrow p_2 = \frac{1}{l} - p_1 \tag{7.56}$$

and $\int_0^l dx(p_1 + p_2) = 1$.

We now consider steady state, $\dot{p}_i = 0$. Together with the normalization, the first of the two Fokker-Planck equations now gives

$$v\partial_x p_1 = -(\omega_1 + \omega_2)p_1 + \frac{\omega_2}{l} \ . \tag{7.57}$$

The force balance (or momentum conservation) gives

$$F_{ext} = \frac{v}{\mu} - F_{int} = \frac{v}{\mu} + \int_0^l dx \ p_1\partial_x(W_1 - W_2) \tag{7.58}$$

where the constant term drops out because we integrate over $\partial_x W_2$ and W_2 is periodic.

For specific choices of the potentials W_i and the rates ω_i, these equations for the steady state $p_1(x)$ can now be solved. This will then lead to a force-velocity relation $F_{ext}(v)$. Here we want to proceed with generic properties of this theory and therefore make a Taylor expansion in small velocity v:

$$p_1(x) = \sum_{n=0}^{\infty} p_1^{(n)}(x)v^n \ . \tag{7.59}$$

The Fokker-Planck equation leads to a recursion relation for the coefficients:

$$p_1^{(0)}(x) = \frac{\omega_2}{(\omega_1 + \omega_2)l}, \ p_1^{(n)}(x) = \frac{-1}{(\omega_1 + \omega_2)}\partial_x p_1^{(n-1)}(x) \tag{7.60}$$

For the force-velocity relation we get

$$F_{ext} = F^{(0)} + (\frac{1}{\mu} + F^{(1)})v + \sum_{n=2}^{\infty} F^{(n)} v^n \tag{7.61}$$

with

$$F^{(n)} = \int dx \; p_1^{(n)} \partial_x (W_1 - W_2) \; . \tag{7.62}$$

For simplicity we next specify for symmetric potentials ($W_i(x) = W_i(-x)$), so all even coefficients vanish ($F^{(0)} = F^{(2)} = \cdots = 0$) and the force-velocity relation $F_{ext}(v)$ becomes anti-symmetric:

$$F_{ext} = (\frac{1}{\mu} + F^{(1)})v + F^{(3)} v^3 + O(v^5) \tag{7.63}$$

For detailed balance ($\Omega = 0$ in Eq. 7.51), we can calculate

$$F^{(1)} = \int dx \frac{\beta}{l} \frac{e^{\beta(W_1 - W_2)}}{(1 + e^{\beta(W_1 - W_2)})^2} \frac{(\partial_x (W_1 - W_2))^2}{(\omega_1 + \omega_2)} \tag{7.64}$$

thus this quantity is positive and the only solution to the force-velocity relation at zero forcing ($F_{ext} = 0$) is $v = 0$. Thus with detailed balance, no spontaneous motion can occur. However, at $\Omega_c > 0$ the coefficient $F^{(1)}$ can be negative with $F^{(1)} = -1/\mu$. Then finite values for v become possible for $\Omega > \Omega_c$, compare Fig. 7.7(B), and the velocity rises as $\pm(\Omega - \Omega_c)^{1/2}$. Thus for sufficiently large deviation from equilibrium, the system spontaneously starts to move. The scaling exponent 1/2 is typical for the mean field theory and the system has to spontaneously break symmetry to move either right or left with velocities v_+ and v_-, respectively. Note that in contrast to the single motor case, spontaneous motion ensues even for symmetric potentials; for single motors, the asymmetric potential is required to give it its direction, but for multiple motors, the system is persistent and a spontaneous symmetry break occurs. If one now switches on the external force, one can move the velocity away from its value at the transition point, compare Fig. 7.7(B). For example, if the ensembles moves to the right with velocity v_+, one can pull it to smaller velocities with a negative external force F_{ext}. However, at a critical value of F_{ext}, this branch loses stability and jumps to a negative velocity. The same works in the other direction and there is a hysteresis loop. In general, the mathematical structure of this theory is exactly the same as for the second order phase transition of the Ising model for ferromagnetism. Velocity v corresponds to the magnetization M, external force F_{ext} to the magnetic field H, and the deviation from equilibrium Ω to the inverse temperature β. If the system works against an external spring, oscillations occur, as observed often in experiments with molecular motors. A famous example are spontaneous oscillations of hair bundles in the inner ear, which lead to otoacoustic emissions.

Fig. 7.7(C) shows the main mechanism generating the instability leading to spontaneous motion. As the motors are excited at the minimum of $W_1(x)$, one gets a dip in $p_1(x)$. This dip moves to the right, effectively repopulating the motor population pulling to the right. Thus any fluctuation will be increased and the system is unstable. The same mechanism is at work in phase transition, when the system does not counteract a fluctuation.

7.8 Master equation approach for motor ensembles

The main advantage of the ratchet models is that they allow us to analyze the fundamental requirements for motion. In order to describe the function of motor ensembles in close comparision to experiments, however, one usually turns to master equations. Here we discuss a simple version that describes cooperative cargo transport by an ensemble of motors[2]. Rather than focusing on the spatial position of the motor ensemble, we rather will later enforce movement in one direction, but focus on the physical limits of this movement, that is on the possibility that the walk stops because the ensemble loses contact with its track. Therefore we now will consider the relevant internal state of the ensemble, namely the number of bound motors. Similar approaches have been used before to describe the internal dynamics of adhesion clusters[3].

We consider N motors, of which $0 \leq n \leq N$ are bound at any time t. The variable $n(t)$ is described by a one-step master equation:

$$\dot{p}_n = \epsilon_{n+1} p_{n+1} + \pi_{n-1} p_{n-1} - (\epsilon_n + \pi_n) p_n \tag{7.65}$$

where ϵ_n and π_n are dissociation and association rates, respectively. The stationary state leads to the detailed balance condition

$$\epsilon_{n+1} p_{n+1} = \pi_n p_n \tag{7.66}$$

and this allows us to calculate the steady state probabilities in a recursive manner:

$$p_n = p_0 \prod_{i=0}^{n-1} \frac{\pi_i}{\epsilon_{i+1}} \tag{7.67}$$

where normalization $\sum_{n=0}^{N} p_n = 1$ gives us the starting condition

$$p_0 = \left(1 + \sum_{n=1}^{N} \prod_{i=0}^{n-1} \frac{\pi_i}{\epsilon_{i+1}} \right)^{-1} = \left(1 + \sum_{n=0}^{N-1} \prod_{i=0}^{n} \frac{\pi_i}{\epsilon_{i+1}} \right)^{-1} . \tag{7.68}$$

From here we define a few quantities of interest. The average number of bound motors is

$$N_b = \sum_{n=1}^{N} n \frac{p_n}{1 - p_0} \tag{7.69}$$

where we have excluded the state $n = 0$ from the sum and have normalized in respect to the bound states only. The average velocity is

$$v_{eff} = \sum_{n=1}^{N} v_n \frac{p_n}{1 - p_0} \tag{7.70}$$

[2]Our treatment is taken from Stefan Klumpp and Reinhard Lipowksy, Coooperative cargo transport by several molecular motors, PNAS 201: 17284-17289, 2005. Compare also the related paper by Melanie Müller, Stefan Klumpp and Reinhard Lipowsky, Tug-of-war as a cooperative mechanism for bidirectional cargo transport by molecular motors, PNAS 105: 4609-4614, 2008, which generalizes this ansatz to two competing motor ensembles pulling in opposite directions.

[3]Compare Thorsten Erdmann and Ulrich S. Schwarz, Stability of adhesion clusters under constant force, Phys. Rev. Lett., 92:108102, 2004.

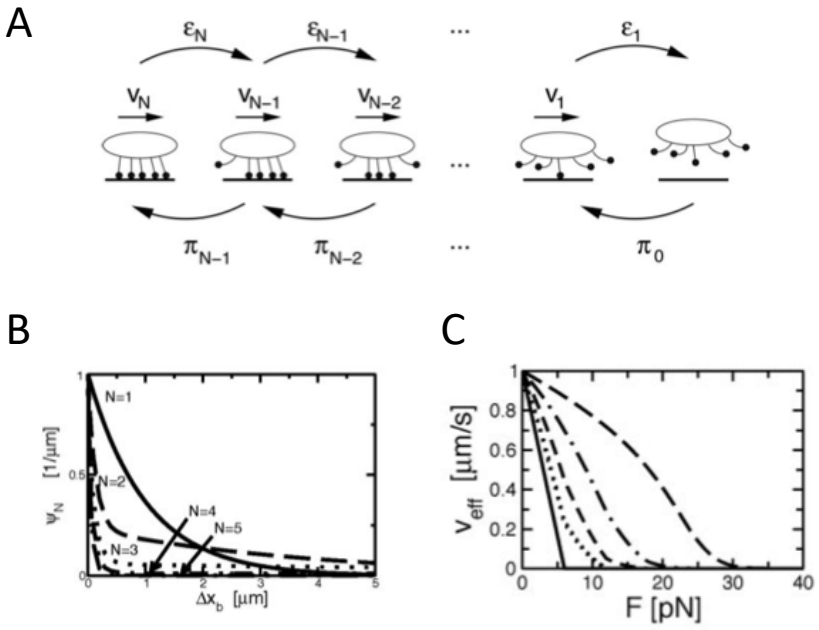

Figure 7.8: (A) Definition of the one-step master equation for cooperative transport by motor ensembles. (B) Distribution of walking distances for group size $N = 1, 2, 3, 4, 5$ kinesin motors without load. For large N, these distributions become very flat and their averages grow. (C) Force-velocity relation for $N = 1, 2, 3, 5, 10$ kinesin motors. The effective stall force increases and the curve changes from linear to concave-down. From Klumpp and Lipowsky PNAS 2005.

and the effective unbinding rate ϵ_{eff} is defined by

$$\epsilon_{eff}(1 - p_0) = \pi_0 p_0 \ . \tag{7.71}$$

The inverse of this would be the average time $< \Delta t_b >$ it takes for the ensemble to unbind. We can calculate

$$\epsilon_{eff} = \pi_0 \frac{p_0}{1 - p_0} = \frac{\pi_0}{\left(\sum_{n=0}^{N-1} \prod_{i=0}^{n} \frac{\pi_i}{\epsilon_{i+1}}\right)} = \frac{\epsilon_1}{\left(1 + \sum_{n=1}^{N-1} \prod_{i=1}^{n} \frac{\pi_i}{\epsilon_{i+1}}\right)} \tag{7.72}$$

Finally we define the average walking distance $< \Delta x_b >$. This can be simply achieved by replacing ϵ_n by ϵ_n / v_n and π_n by π_n / v_n in the formula for $< \Delta t_b >$ (thus replacing inverse time steps by inverse step sizes):

$$< \Delta x_b >= \frac{v_1}{\epsilon_1} \left(1 + \sum_{n=1}^{N-1} \prod_{i=1}^{n} \frac{\pi_i v_{i+1}}{\epsilon_{i+1} v_i}\right) \tag{7.73}$$

7.8.1 Without load

Our model definition is now concluded and to continue, we have to specify rates and velocity for the different states n. We first consider the case of vanishing external load. We set

$$\epsilon_n = n\epsilon, \pi_n = (N-n)\pi, v_n = v \tag{7.74}$$

assuming that each bond dissociates and associates with constant rates ϵ and π, respectively, independent of the others, thus leading to the combinatorial factors, and that velocity v is independent of state. We define $\gamma = \pi/\epsilon$, the dimensionless (re)binding rate. The probability distribution now is simply a binomial distribution, because each bond is open and closed with the probabilities $1/(1+\gamma)$ and $\gamma/(1+\gamma)$, respectively:

$$p_n = \binom{N}{n}\left(\frac{1}{1+\gamma}\right)^n\left(\frac{\gamma}{1+\gamma}\right)^{N-n} = \binom{N}{n}\frac{\gamma^n}{(1+\gamma)^N} \tag{7.75}$$

With some work, one can check that this agrees with the general formulae given above. In particular, we have $p_0 = 1/(1+\gamma)^N$.

The average number of bound motors follows from the average of the binomial distribution (with the normalization to the bound states):

$$N_b = \frac{1}{1-p_0} < n >= \frac{1}{1-p_0}\frac{\gamma}{1+\gamma}N = \frac{\gamma(1+\gamma)^{N-1}}{(1+\gamma)^N - 1}N \approx \frac{\gamma}{1+\gamma}N \tag{7.76}$$

with the last expression being valid in the limit of very large N. In the limit of large γ we get $N_b \approx N$. The effective unbinding rate follows as

$$\epsilon_{eff} = \pi_0\frac{p_0}{1-p_0} = \frac{N\gamma\epsilon}{(1+\gamma)^N - 1} \tag{7.77}$$

and therefore the average bound time is

$$< \Delta t_b >= \frac{1}{\epsilon_{eff}} = \frac{(1+\gamma)^N - 1}{N\gamma\epsilon} \tag{7.78}$$

From here we get the average run length

$$< \Delta x_b >= v < \Delta t_b >= \frac{v}{N\gamma\epsilon}[(1+\gamma)^N - 1] \tag{7.79}$$

Thus we see that it increases exponentially with N, thus larger clusters can walk for much longer distances as long as $\gamma > 1$. In the limit of very weak binding, we make a Taylor expansion in γ and find

$$< \Delta x_b >\approx \frac{v}{\epsilon}[1 + \frac{(N-1)}{2}\gamma] \tag{7.80}$$

The first term corresponds to the single motor. In this case, the additional increase due to cooperativity is only linear in N.

In the case of kinesin, we have $v = 1$ μm/s, $\epsilon = 1$ Hz and $\pi = 5$ Hz, thus $\gamma = 5$ and run length increases exponentially with motor number. For $N = 1$, we have $< \Delta x_b >= v/\epsilon = 1$ μm. For $N = 5$, we are already up from 1 to 311 μm, and 10 motors give one meter. Note that the longest neural axons can extend up to one meter, so this cooperative effect is very relevant. However, note also that this is only a statement on the average. One can also calculate the full distribution and find that it becomes very broad for large collectives.

7.8.2 With load

In order to deal with the case of mechanical load F, we use the linearized force-velocity relation:

$$v_n(F) = v(1 - \frac{F}{nF_s}) \tag{7.81}$$

Very importantly, here we account for the fact that force F is distributed over the bound motors (*load sharing*), thus dissipating its effect over the cluster. While the association is usually assumed to be force-independent, for the dissociation we have to take force into account:

$$\pi_n = (N - n)\pi, \epsilon_n(F) = n\epsilon e^{F/(nF_d)} \tag{7.82}$$

The second equation (*Bell-relation*) takes into account that dissociation is exponentially increased by force, as explained by Kramers theory. Here again we also take load sharing into account. For kinesin, the stall force F_s and the detachment force F_d are 6 and 3 pN, respectively. If one now evaluates the formulae given above for these rates, one finds that increasing N leads to a much slower decay in the force-velocity relation, and changes its character from linear to concave-down.

Bibliography

[1] John Jumper, Richard Evans, Alexander Pritzel, Tim Green, Michael Figurnov, Olaf Ronneberger, Kathryn Tunyasuvunakool, Russ Bates, Augustin Zidek, Anna Potapenko, Alex Bridgland, Clemens Meyer, Simon A. A. Kohl, Andrew J. Ballard, Andrew Cowie, Bernardino Romera-Paredes, Stanislav Nikolov, Rishub Jain, Jonas Adler, Trevor Back, Stig Petersen, David Reiman, Ellen Clancy, Michal Zielinski, Martin Steinegger, Michalina Pacholska, Tamas Berghammer, Sebastian Bodenstein, David Silver, Oriol Vinyals, Andrew W. Senior, Koray Kavukcuoglu, Pushmeet Kohli, and Demis Hassabis. Highly accurate protein structure prediction with AlphaFold. *Nature*, 596(7873):583–589, August 2021. Number: 7873 Publisher: Nature Publishing Group.

[2] Minkyung Baek, Frank DiMaio, Ivan Anishchenko, Justas Dauparas, Sergey Ovchinnikov, Gyu Rie Lee, Jue Wang, Qian Cong, Lisa N. Kinch, R. Dustin Schaeffer, Claudia MillÃ¡n, Hahnbeom Park, Carson Adams, Caleb R. Glassman, Andy DeGiovanni, Jose H. Pereira, Andria V. Rodrigues, Alberdina A. van Dijk, Ana C. Ebrecht, Diederik J. Opperman, Theo Sagmeister, Christoph Buhlheller, Tea Pavkov-Keller, Manoj K. Rathinaswamy, Udit Dalwadi, Calvin K. Yip, John E. Burke, K. Christopher Garcia, Nick V. Grishin, Paul D. Adams, Randy J. Read, and David Baker. Accurate prediction of protein structures and interactions using a three-track neural network. *Science*, 373(6557):871–876, August 2021. Publisher: American Association for the Advancement of Science.

[3] Daniel Lingwood and Kai Simons. Lipid Rafts As a Membrane-Organizing Principle. *Science*, 327(5961):46–50, January 2010. Publisher: American Association for the Advancement of Science.

[4] Sarah L. Veatch, Nat Rogers, Adam Decker, and Sarah A. Shelby. The plasma membrane as an adaptable fluid mosaic. *Biochimica et Biophysica Acta (BBA) - Biomembranes*, 1865(3):184114, March 2023.

[5] Clifford P. Brangwynne, Christian R. Eckmann, David S. Courson, Agata Rybarska, Carsten Hoege, Jöbin Gharakhani, Frank Jülicher, and Anthony A. Hyman. Germline P Granules Are Liquid Droplets That Localize by Controlled Dissolution/Condensation. *Science*, 324(5935):1729–1732, June 2009. Publisher: American Association for the Advancement of Science.

[6] Anthony A. Hyman, Christoph A. Weber, and Frank JÃ¼licher. Liquid-Liquid Phase Separation in Biology. *Annual Review of Cell and Developmental Biology*, 30(1):39–58, 2014.

[7] Huan-Xiang Zhou, Valery Nguemaha, Konstantinos Mazarakos, and Sanbo Qin. Why Do Disordered and Structured Proteins Behave Differently in Phase Separation? *Trends in Biochemical Sciences*, 43(7):499–516, July 2018.

[8] Daan Frenkel and Berend Smit. *Understanding Molecular Simulation: From Algorithms to Applications*. Elsevier, October 2001. Google-Books-ID: 5qT-zldS9ROIC.

[9] Nicola Bellotto, Jaime Agudo-Canalejo, Remy Colin, Ramin Golestanian, Gabriele Malengo, and Victor Sourjik. Dependence of diffusion in escherichia coli cytoplasm on protein size, environmental conditions, and cell growth. 11:e82654. Publisher: eLife Sciences Publications, Ltd.

[10] Ulf D. Schiller, Timm Krüger, and Oliver Henrich. Mesoscopic modelling and simulation of soft matter. *Soft Matter*, 14(1):9–26, December 2017. Publisher: The Royal Society of Chemistry.

[11] R.R. Netz. Electrostatistics of counter-ions at and between planar charged walls: From Poisson-Boltzmann to the strong-coupling theory. *The European Physical Journal E*, 5(1):557–574, August 2001.

[12] W. C. K. Poon and David Andelman. *Soft Condensed Matter Physics in Molecular and Cell Biology*. CRC Press, January 2006. Google-Books-ID: hk9UbvyKZE0C.

[13] A. G. Moreira and R. R. Netz. Strong-coupling theory for counter-ion distributions. *Europhysics Letters*, 52(6):705, December 2000. Publisher: IOP Publishing.

[14] Douglas E. Smith, Sander J. Tans, Steven B. Smith, Shelley Grimes, Dwight L. Anderson, and Carlos Bustamante. The bacteriophage phi29 portal motor can package DNA against a large internal force. *Nature*, 413(6857):748–752, October 2001.

[15] Pablo Ceres and Adam Zlotnick. Weak Protein Protein Interactions Are Sufficient To Drive Assembly of Hepatitis B Virus Capsids. *Biochemistry*, 41(39):11525–11531, October 2002.

[16] Willem K. Kegel and Paul van der Schoot. Competing Hydrophobic and Screened-Coulomb Interactions in Hepatitis B Virus Capsid Assembly. *Biophysical Journal*, 86(6):3905–3913, June 2004.

[17] P. B. Canham. The minimum energy of bending as a possible explanation of the biconcave shape of the human red blood cell. *Journal of Theoretical Biology*, 26(1):61–81, January 1970.

[18] W. Helfrich. Elastic Properties of Lipid Bilayers: Theory and Possible Experiments. *Zeitschrift für Naturforschung C*, 28(11-12):693–703, December 1973. Publisher: De Gruyter.

[19] R. Lipowsky and E. Sackmann. *Structure and Dynamics of Membranes: I. From Cells to Vesicles / II. Generic and Specific Interactions*. Elsevier, June 1995. Google-Books-ID: V1H9oVpNC7wC.

[20] Patricia Bassereau and Pierre Sens, editors. *Physics of Biological Membranes*. Springer International Publishing, Cham, 2018.

[21] Ou-Yang Zhong-can and Wolfgang Helfrich. Bending energy of vesicle membranes: General expressions for the first, second, and third variation of the shape energy and applications to spheres and cylinders. *Physical Review A*, 39(10):5280–5288, May 1989. Publisher: American Physical Society.

[22] Udo Seifert, Karin Berndl, and Reinhard Lipowsky. Shape transformations of vesicles: Phase diagram for spontaneous- curvature and bilayer-coupling models. *Physical Review A*, 44(2):1182–1202, July 1991.

[23] Ling Miao, Udo Seifert, Michael Wortis, and Hans-GÃ¼nther DÃ¶bereiner. Budding transitions of fluid-bilayer vesicles: The effect of area-difference elasticity. *Physical Review E*, 49(6):5389, June 1994.

[24] Patricia Bassereau, Benoit Sorre, and Aurore LÃ©vy. Bending lipid membranes: Experiments after W. Helfrich's model. *Advances in Colloid and Interface Science*, 208:47–57, June 2014.

[25] R. Lipowsky and H.-G. DÃ¶bereiner. Vesicles in contact with nanoparticles and colloids. *Europhysics Letters*, 43(2):219, July 1998. Publisher: IOP Publishing.

[26] Markus Deserno. Elastic deformation of a fluid membrane upon colloid binding. *Physical Review E*, 69(3):031903, March 2004. Publisher: American Physical Society.

[27] Lionel Foret. Shape and energy of a membrane bud induced by protein coats or viral protein assembly. *The European Physical Journal E*, 37(5):42, May 2014.

[28] Felix Frey, Falko Ziebert, and Ulrich S. Schwarz. Dynamics of particle uptake at cell membranes. *Physical Review E*, 100(5):052403, November 2019. Publisher: American Physical Society.

[29] P. G. De Gennes and C. Taupin. Microemulsions and the flexibility of oil/water interfaces. *The Journal of Physical Chemistry*, 86(13):2294–2304, June 1982. Publisher: American Chemical Society.

[30] W. Helfrich. Steric Interaction of Fluid Membranes in Multilayer Systems. *Zeitschrift für Naturforschung A*, 33(3):305–315, March 1978. Publisher: De Gruyter.

[31] W. Janke and H. Kleinert. Fluctuation pressure of membrane between walls. *Physics Letters A*, 117(7):353–357, September 1986.

[32] Dmitry A. Fedosov, Hiroshi Noguchi, and Gerhard Gompper. Multiscale modeling of blood flow: from single cells to blood rheology. *Biomechanics and Modeling in Mechanobiology*, 13(2):239–258, April 2014.

[33] N. S. Gov and S. A. Safran. Red Blood Cell Membrane Fluctuations and Shape Controlled by ATP-Induced Cytoskeletal Defects. *Biophysical Journal*, 88(3):1859–1874, March 2005.

[34] Young-Zoon Yoon, Ha Hong, Aidan Brown, Dong Chung Kim, Dae Joon Kang, Virgilio L. Lew, and Pietro Cicuta. Flickering Analysis of Erythrocyte Mechanical Properties: Dependence on Oxygenation Level, Cell Shape, and Hydration Level. *Biophysical Journal*, 97(6):1606–1615, September 2009.

[35] H. Turlier, D. A. Fedosov, B. Audoly, T. Auth, N. S. Gov, C. Sykes, J.-F. Joanny, G. Gompper, and T. Betz. Equilibrium physics breakdown reveals the active nature of red blood cell flickering. *Nature Physics*, 12(5):513–519, May 2016.

[36] Herve Turlier and Timo Betz. Unveiling the Active Nature of Living-Membrane Fluctuations and Mechanics. *Annual Review of Condensed Matter Physics*, 10(1):213–232, 2019.